Real-time Monitoring of (Photo)chemical Reactions in Micro Flow Reactors and Levitated Droplets by IR-MALDI Ion Mobility and Mass Spectrometry

---

cumulative Dissertation

A thesis submitted for the degree of
"Doctor rerum naturalium" (Dr. rer. nat.)
in Physical Chemistry
to the Institute of Chemistry, Faculty of Science, University of Potsdam

by

Aleksandra Michalik-Onichimowska

Potsdam, 31 May 2022

Reviewers:
Prof. Hans-Gerd Löhmannsröben
Dr. Jens Riedel
Prof. Michael W. Linscheid

Published online on the
Publication Server of the University of Potsdam:
https://doi.org/10.25932/publishup-55729
https://nbn-resolving.org/urn:nbn:de:kobv:517-opus4-557298

List of Publications

1. A. Michalik-Onichimowska, T. Beitz, U. Panne, H.-G. Löhmannsröben, J. Riedel, “Laser ionization ion mobility spectrometric interrogation of acoustically levitated droplets” Anal. Bioanal. Chem., 2019, 411, 8053–8061; DOI:10.1016/j.snb.2016.06.155

2. A. Michalik-Onichimowska, S. Kern, J. Riedel, U. Panne, R. King, M. Maiwald “"Click" analytics for "click" chemistry - a simple method for calibration-free evaluation of online NMR spectra” J. Magn. Reson. 2017, 277, 154 –161

3. A. Michalik-Onichimowska, T. Beitz, U. Panne, H.-G. Löhmannsröben, J. Riedel, “Microsecond mid-infrared laser pulses for atmospheric pressure laser ablation/ionization of liquid samples”, Sens. Actuators, B, 2017, 238, 298-305; DOI:10.1007/s00216-019-02167-5

Presentations

1. A. Michalik-Onichimowska, C. Warschat, U. Panne, H.-G. Löhmannsröben, J. Riedel “Online monitoring of photoreactions within levitated droplets by LA-DBD-MS”, 49. Jahrestagung der Deutsche Gesellschaft für Massenspektrometrie (March 2016), presentation

2. A. Michalik, A. Siwek, G. Meißner, “MALDI-MS Imaging – Technical Aspects”, Kosmos Summer University “Limits & Scales in Analytical Sciences” September 2014, challenge session & discussion panel

Posters

3. A. Michalik-Onichimowska, J. Riedel, U. Panne, H.-G. Löhmannsröben, “Real time monitoring of photoreactions performed within levitated droplets by LA-DBD-MS”, 21st International Mass Spectrometry Conference (September 2016), poster

4. A. Michalik-Onichimowska, T. Beitz, J. Riedel, U. Panne, H.-G. Löhmannsröben, “Monitoring of Thiol-Ene Coupling by Mass Spectrometry and Ion Mobility Spectrometry” European Symposium on Chemical Reaction Engineering (October 2015), poster

5. A. Michalik-Onichimowska, T. Beitz, J. Riedel, U. Panne, H.-G. Löhmannsröben, “The effect of laser pulse duration on atmospheric pressure IR-MALDI using liquid matrices” Bunsentagung (Mai 2015), poster

6. A. Michalik-Onichimowska, T. Beitz, J. Riedel, U. Panne, H.-G. Löhmannsröben “Coupling of Acoustically Levitated Droplets to Ion Mobility Spectrometry”, 48. Jahrestagung der Deutsche Gesellschaft für Massenspektrometrie (March 2015), poster, Poster Award

7. A. Michalik, T. Beitz, J. Riedel, U. Panne, H.-G. Löhmannsröben’ “The effect of the laser pulse duration in infrared free-liquid MALDI” 20th International Mass Spectrometry Conference (September 2014), poster

Kurzzusammenfassung

Eine nachhaltigere chemische Industrie erfordert eine Minimierung der Lösungsmittel und Chemikalien. Daher werden Optimierung und Entwicklung chemischer Prozesse vor einer Produktion in großem Maßstab in kleinen Chargen durchgeführt. Der entscheidende Schritt bei diesem Ansatz ist die Skalierbarkeit von kleinen Reaktionssystemen auf große, kosteneffiziente Reaktoren. Die Vergrößerung des Volumens des Reaktionsmediums geht immer mit der Vergrößerung der Oberfläche einher, die mit dem begrenzenden Gefäß in Kontakt steht. Da das Volumen kubisch, während die Oberfläche quadratisch mit zunehmendem Radius skaliert, nimmt ihr Verhältnis nicht linear zu. Viele an der Grenzfläche zwischen Oberfläche und Flüssigkeit auftretende Phänomene können die Reaktionsgeschwindigkeiten und Ausbeuten beeinflussen, was zu falschen Prognosen aufgrund der kleinskaligen Optimierung führt. Die Anwendung von schwebenden Tropfen als behälterlose Reaktionsgefäße bietet eine vielversprechende Möglichkeit, die oben genannten Probleme zu vermeiden.

In der vorgestellten Arbeit wurde eine effiziente Kopplung von akustisch schwebenden Tropfen und IM Spektrometer für die Echtzeitüberwachung chemischer Reaktionen entwickelt, bei denen akustisch schwebende Tropfen als Reaktionsgefäße fungieren. Das Design des Systems umfasst die berührungslose Probenahme und Ionisierung, die durch Laserdesorption und -ionisation bei 2,94 µm realisiert wird. Der Umfang der Arbeit umfasst grundlegende Studien zum Verständnis der Laserbestrahlung von Tropfen im akustischen Feld. Das Verständnis dieses Phänomens ist entscheidend, um den Effekt der zeitlichen und räumlichen Auflösung der erzeugten Ionenwolke zu verstehen, die die Auflösung des Systems beeinflusst.

Der Aufbau umfasst eine akustische Falle, Laserbestrahlung und elektrostatische Linsen, die bei hoher Spannung unter Umgebungsdruck arbeiten. Ein effektiver Ionentransfer im Grenzflächenbereich zwischen dem schwebenden Tropfen und dem IMS muss daher elektrostatische und akustische Felder vollständig berücksichtigen. Für die Probenahme und Ionisation wurden zwei unterschiedliche Laserpulslängen untersucht, nämlich im ns- und µs-Bereich. Die Bestrahlung über µs-Laserpulse bietet gegenüber ns-Pulse mehrere Vorteile: i) das Tropfenvolumen wird nicht stark beeinflusst, was es ermöglichet, nur ein kleines Volumen des Tropfens abzutasten; ii) die geringere Fluenz führt zu weniger ausgeprägten Schwingungen des im akustischen Feld eingeschlossenen Tropfens und der Tropfen wird nicht aus dem akustischen Feld rückgeschlagen, was zum Verlust der Probe führen würde; iii) die milde Laserbestrahlung führt zu einer besseren räumlichen und zeitlichen Begrenzung der Ionenwolken, was zu einer besseren Auflösung der detektierten Ionenpakete führt. Schließlich ermöglicht dieses Wissen die Anwendung der Ionenoptik, die erforderlich ist, um den Ionenfluss zwischen dem im akustischen Feld suspendierten Tropfen und dem IM Spektrometer zu induzieren. Die Ionenoptik aus 2 elektrostatischen Linsen in der Nähe des Tropfens ermöglicht es, die Ionenwolke effektiv zu fokussieren und direkt zum IM Spektrometer-Eingang zu führen. Diese neuartige Kopplung hat sich beim Nachweis einiger basischer Moleküle als erfolgreich erwiesen. Um die Anwendbarkeit des Systems zu belegen, wurde die Reaktion zwischen N-Boc Cysteine Methylester und Allylalkohol in einem Chargenreaktor durchgeführt und online überwacht. Für eine Kalibrierung wurde der Reaktionsfortschritt parallel mittels ^{1}H-NMR verfolgt. Der beobachtete Reaktionsumsatz von mehr als 50% innerhalb der ersten 20 Minuten demonstrierte die Eignung der Reaktion, um die Einsatzpotentiale des entwickelten Systems zu bewerten.

Abstract

One aspect of achieving a more sustainable chemical industry is the minimization of the usage of solvents and chemicals. Thus, optimization and development of chemical processes for large-scale production is favourably performed in small batches. The critical step in this approach is upscaling the batches from the small reaction systems to the large reactors mandatory for cost efficient production in an industrial environment. Scaling up the bulk volume always goes along with increasing the surface where the reaction medium is in contact with the confining vessel. Since volume scales proportional with the cubic dimension while the surface scales quadratic, their ratio is size-dependent. The influence of reaction vessel walls can change the reaction performance. A number of phenomena occurring at the surface-liquid interface can affect reaction rates and yields, resulting in possible difficulties in predicting and extrapolating from small size production scale to large industrial processes. The application of levitated droplets as a containerless reaction vessels provides a promising possibility to avoid the above-mentioned issues.

In the presented work, an efficient coupling of acoustically levitated droplets to an ion mobility (IM) spectrometer, operating at ambient conditions, was designed for real-time monitoring of chemical reactions. The design of the system comprises noncontact sampling and ionization of the droplet realised by laser desorption/ionization at 2,94 μm. The scope of the work includes fundamental studies covering understanding of laser irradiation of droplets enclosed in an acoustical field. Understanding of this phenomenon is crucial to comprehending the effects of temporal and spatial resolution of the generated ion plume that influence the resolution of the system.

The set-up includes an acoustic trap, laser irradiation and ion manipulation electrostatic lenses operating at high voltage at ambient pressure. The complexity of the design needs to fully be considered for an effective ion transfer at the interface region between the levitated droplet and IM spectrometer. For sampling and ionization, two distinct laser pulse lengths were evaluated, ns and μs. Irradiation *via* μs laser pulses provides several advantages: i) the droplet volume is not extensively impinged, as in case of ns laser pulses, allowing the sampling of only the small volume of the droplet; ii) the lower fluence results in less pronounced oscillations of the droplet confined in the acoustic field. The droplet will not be dissipated out of the acoustic field leading to loss of the sample; iii) the mild laser irradiation results in better spatial and temporal ion plume confinement, leading to better resolution of the detected ion packets. Finally, this knowledge allows the application of ion optics necessary to induce ion flow between the droplet suspended in the acoustic field and the IM spectrometer. The ion optics, composed of 2 electrostatic lenses placed in the near vicinity of the droplet, allow effective focusing of the ion plume and its redirection directly to the IM spectrometer entrance. This novel coupling has proved to be successful for detection of some simple molecules ionizable at the 2.94 μm wavelength. To further demonstrate the applicability of the system, a proof-of-principle reaction was selected, fulfilling the requirements of the system, and was subjected to comprehensive investigation of its performance. Herein, the reaction between N-Boc cysteine methyl ester and allyl alcohol has been performed in a batch reactor and on-line monitored *via* ^{1}H NMR to establish reaction propagation. With the additional assessment, it was confirmed that the thiol-ene coupling can be performed within first 20 minutes of the irradiation with a reaction yield above 50%, proving that the reaction can be applied as a study case to assess the possibilities of the developed system.

Table of Content

Abbreviations

ESI – Electrospray Ionization

DESI – Desorption Electrospray Ionization

FWHM – full width at half maximum

^{1}HNMR – Proton nuclear magnetic resonance

IHM – Indirect Hard Modelling

IM – Ion Mobility

IR – Infrared

LC – Liquid Chromatography

MALDI – Matrix Assisted Laser Desorption / Ionization

MS – Mass Spectrometry

µm – micrometer

µs - microsecond

ms - milliseconds

ns – nanosecond

PAT – Process Analytical Technology

SFC – Supercritical Fluid Chromatography

1. Introduction and Objective

In a fast-developing world with constantly increasing demand for modern chemicals utilized in daily life, their development and analysis play vital roles. Conversely, the demands to develop new chemicals/materials in a safe and sustainable way, with minimized consumption of complex and potentially harmful reagents, become crucial due to possible health hazards and environmental consequences. The high demands to minimize the working volumes to a microscale have given rise to microfluidic devices. Microfluidics provide several advantages, such as, the rapid on-line detection and identification of compounds, low sample and reagent consumption, from an industrial point of view, and high surface-to-volume ratio. The high controllability in sample manipulation that precisely influences the environment at higher reaction rates cannot be underrated from a chemical viewpoint. Especially reactions utilizing fragile (unstable), expensive and sometimes hazardous substances must be well defined before their upscaling and industrial production.[1] A number of biochemical and photochemical reactions require microvolumes to minimize the primary operating cost and prove their reactivity. Hence, on-line monitoring is a key feature. This powerful method allows optimizing crucial parameters influencing the reaction rate before upscaling.[2-5] The on-line interrogation of the sample volume within microdevices has grown to form the so-called lab-on-a-chip approach, allowing for all the steps (including sample preparation, reaction performance, and analysis) in one unit, an efficient compilation of all standard laboratory tasks.[3] Further interest in miniaturized approaches leads to developing and incorporating several different microdevices and interrogation schemes. Still, chip-based analytical systems with electrophoretically driven flows face obstacles in the form of analyte adsorption to walls and interface and optical interference at the walls of containers. Further advances in the field are focussed on delivering systems circumventing contact with the walls within a reasonable interrogation time. One of the approaches utilizes acoustically levitated droplets as microreactors, allowing compartmentalization of liquids, minimizing crosstalk effects, and enabling real-time interrogation of the droplet volume. [6-9]

The choice of acoustical levitation for analytical purposes was not accidental. Acoustical levitation provides several advantages in comparison to other levitation techniques such as optical, diamagnetic, electrostatic, or aerodynamic levitation. It provides compatibility with analytical and bioanalytical approaches, allowing for stable sample handling and accommodates a wide range of sample classes and volumes. Especially important is that acoustical levitation is not limited by the physical properties of the sample and carrier-gas, including ambient conditions. [10-13] The positioning of the droplet in the zone of acoustic silence, where diffusion dominates any occurring mixing effects, allows phase separation between two solvents of different polarities, e.g., to achieve the extraction of analytes of importance in one of the phases inside the single droplet.[14, 15] If mixing is favored, modulation of the carrier frequency can effectively perturb the droplet.[16] Enrichment of the droplet volume is achieved *via* piezo-dispensers, resulting in constant droplet volume with a changing composition, if necessary.[17] All fundamental steps of routine laboratory analysis, such as sample introduction, mixing, separation, preconcentration and sample removal, can be performed on levitated droplets.[18] Hence, the intrinsic properties of the acoustically levitated droplet make it a suitable microreactor.

A large number of analytical techniques have been presented for droplet volume analysis. [19-22] While primarily the focus was placed on optical sensing devices allowing for the detection of analytes without interfacing with the droplet volume, gas-phase detection

schemes, like mass spectrometry (MS), were proposed for biochemical analytics, where a higher level of chemical information has to be embedded in the recorded spectra due to the larger complexity of the involved molecules.[13] MS has matured into a powerful qualitative and quantitative analytical tool with practically no mass limitation. The approach of interrogating the liquid droplet volume with MS – though promising – brings along several obstacles that had to be overcome to pave the road towards a successful application. Like the continuous renewal of the droplet volume, some of them have already been resolved from studies using a coupling of the droplet to optical detection schemes. Here, the highest emphasis was placed on the contactless sampling of the droplet volume and redirecting the analytes to the interrogation scheme. The first attempt to interrogate the droplet volume was presented by Westphal et al., [23] who introduced charge and matrix-assisted laser desorption/ionization to sample and ionize the droplet volume and interrogate the ion plume *via* MS. In that approach, a four-ring electrostatic ring was coupled to a corona needle. The generated corona bursts were used to charge the droplet volume that was further ionized *via* 337 nm laser pulses at ambient pressure.[23] This preliminary method has become the foundation for further developments of acoustically levitated droplet systems coupled with phase-detection schemes at atmospheric pressure. Subsequently, some promising approaches to interrogate the droplets' chemical composition by MS were presented by Warschat et al. and Crawford et al. [24, 25] While the first approach utilizes laser desorption/ionization to contactlessly sample the droplets, in the second, the droplets are disposed on metal mesh and ionized using the DESI approach. So far, only the second method represents the at-line interrogation of chemical reaction performed in the droplet volume at the cost of continuous removal of the reaction volume from the acoustically levitated droplet reactor. The contactless interrogation of the droplet volume allows the treatment of the acoustically levitated droplet as a microfluidic device, the surface of which can be continuously refreshed and fed by reactants to perform chemical reactions and contactless interrogation with the gas phase detection scheme. The MS is one of the techniques applicable, however for many chemical reactions occurring on an ms timescale, IM spectrometry is another possibility. IM spectrometry provides detection on the ms timescale with less instrumental sophistication but never-the-less achieving robust performance. Accordingly, MS and IM spectrometry are two complementary methods. Because it also exploits ion manipulation by electrostatic lenses, most of the recent progress in IM spectrometry can be ascribed to the fast development of MS and related instrumental systems. The analyte identification is unambiguous, however requiring prior information. For the complete identification of the compounds, coupled techniques like IM spectrometry-MS provides impeccable possibilities.[26-29] The primary separation of the analytes occurring inside the IM spectrometer separation device happens according to the shape, size, and structure of the molecules and results in the analytes' packets leaving the drift tube according to their propagation time. Each ion packet reaches the MS where the separation according to m/z allows for identification on the molecular level. Still, the presented techniques need further development to improve their accuracy and reproducibility and fundamental studies to fully understand the mechanisms behind the laser desorption/ionization of liquid droplets inside the acoustic field and the plume propagation between the individual parts of the system under ambient conditions. The main objectives of this thesis are directed to understanding the complex procedure of ion formation *via* laser desorption and deflecting them towards the detection scheme. As a consequence, coupling of acoustically levitated droplets to the IM spectrometer can be ensured *via* tailored solutions in the IM spectrometer interface region to enable the ion uptake under ambient conditions. The improvement and optimization of the system is followed by its real application. Hence a

photochemical reaction capable of occurring within the droplet operating volume needs to be standardized *via* comprehensive techniques. Thus, the reaction of choice was alternatively performed in an ml volume size batch reactor and analyzed using NMR.

2. Theoretical background

2.1. Ion Mobility Spectrometry

The mobility of ions in relation to the strength of the electric field was firstly investigated in 1897 by Rutherford and Thomson. In the following three decades, the effect of collisions, attractive forces, temperature, pressure, accelerating voltage and contamination, on mobilities were identified, leading to the development of a new technique primarily called plasma chromatography. The name originates from the ions (plasma) separated according to chromatography principles and was further replaced with the IM spectrometry.[30] The pronounced development of the technique has started a decade ago leading to its establishment as a powerful analytical tool.[31-33] The characterization of substances in the ion swarm derived from a particular substance depends on its mobility in the electric field under a supporting gas atmosphere. The provided definition is applicable for all conditions of pressure, flow, and compositions of gases, as well as the range of applicable strength of the electric field and ion forming methods. The current approaches utilize a number of geometries and dimensions to generate the electric field and separate the ions.

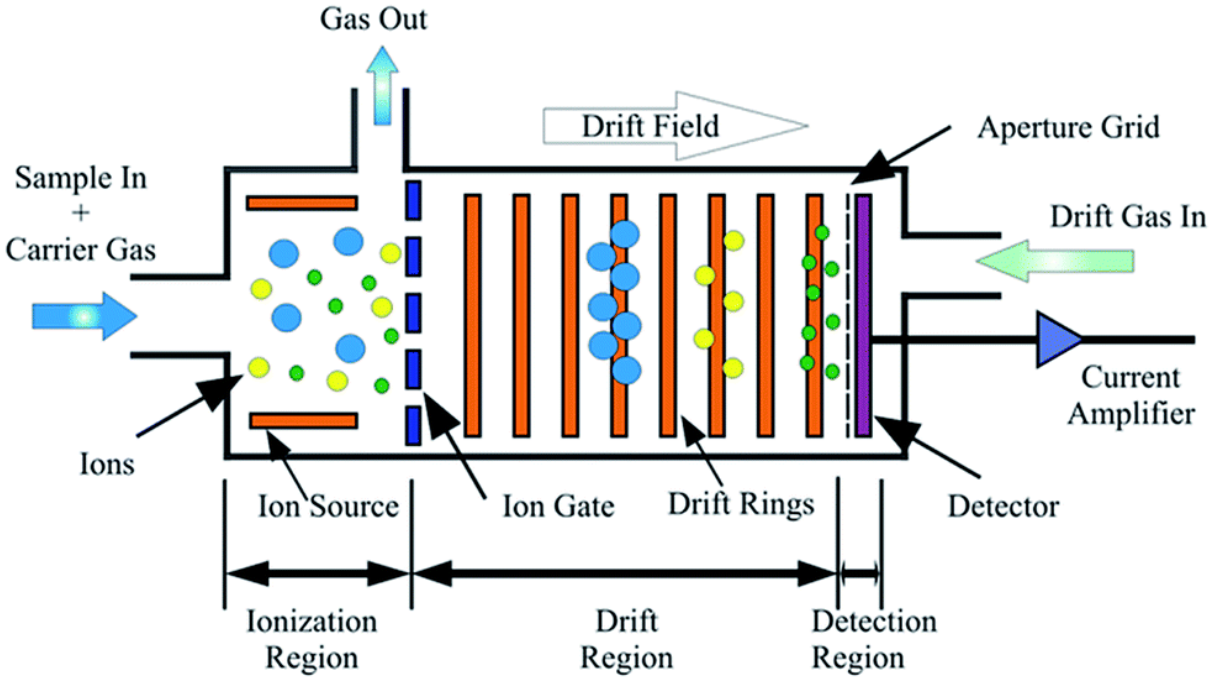

Figure 1. Scheme representing the typical drift tube IMS system, introducing a mixture of three analytes that are separated in the drift cell. The IMS is comprises an ionization region, standard ion gate, drift region and the detector. The drift gas is supplied form the back end of the IMS. The sample is inserted into the ionization region via a carrier gas. [34]

The separation principle in the IM spectrometry is based on the propagation of the ions in the electric field under ambient conditions. The ions are propagating in the voltage gradient against the counter gas. The electric field exerts a force on the analyte ion that is balanced by the friction with the buffer gas, yielding a steady-state ion velocity v_d. The number of effective collisions between the ions and counter gas defines the speed of propagation of the

ions in the electric field (Figure 1.). The velocity v_d of the ions is characterized by the distance d the ion swarm needs to traverse and the required time t_D.

$$v_d = \frac{d}{t_D} \quad (1)$$

The mobility of ions in the electric field is defined by the mobility parameter K, being the drift velocity divided by the electric field

$$K = \frac{V_d}{E} \quad (2)$$

Since the drift velocity is affected by the temperature (T) and pressure (P) in the drift tube, the reduced mobility coefficient represents normalized values at 273 K and 760 Torr.

$$K_0 = K \cdot \left(\frac{273}{T}\right)\left(\frac{P}{760}\right) \quad (3)$$

The presented relationships between drift velocity and electric field are only valid for the measurements performed under the specific combination of a constant gas atmosphere composition, pressure, and temperature at which the ion swarm is thermalized. This behaviour is observed only for low electric fields, remaining approximately ~2 Td, under conditions where the energy gained by the ions undergoing collisions with the supporting gas is greater than the one obtained from the supplied electric field, resulting in ion energies comparable to that of the buffer gas. Under these conditions, diffusion processes are dominant and the velocity of the ions is directly proportional to the electric field.[2]

The reduced mobility coefficients (K_0) originate from the measurements performed in non-clustering media like He and at reduced pressures, in the range of 1 – 10 Torr.[35] Hence, the obtained values accurately account for ion-molecule interactions for measurements under these defined conditions. Normalization of K for pressure and temperature does not describe all conditions. Other factors operating in the drift tube influence the ion-molecule interactions, including gas composition, collisional cross section, and formation of adducts of polar neutrals in gases. The mobility of the ions depends on collisional cross section (Ω) and the number density (N), representing the number of molecules per unit volume, according to the Chapman-Enskog theory as described by the Mason-Champ equation:

$$K = \frac{3}{16}\left(\frac{2\pi}{\mu k_B T}\right)^{1/2} \frac{ze}{N\Omega} \quad (4)$$

where the quantity $\mu = mM/(m + M)$ is the reduced mass of the pair of diffusing ions and carrier gas molecule (with respective masses of m and M), T is the gas temperature [K], z [dimensionless] is the number of elemental charges, e is the elementary charge, and Ω is the collisional cross section. For high values of E/N, the mobility is dependent on the electric field, E. In this situation, the mobility of the ions is represented as:

$$K\left(\frac{E}{N}\right) = K_0 \times \left[1 + \alpha\left(\frac{E}{N}\right)\right] = K_0 \times \left[1 + \sum_{n=1}^{\infty} \alpha_{2n}\left(\frac{E}{N}\right)^{2n}\right]$$
$$= K_0 \times \left[1 + \alpha_2\left(\frac{E}{N}\right)^2 + \alpha_4\left(\frac{E}{N}\right)^4\right] \quad (5)$$

where $K_0 = K(E)_{|E=0}$ is the mobility of the ion in a low electrical field (approaching zero). In the case of low field IM spectrometry, the α function values, describing the dependence of

mobility on the ratio of electric field strength to neutral density are comparable, leading to a constant mobility. Hence, the analytes with similar mobility *K* will result in overlapping peak signals. [34-36]

The collisional cross section parameter, Ω, represents an ion-gas pair and has the dimensions of area. In the case of assessing the collisional cross section, buffer gas plays an important role. The collision profile is dependent on the radius of the buffer gas molecules and cross section. Moreover, the properties of the gas, like temperature *T*, electric field *E*, pressure and specifically *E/N* will influence the ion-gas collision velocity. (37-39)

$$\Omega = \frac{(18\pi)^{1/2}}{16}\frac{ze}{(k_B T)^{1/2}}\left[\frac{1}{m_I}+\frac{1}{m_B}\right]^{1/2}\frac{t_D E}{L}\frac{760}{P}\frac{T}{273.2}\frac{1}{N} \quad (6)$$

A standard drift tube IM spectrometer typically is composed of three units: i) the sample introduction/ionization region, ii) desolvation cell, iii), and drift tube terminated with the ion detector. Historically, the Ni radioactive ionization source was the first proposed, ionizing gaseous samples within the ionization chamber in an effective way and originating from the work of E. Rutherford, performed in 1901, defining ionization of gaseous by X-ray radiation. Further development of IM spectrometry has shown that a chemical ionization and corona discharge can be successfully applied to obviate the need for radioactive sources within the system. This step has opened a new possibility for the IM spectrometry application. The inability to analyse liquid and solid samples in this simple yet effective gas-phase detection system has forced further application of ionization techniques already applied in MS. Hence, the ionization techniques portfolio was increased including electrospray ionization (ESI), matrix-assisted laser desorption/ionization (MALDI), laser ablation etc. [40] Herein, the ESI was of special importance. The possibility to dissolve the sample in nonpolar liquid medium has expanded its applicability as an analytical tool. Practices like subsequent post-ionization of the ion swarm increases the flexibility of analyte interrogation, introducing a new dimensionality.

The ions generated within the ionization region are directed towards the desolvation cell *via* the repeller. The high voltage applied to the repeller focuses the ions spatially. The spatial focusing is necessary to achieve a high number of ions that can be transferred. The desolvation cell and drift tube are separated *via* an ion gate. The ion gate aims to sample the continuous ion swarm into small packets and effect their injection into the drift tube in small time increments. The two most common ion gates are the Bradbury-Nielsen design and Tyndall Powell design. The Bradbury-Nielsen ion gate is one of the most commonly used in IM spectrometers. It consists of two sets of parallel wires, of less than 0.1 mm in diameter, oriented in one plane, providing negligible sizes in the drift tube IM spectrometer design. A small potential is applied to the wires, alternately closing and opening the drift region entrance, where the separation occurs. In the open state, both sets of wires are supplied with the same electric potential pulse allowing the ions to migrate. In this mode, the gate is simply a metal grid, not impeding ion motion. In the closed state opposing electric potential is applied on the wire sets resulting in an electric field perpendicular to the drift direction. Under these conditions, the ions reaching the gate are discharged. [41]

The Tyndall Powell design of the ion gate also consists of wire sets. However, they are located in separate planes with a distance offset of 0,01 mm, up to 1 mm. One of the grids is fixed at a constant electric potential equal to the one remaining in the surrounding field in the IM spectrometer. The second set of wires is supplied with periodic electric potential to create

an electric field used to control the ion movement and inject, in small time increments, the ions into the drift tube.[42]

This challenging task of transferring the ions in small packets into the drift tube region can also be accomplished by applying synchronised pulsed sources, achieving ion sources that simultaneously generate high ion number and operate at high frequencies. One of the possible solutions is the application of laser irradiation for sampling of the probes. Another applicable solution is to feed the ions into the IM spectrometer entrance *via* high frequency, high voltage, pulses, thus generating an electric field responsible for streaming the ions in the desired direction.

The ions thus injected into the drift cell propagate in the electric field, undergoing many collisions with the counterflowing drift gas. The separation occurs according to the shape, size, and structure of ions. Accordingly, bigger unfolded molecules arrive at the detector later due to many collisions with buffer gas, while small and folded molecules arrive earlier due to a small number of collisions, as defined by the difference in the collisional cross section parameter (Ω). The Faraday detector, coupled with the transimpedance amplifier, allows the collection of the current signal, converting it to voltage, and magnifying it. Such a post-treated signal is further directed to an oscilloscope, achieving the final spectrum describing the signal intensity-to-arrival time dependence. The final spectrum represents the number of ions detected on the faraday detector according to their elution time. [37, 43]

2.2. Supporting techniques

To fulfill the aims of the work, additional techniques has been applied to support proper understanding and realization of the project. Such techniques like i) shadowgraphy, ii) ^{1}H NMR have been utilized to give the foundation to the project and allow for its successful performance.

Since the theory behind the techniques is not in the scope of this thesis, in this chapter focus is placed on the brief introduction of the techniques, field of use and the advantages that have classified them as legitimate when discussing the phenomenon behind the laser desorption/ionization of acoustically levitated droplets and reaction performance.

2.2.1. Shadowgraphy

The information about the type of phenomenon behind the irradiation of the droplet surface, fixed in the acoustic field, provides crucial information on how to treat the system, when coupled to the gas phase detection unit. Assessment of the spatial and temporal dissipation of the ion plume allows to define in advance whether additional lensing will be required and define the constrains of the designed hyphenated system.

Technical developments achieved over more than a decade of utilizing high-speed cameras in combination with optical methods, like shadowgraphy, have resulted in their broad applicability for fluid dynamics studies, collectively defined as high-speed imaging. The formation of an ion plume, as well as its spatial and temporal dissipation, can be determined effectively using high speed imaging techniques, providing high spatial resolution with high frame rates.[44] Particularly the shadowgraphy technique has been recognized in this field as being relatively easy, inexpensive yet powerful.[45]

Shadowgraphy is an optical method used to visualize phenomena based on disturbance of refractive index in transparent media. The shadowgraph image consists of a bright

background and a shadow of the interfaces between regions with different refractive index. The bright background is produced due to a lack of interactions between the surrounding medium and the light, while the light refracted at the object interface is dispersed, hence appearing dark in the images [44, 45].

The design of the shadowgraph system should fulfill designated conditions like i) field of view, ii) sharpness and iii) brightness, hence must consider parameters like: i) magnification, ii) light sensitivity, iii) field of view, iv) depth of the field and v) focal length. These are of particular importance and may be restricted by the available equipment.[46, 47]

This visualization technique has been chosen due to its non-invasive and quantitative character, allowing the assessment of the interface speed, direction of motion and object sizes.

2.2.2. ^{1}H NMR

To evaluate the performance of chemical reactions, the ^{1}H NMR technique has been chosen as highly linear, quantitative, and reliable. The ^{1}H NMR technique has lately matured to be reliable for online monitoring and process control as it directly yields both structural and quantitative information, about complex reacting mixtures.[48] For example, it allows tracking of aromatic-to-aliphatic conversions or isomerizations, where alternative conventional methods fail, due to only minor changes in functional groups resulting in such reactions. The application has originated from the on-line coupling of an ^{1}H NMR spectrometer to LC and SFC. To realize the coupling and the flow approach, special flow ^{1}H NMR probes have been developed, introducing a flow option to normally static ^{1}H NMR systems. In the case of on-line reaction monitoring by ^{1}H NMR, the sample is simply bypassed from the reactor to the ^{1}H NMR flow cell. The growing importance of the flow ^{1}H NMR approach in process management resulted in its incorporation into PAT. [49]

In the case of flow ^{1}H NMR, of importance is the incorporation of numerical methods into signal processing. Nowadays, numerical and spectra modelling, or Indirect Hard Modelling (IHM) methods, are applied to avoid linear and non-linear obstacles in the form of spectral shifts, changes in line shape and, most importantly, overlapping signals and low signal intensity. These techniques allow application directly within the production line and without additional standardization. Their application to ^{1}H NMR simplifies the operational procedure as the sample does not need to be spiked with standards, resulting in automated acquisition of spectra and post processing. Hence, providing unambiguous identification of reactand and the reaction rate are easily achievable, both parameters being extremely important in case of future application of the studied reaction and its operational importance. Signal processing utilizing IHM for on-line monitoring of chemical reactions has been already demonstrated to be a reliable method.[50, 51]

This part of the work has been performed in cooperation with Division 1.4 Process Analytical Technology at Bundesanstalt für Materialforschung und – Prüfung, being fully responsible for NMR data acquisition and processing.

3. Publications

3.1. Investigation of mid-infrared laser pulses

Microsecond mid-infrared laser pulses for atmospheric pressure laser ablation/ionization of liquid samples

Aleksandra Michalik-Onichimowska[abd], Toralf Beitz[b], Ulrich Panne[acd], Hans-Gerd Löhmannsröben[bd], Jens Riedel[a]

[a]*BAM Federal Institute for Materials Research and Testing Richard-Willstätter-Straße 11, 12489 Berlin, Germany*

[b]*Physical Chemistry, University of Potsdam, Karl-Liebknecht-Str. 24-25, 14476 Potsdam, Germany*

[c]*Institut für Chemie, Humboldt-Universität zu Berlin, Brook-Taylor-Str. 2, 12489 Berlin, Germany*

[d]*School of Analytical Sciences Adlershof, Humboldt-Universität zu Berlin, Zum Großen Windkanal 6, 12489 Berlin*

Abstract

In many laser based ionization techniques with a subsequent drift time separation, the laser pulse generating the ions is considered as the start time t_0. Therefore, an accurate temporal definition of this event is crucial for the resolution of the experiments. In this contribution, the laser induced plume dynamics of liquids evaporating into atmospheric pressure are visualized for two distinctively different laser pulse widths, $\Delta\tau$ = 6 nanoseconds and $\Delta\tau$ = 280 microseconds. For ns-pulses the expansion of the generated vapour against atmospheric pressure is found to lead to turbulences inside the gas phase. This results in spatial and temporal broadening of the nascent clouds. A more equilibrated expansion, without artificial smearing of the temporal resolution can, in contrast, be observed to follow µs-pulse excitation. This leads to the counterintuitive finding that longer laser pulses results in an increased temporal vapour formation definition. To examine if this fume expansion also eventually results in a better definition of ion formation, the nascent vapour plumes were expanded into a linear drift tube ion mobility spectrometer (IMS). This time resolved detection of ion formation corroborates the temporal broadening caused by collisional impeding of the supersonic expansion at atmospheric pressure and the overall better defined ion formation by evaporation with long laser pulses. A direct comparison of the observed results strongly suggests the coexistence of two individual ion formation mechanisms that can be specifically addressed by the use of appropriate laser sources.

1. Introduction

Infrared laser ablation/ionization (IR-LDI) in vacuum and under atmospheric pressure is a well-established analytical technique for direct isolation of charged molecular aggregates of biomolecules. Recently, a special interest towards atmospheric pressure applications has emerged for the direct analysis of native aqueous solutions [1, 2]. While in most applications mass spectrometry (MS) is the analyser of choice, IMS is an emerging alternative for rapid screening for known target analytes. The most commonly used IR wavelength is the $\lambda = 2.94$ μm output of Er:YAG lasers or optical parametric oscillators (OPO). This wavelength directly induces excitation in the OH/NH stretch vibration modes of many commonly used solvents including water and alcohols. Its simplicity in term of sample preparation and possibility of coupling to high performance liquid chromatography separation technique makes ambient IR-LDI well suited for a liquid phase on-line analysis with ever increasing significance in real life application [3-5].

Despite the ionization the most fundamental process in any laser ablation based detection is the radiation induced liquid (or solid)-gas phase transition. Though extensive studies on thermal evaporation [6-8], pressure induced phase explosion [9-11] and photoablation [11-14] were performed, the exact involvement of the individual mechanisms remains unclear. The laser irradiation leads to a spontaneous local heating of the sample interrogation volume, the accompanying photoacoustic excitation results in a pressure jump. Both state functions, T and P equilibrate within the sample on timescales governed by the sample material transport properties (thermal conductivity and speed of sound, respectively). Typical values for excitation of water with a focused resonant laser are τ_{ac} ~1 ns for acoustic relaxation and τ_{th} ~1 μs for thermal equilibration.

The effect of the laser pulse duration with respect to these relaxation rates has been studied by Dreisewerd et al. [15, 16] for matrix assisted desorption/ionisation (MALDI) in vaccum. According to their observations the nature of IR-LDI is based on the thermal/photo-mechanically induced liquid phase disintegration rather than a pure spallation model previously proposed for vacuum MALDI. The temporal pulse widths studied were 5 ns and 100 ns. For a speed of sound of ~1500 m/s in liquids and a typical penetration depth of several μm these conditions roughly correspond to acoustically confined compared to acoustically unconfined conditions, while thermal confinement was given in both experiments. In vacuum MALDI time of flight (TOF) experiments the pulse width of the ablation/ionization laser defines the temporal (and therefore mass) resolution of the experiment and, thus, has a reasonable upper limit of 100 ns, hence no experiments regarding the effect of thermally unconfined pulses have been conducted.

Modern mass spectrometers coupled to atmospheric pressure exploit a pulsed ion extraction at a continuous sample inlet. In these setups, no upper limit for temporal pulse widths of the used laser is given. In IMS experiments, the experimental resolution is still determined by the temporal definition of the ion formation, however IMS drift times at atmospheric pressure are usually relatively long (several ms) and the resolution of IMS is relatively poor in general when compared to TOF experiments, allowing for the use of microsecond pulse width lasers without affecting the overall resolution of the experiment. Temporal gating of ion flow out of continuous ion sources (like electrospray) has been shown to yield in good resolution utilizing injection times of several hundreds of microseconds [17, 18]. Until now the impact of longer pulse duration, in a μs range, on the temporal behaviour of ion formation elucidating the

analytical applicability has not been studied. However, such lasers recently became available at affordable prices for tissue ablation and cauterization in medical applications [19].

Despite the laser pulse, the sample itself has been found to play a vital role in determining the exact ablation mechanism [20 - 24]. The ablation behaviour was found to be strongly depending on the sample's material properties like viscosity, thermal and acoustic conductivity as well as on its shape, temperature and absolute volume [3, 12, 25 – 29]. These findings have also been rationalized by the dissipation mechanism of the irradiated energy. At a given material the shape of the sample changes the surface tension distribution, any contact with a substrate or vessel introduces ill-defined boundaries perturbing the thermal and acoustic energy equilibration.

In this work mechanism of laser ablation/ionization of liquid sample at atmospheric pressure is exemplary studied for two distinct pulse widths, $\Delta\tau$ = 6 ns and $\Delta\tau$ = 280 µs, at a constant wavelength. The chosen pulse widths correspond to the temporal full width at half maximum (FWHM) of the output of a Nd:YAG driven OPO and the output of a diode pumped solid state Er:YAG laser (DPSS). The chosen pulse width of the DPSS laser of 280 µs was empirically found to result in maximum ionization yield. To minimize the introduction of external perturbations by sample handling, the laser ablation was studied on freely hanging droplets.

The two step ablation/ionization dynamics at the two pulse characteristics were studied by interrogating the resulting ion cloud distribution by two orthogonal techniques. In a first experiment, the mere ablation process was visualized by nanosecond resolution high resolution shadowgraphy. In a second experiment the formed ion clouds were guided through an IMS and detected temporally resolved.

2. Methods

For each experiment, a freshly made sample droplet (acetonitrile/water) was dispensed by a syringe pump (KDS 100, KDS Scientific, Holliston, MA, USA). The sample solution was constantly pumped at 20 µL/min into a home-built microdroplet source consisting of a capillary (Hamilton, ID = 110 µm, OD = 235 µm). The fresh surface of each formed sample droplet was intersected by a pulsed laser beam focused by a plano-convex CaF_2 lens (f = 100 mm). In subsequent experiments, two different laser sources were applied, *I)* an OPO (Opotek inc. Carlsbad, CA, USA) with a pulse duration of $\Delta\tau$ = 6 ns and *II)* a diode pumped solid state Er:YAG laser (Pantec Engineering AG, Ruggell, Liechtenstein) with a variable pulse duration. Throughout the experiments both lasers were operated resulting in comparable fluences. Deviations in fluences were minimized but could not be avoided due to the differences in the individual lasers beam shape and lasing thresholds. For recording the fluences, the pulse energies were determined with a pyroelectric laser power meter, the sizes of the focal spots were determined as burn spots on photosensitive paper followed by visual inspection under an optical microscope. To have constant thermal lensing in all conducted experiments, both laser systems were operated at a constant repetition rate of 20 Hz.

2.1 Shadowgraphy measurements

For a fast visualization of the evaporation dynamics, back illumination was generated by laser induced fluorescence of methanolic rhodamine B solution (25 µM) placed in a quartz cuvette and excited by the second harmonic of the output of an additional Nd:YAG laser (SpitLight 600, Innolas Laser GmbH, Krailling, Germany). The emitted light pulses were of a temporal width of ~ 5 ns and, thus allowed to capture high speed shadowgraphy images with

nanosecond temporal resolution. The plume was imaged through a macroobjective (Tamron SP 90mm F/2.8 Di) with adjustable field of vision onto the detector of a Canon EOS digital camera (400D, Canon Inc., Tokyo, Japan). Two delay generators (DG 535, Stanford Research Systems, Sunnyvale, CA, USA) were used to synchronize the triggering of the individual events. The OPO's flashlamp output signal or Er:YAG laser current source output signal, both operating at 20 Hz, were used as master trigger, initiating the chain of subsequent illumination and camera exposure (figure 1 a)). The camera exposure was triggered *via* a home-built MOSFET circuit using the remote-control release input of the camera. The microdroplet source described above produced droplets hanging on a metal capillary, providing fresh droplets for reproducible conditions for visualization of subsequent laser ablation processes. All recorded images were post processed for optimal contrast and analysed using the ImageJ software suite (National Institute of Health, USA).

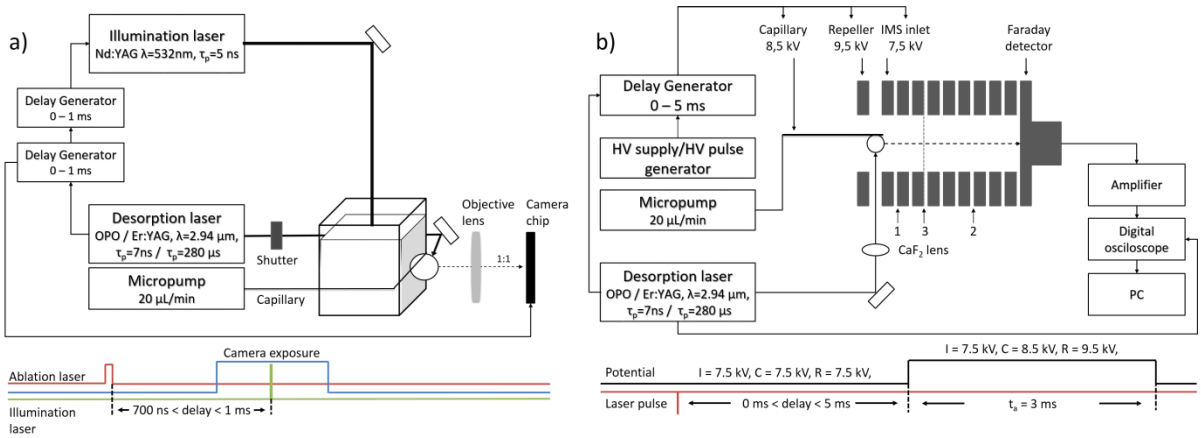

Figure 1. Schematic drawing of the used experimental setups. a) setup for fast high resolution shadowgraphy and triggering sequence applied to visualize evaporation dynamics b) setup for ion mobility interrogation of formed ion plume and representation of a pulsed ion extraction mode.

2.2 Ion mobility spectrometry interrogation

The ablated plume was accelerated coaxially into the opening of a home-built liquid injection drift tube IMS consisting of a desolvation cell (1: L=53 mm, T=180 °C), connected to a drift tube (2: L=80 mm, T=160 °C), *via* a Bradbury-Nielsen type ion grid (3) (figure 1. b)). The IMS is based on the original design described in [30, 31], adopted with a heated gas stream and a desolvation cell as commonly used for liquid sample introduction IMS [32]. Briefly it consists of a tubular arrangement of conductive rings, along which a externally applied electrostatic gradient is realized *via* a series of resistor based voltage dividers. The endcap carries a Faraday plate detector. Along the drift tube separation according to collisional cross section is enhanced by application of a gas stream propagating antiparallel with respect to the electrostatic slope. For an effective transfer of the ablated plume into the IMS a steep voltage gradient was applied: 9.5 kV on the repeller electrode (R), 8.5 kV on the microdroplet source (C) and 7.5 kV on the inlet ring (I). The experiments were conducted in two operating modes: i) by a continuously applied voltage gradient or ii) by pulsed ion extraction into the IMS cell for gated detection. In the latter case all parts of the operated system were kept at constant potential 7.5 kV and pulsed to their respective values (see above) after a specific delay time triggered by the Q-switches of OPO or output signal of the Er:YAG current source (figure 1. b)). For the pulsed extraction, the potential on the repeller was applied *via* a fast transistor

push-pull switch (Behlke Power Electronics, Kronberg, Germany). The laser pathway is adjusted orthogonally to the surface normal of the IMS electrode plates. Because the IMS was used not in order to achieve maximum ion separation but to interrogate the laser induced ion plume distribution, throughout the entire investigation the Bradbury Nielsen ion gate was held open

2.3 Chemicals

The AP-IR IMS comparison studies were performed on tetra-n-butylammonium bromide (TBAB), perphenazine, promazine and L-arginine (supplied by Sigma-Aldrich, St. Louis, MO, USA). In all cases, acetonitrile:water (1:1 v/v) solution was used as a matrix.

3. Results & Discussion

A series of high resolution shadowgraphy images of the ablation dynamics following the droplets excitation with an OPO pulse is depicted in figure 2. In all pictures the laser beam hits the droplet at t_0 (relative delay times are given in the individual images) propagating from the right centre of the pictures. Figure 2 clearly shows the formation of a fine spray consisting of microdroplets. The inset b) in the first figure shows a magnification to single pixel resolution. The used objective, the detector size and the number of its pixels result in an imaging scale of ~1.2 µm/pixel. It can be seen from the inset in the first image that the formed microdroplets range from this minimum determinable droplet size of ~1 µm to 10 µm in diameter.

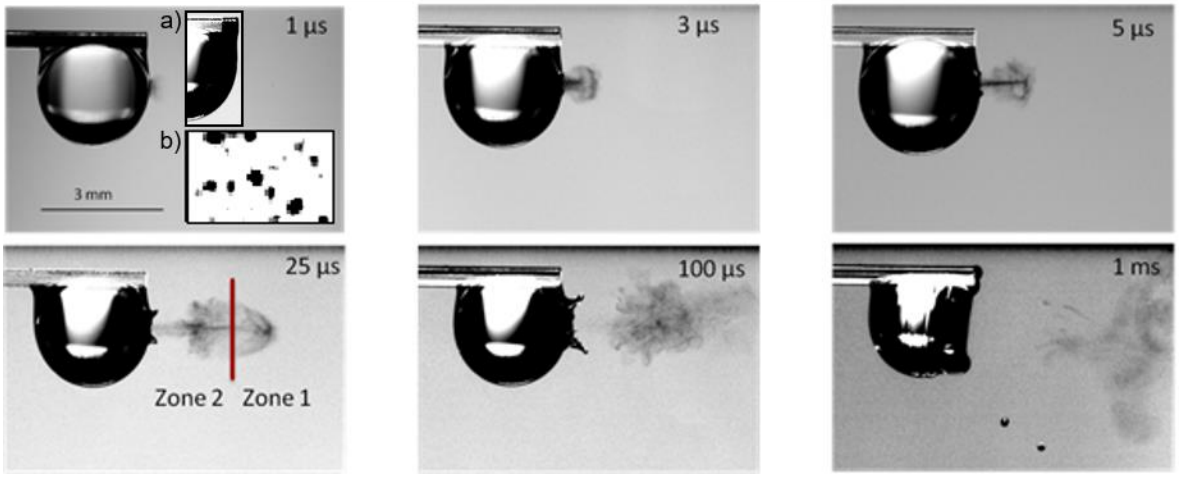

Figure 2. Shadowgraphy images of ablation dynamics following laser excitation with a pulse width of τ_p = 6 ns. Inset a) zoom of the vapour front at t= 700 ns, inset b) close up view on single pixel resolution.

A surprising observation is that the earliest disturbance of the solvent surface can be observed 700 ns after the laser pulse (see inset a) in figure 2). In other words, during the absorption and in the first hundreds of nanoseconds after the absorption of the laser pulse, no laser induced vaporization occurs. This temporal delay cannot be rationalized by a long pressure build up time inside the excited volume in comparison with the excitation pulse alone but has to be caused by a kinetic hindrance of evaporation of the excited volume. Similar observations have been made in the group of Vogel [8, 9]. The first ejected microdroplets occurring in the image after 1 µs can be seen to have travelled up to 300 µm in the 300 ns after the first visible surface distortion. This corresponds to a supersonic average velocity of ~ 1000 m/s.

While in the first image at 1 µs the expanding spray plume is of the typical conical form, already after 3 µs it can be seen to form an acoustic front in which the compressibility of the

surrounding ambient air limits an unperturbed expansion. A close inspection of resulting the "mushroom shaped" expansion plume reveals at least three different regions with characteristic features (*1)* – (*3)*. In the direct vicinity of the droplet's surface, the fumes are forming an ascending column with a diameter of 300 µm, roughly resembling the irradiated surface area *(1)*. At the outmost end of this column the fumes are repelled at a circular acoustic wave front forming the "mushroom cap" *(2)*. This expansion front can be seen to be followed by a zone of rarefaction in which hardly any microdroplets can be found *(3)*. This behaviour is known from supersonic expansions into stationary pressure regions and can be described by the Chapman–Jouguet formalism [33, 34]. It can be seen in explosions, detonations and supersonic expansion experiments. After 5 µs, friction with the surrounding air leads to the formation of toroidal cloud with higher fume concentrations centred around the initial column. After 25 µs the leading pressure wave front, the following torus, and the ejected column start to collapse and a free propagation along the original repulsion trajectory is the main form of fume movement. At this time, a clear separation into at least two regimes is clearly visible leading to a broad spatial distribution. At 100 µs after the laser irradiation, the two regimes can be seen to still continue their movement away from the droplets surface. At this time, the leading fraction of the plume (originally the "mushroom cap") has just left the image while the tailing cloud is slowly expanding while it is following. At the droplet surface, a pronounced liquid crater can be seen, with a wave crest of ~ 500 µm height. 1 ms after the laser impact this deformation of the droplets surface can be seen to have been distributed into large scale surface waves all over the droplet. The picture also shows two larger secondary solvent drops that originate of a breaking up of the crater wave crest. In terms of evaporation efficiency this strong excitation of liquid displacement is a major loss channel. On the right end of the image the last fraction of the fume cloud can be seen to have diffused to a lateral diameter orthogonal to the vector of repulsion of ~ 5 mm.

The presented shadowgraphy images reveal that the supersonic expansion lead to a broad dissipation of the ejected plume along space and momentum in phase space. While the spatial broadening is directly visible in the corresponding images, the broadening in momentum can be estimated by comparison of the travelled distance of the individual fume fractions with respect to the time passed. *Nota bene* the smallest fraction of the yet visible microdroplets are all of comparable size (mass) and, thus, their momentum linearly scales with the velocity. The depicted zones in the image at 25 µs *e.g.* can already be identified in the picture at 3 µs and have been travelling with integrated velocities of 120 m/s (zone 1) and 45 m/s (zone 2), in the subsequent expansion *i.e.* with about threefold lower momentum, respectively.

Another counterintuitive finding is the obvious formation of so called post-pulse ablation. This can be best seen in the figure depicting the expansion after 5 µs. Even though, the laser pulse has been off for 5 µs, a well-defined fume column can be seen to eject from the droplet surface formerly irradiated. This phenomenon is well known from laser treatment of biological tissues in medical applications [9] and was found to be especially pronounced for mechanically weak materials with a low tensile strength. While the exact mechanism behind postpulse ablation is still under debate it is discussed to be the consequence of tight energy confinement. The introduced energy cannot be dissipated within the short period of laser irradiation neither by thermal conductivity, pressure relaxation by acoustic transportation, nor can it be consumed by a phase transition of the excited material. Thus, these three energy loss channels have to be discussed in more detail.

To further elucidate the underlying energetics it is important to estimate the volume of the excited fraction inside the droplet. The focal spot was determined to be 300 µm x 300 µm, the

focal length of the focusing lens was f = 100 mm with a Rayleigh length of several mm resulting in a cylindrical excitation volume. The penetration depth is typically approximated by use of the Lambert absorption coefficient to $\alpha^{-1} \sim 0.8$ µm [27]. However, it could be observed that a thermal excitation of water leads to a weakening of the H…OH hydrogen bonds resulting in a blue shift of the absorption at 2.94 µm. Thus, for high irradiances the absorption coefficient has to be corrected. For the used fluence of 7 J/cm^2 Vogel *et al.* [9] found an empirical value for the penetration depth of $\alpha^{-1} \sim 5$ µm. This leads to a total excited volume of 350 pL that absorbs the 2.5 mJ. Assuming pure water the delivered energy exceeds the energy of the critical point by 3 orders of magnitude leaving the liquid in a supercritical state. The only possible ways for energy dissipation out of the excited volume are *via* transport of heat or excited matter. The limited thermal conductivity of the solvent does not allow for sufficient energy dissipation on the timescale of the laser pulse. The consequence is the formation of an intradroplet shockwave travelling with the speed of sound in the condensed phase. Approximating the speed of sound with the value for water the time it takes to leave the excited volume disk along the 5 µm thickness is ~ 3 ns. The opposing emitted acoustic wave into the droplet induces the recoil of matter equal in momentum towards the droplet/air boundary. This equivalent fraction of energy is removed by material transport into the direction of the neighbouring air resulting in the observed ablation behaviour. This channel is limited by the saturation limit following the Clausius-Clapeyron equation and the subsequent transport of the nascent vapour flow in compressed air. An additional energy loss channel is the kinetic uptake of droplets ejected out of the liquid by the mentioned vapor flow. Once the shockwave in the liquid reaches the liquid/air interface, due to the much lower compressibility the vast excess of energy dissipation will result in evaporation. The maximum evaporation rate is limited. Firstly, solvent from the surface can evaporate into the surrounding atmosphere until the vapour pressure reaches saturation, secondly, the solvent vapour will be transported away from the droplet with a maximum flux eventually limited by the speed of sound in air. After some time, the resulting gas flow will be large enough to overcome the surface tension and the small visible droplets appear. Those droplets are being formed by the Venturi forces of the evaporating gas stream as well as a direct acceleration into the rarefied pressure region behind the gas phase expansion. The mechanism for this formation of nebula is based on macroscopic mechanical effects and will, thus, occur on a much longer timescale than the molecular fume evaporation. The same two step mechanism can be observed in shadowgraphy images of IR rupture of a liquid thin jet recorded by the Abel group [3].

The resulting progeny droplets follow the gas stream away from the surface until they are reflected on the acoustic wave front. The excess of energy in the originally illuminated sample volume leads to a continuation of the evaporation process beyond the timescale of the laser pulse (postpulse ablation). The thermal transport perpendicular to the laser axis (up and down in figure 2) as well as the acoustically driven build-up of a macroscopic crater broadens the column carrying the microdroplets away from the surface to longer delay times until eventually the solvent is in thermal equilibrium and no further progeny droplets are being formed.

It could be seen in figure 2 that even though the ablation was driven by a nanosecond pulse laser, the underlying energy and matter flow dynamics results in significantly slower ablation dynamics. This temporal broadening is also reflected in the formation of the ejected microdroplet plume. In atmospheric pressure ionization applications the main goals are an effective ablation and a spatially and temporally well-defined fume cloud. Because the

temporal and spatial broadening observed in figure 2 is merely explained by the tight energy confinement conditions and a temporally hampered dissipation, the experiment was repeated visualizing the ablation dynamics using a significantly longer laser pulse, in which the heating takes place on a timescale long enough for energy equilibration. Figure 3 shows an equivalent set of images depicting the ablation followed by microsecond laser excitation.

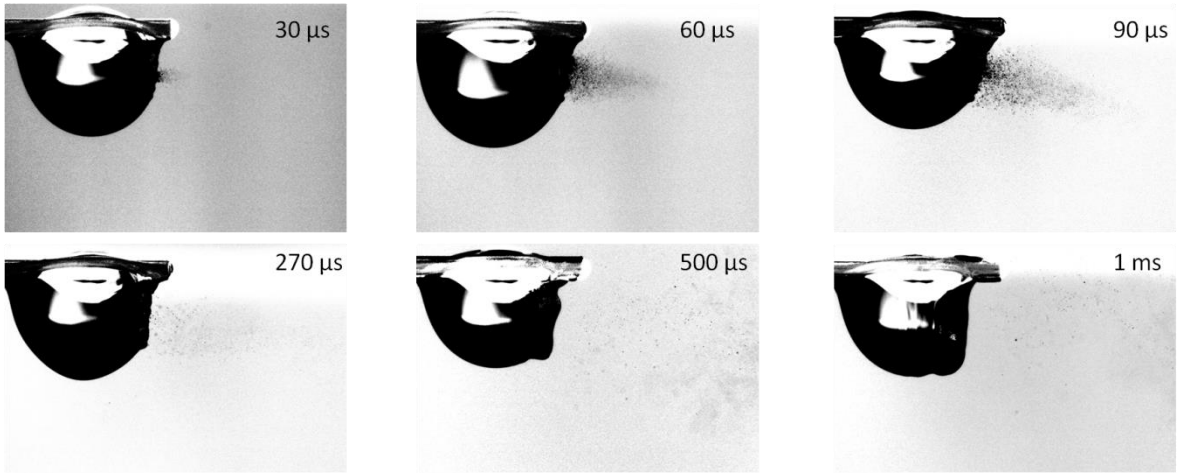

Figure 3. Shadowgraphy images of ablation dynamics following laser excitation with a pulse width of τ_p = 280 µs.

As can be seen, throughout roughly the entire laser pulse duration a droplet ejection can be observed. Here, the initial delay time of ~ 25 µs during which no visible ablation can be observed is somewhat longer than for the nanosecond laser pulse. According to the above discussion, this longer delay could be rationalized by a less rapid evaporation leading in a less pronounced Venturi force of the evaporating solvent. This weaker gas flow takes longer to tear out and carry away microdroplets. Due to higher focal spot size, of 550 µm, larger volume of the droplet is irradiated forming broad descending column of fumes. In contrast to the nanosecond pulse ablation, no distortion of the direct recoil trajectories of the droplets due to shock front or acoustic wave front can be observed. Absence of plume backscattering prevent from rarefraction formation propagating with a much slower velocity than the initial plume front. Though the energy per area supplied by the laser is higher than in case of nanosecond pulses, ~20 J/cm^2, it is distributed over a longer timescale resulting in lower heating rates hence in lower volumetric energy densities. However, the energy provided by the laser pulse is still sufficient to achieve the supercritical state and induce high net mass flux from the droplet surface. This most significant mass ejection from the droplet surface occurs between 30 - 90 µs. Thermally unconfined laser ablation results in plume formation of lower density and unhindered thermal evaporation along the propagation trajectory compared to nanosecond ablation. In the individual images seen in Figure 3, a shrinking of the secondary droplets along the distance of travel can be observed. The absence of the subsequent post-pulse ablation phenomenon is a result of effective heat transfer inside the liquid droplet and reduced recoil-stress. The ejection appears to also induce less recoil stress on the remaining droplet so no crater wave formation or droplet rupture can be observed. The entire series of shadowgraphy images indicate a much more gentle and unperturbed ablation, yet on the same timescale.

For a better visualization of the presence and absence of the crater crest as well as the recoil induced surface waves along the hanging droplet, additional top view images were recorded with a high speed camera (Bonito CL400B, Allied Vision, Exton, PA, USA). Although the

spatial resolution of the recorded frames is much lower, the difference in surface wave excitation is clearly visible. With a total diameter of the droplet of D = 2.5 mm it gets visible that the overall peak-to-peak amplitude of the travelling surface wave induced by the nanosecond laser pulse is on the order of several hundred µm. Thus the volume of the displaced solvent and the needed amount of energy for this displacement is significant. In case of the microsecond laser excitation, the repulsion being distributed over a longer time period seems to result in much lower deformational stress of the remaining droplet.

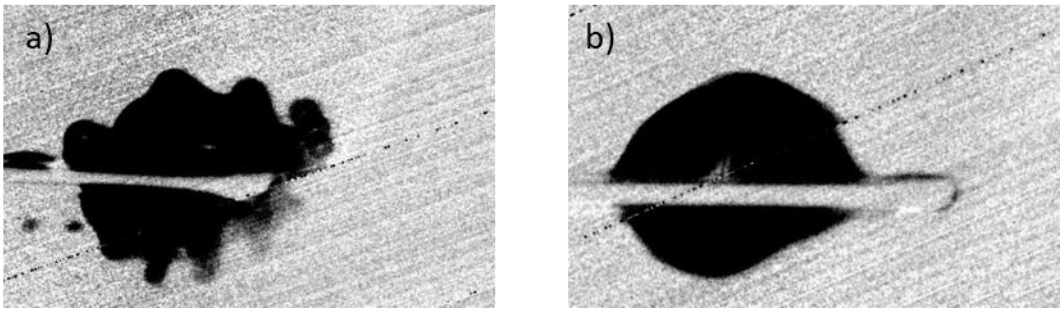

Figure 4. Top view of hanging droplet 280 µs after a) nanosecond laser irradiation and b) microsecond laser irradiation. The horizontal bar in the centre of the images is the capillary for hanging the droplets, the point of irradiation is on the right end of the droplets.

The shadowgraphy images suggest a more homogenous droplet formation by microsecond ablation. Albeit the droplets still vary in size, they follow a much more homogenous distribution in velocity and direction. Also all of them stay in one "cloud" which is only slowly dissipating in space. The expected temporal broadening of the ion formation response function by the longer pulse appears to be of only little effect since in the case of nanosecond ablation the expansion dynamics in combination with the presence of postpulse ablation result in an ion cloud with a comparable temporal width. The spatial distribution of the ejected progeny droplets appears to be much more homogenous in the case of microsecond ablation. For applied fluence ratio Vogel et al. revealed similar propagation behaviour of the plume originating from the confined and unconfined phase explosion conditions [8, 9].

So far, the mere visual inspection only allows for a qualitative observation of the evaporation dynamics. To obtain a more quantitative insight, the experiments were supplemented by a temporally resolved detection of ion formation out of the progeny droplet evaporation. As it is known from sonic spray experiments [35, 36], the ejection of micrometer sized droplets into atmospheric surrounding results in ion formation. Therefore, the progeny droplet formation can be quantitative monitored by detection of the ion release. For this purpose, the evaporated plume was overlapped with the acceptance volume of an ion mobility spectrometer.

3.1 IMS interrogation of the resulting ion plume

A spectral resolution of R ~ 100 (which is sufficient for typical atmospheric pressure IMS experiments) at usual absolute drift times of t_D ~ 10 ms corresponds to an maximal affordable uncertainty of t_0 of $\Delta\tau$ = 100 µs. Still, until now no microsecond laser ablation IMS studies have been conducted [17, 18]. Hence, as a proof of principle the IMS spectra of the test analyte tetrabutylammonium bromide (TBAB) were recorded using the diode pumped Er:YAG laser with different pulse widths in the range of $\Delta\tau$ = 80 µs to $\Delta\tau$ = 280 µs for droplet evaporation with IMS operated with continuously applied voltage gradient. The resulting spectra are depicted in figure 5 a). Due to the design of the specific laser these pulses of different lengths also correspond to different pulse energies. The corresponding fluences for a constant focal spot size of 550 µm diameter as well as the corresponding peak powers are

shown in figure 5 b). They show a linear dependence of the fluence with the pulse length. As can be seen in figure 5 a) below a pulse length of $\Delta\tau$ = 100 µs the laser output is insufficient to obtain spectra. As can be seen in the raw spectra in figure 5 a), with increasing pulse length (i.e. fluence) the ion signal steadily increases. For a more direct visualization this trend is emphasized in figure 5 c) where the peak area as a measure for the total number of ions is plotted against the pulse width. The observed linear increase in ion signal following the increasing laser fluence nicely corroborates the suggested unconfined explosive boiling/ionization mechanism described above. Following a confined mechanism, in contrast, the ion yield could be expected to scale linear with the irradiation peak power. Following the results in fig. 5, all subsequent experiments were conducted with 280 µs pulse length.

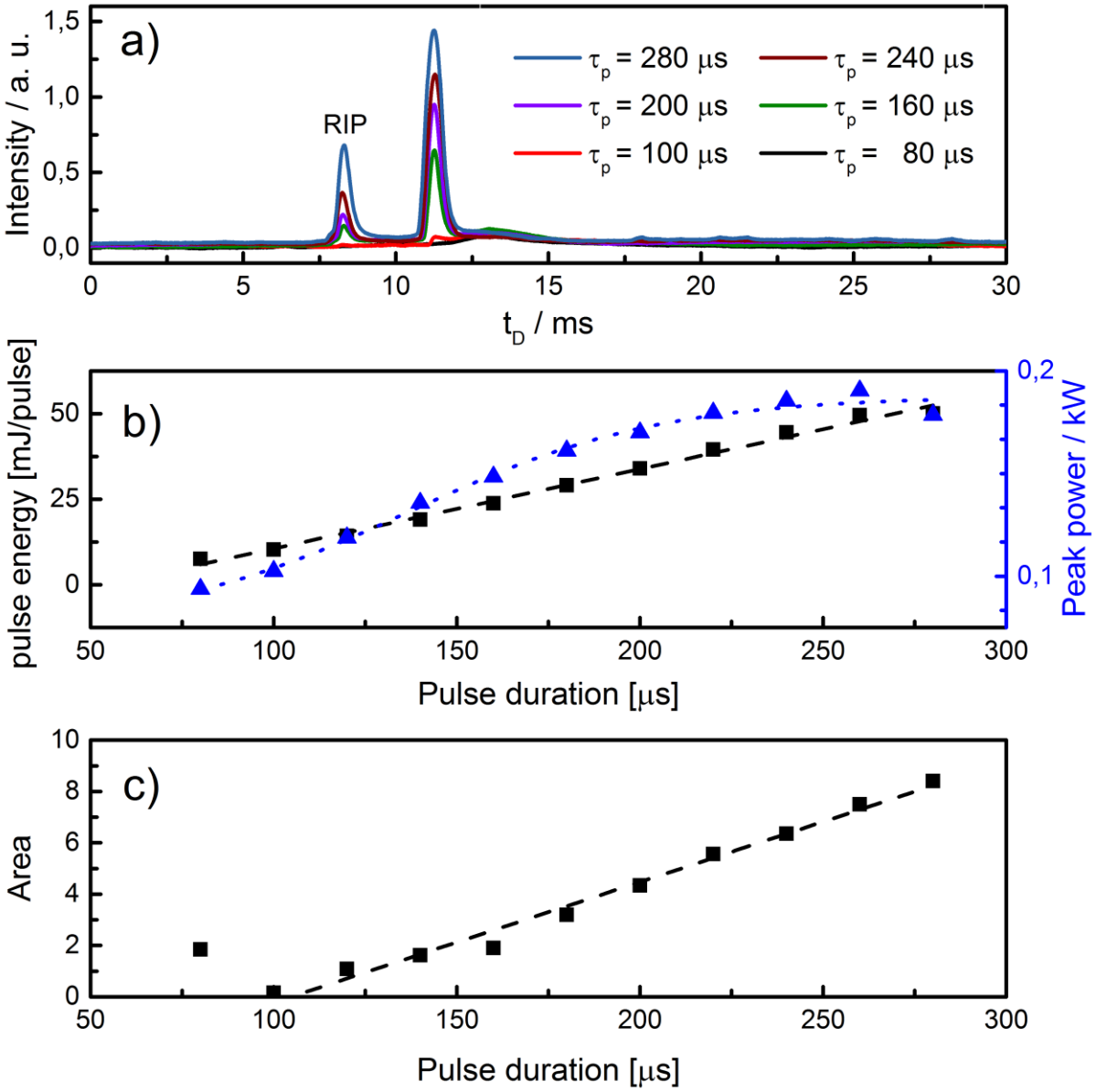

Figure 5. Characterization of Er:YAG laser beam in relation to applied pulse width: a) IMS spectra for different pulse widths; RIP denotes the reactive ion peak of protonated solvent clusters, b) comparison of laser fluence and peak power, c) influence of laser pulse duration on IMS peak area. For b) and c): dashed lines represent linear fits of experimental data; dotted line represents sigmoidal fit of experimental data.

In subsequent IMS experiments two sets of temporally resolved spectra of the antipsychotic pharmaceutical perphenazine were compared that were obtained by laser evaporation with the

Er:YAG laser operating with a pulse width of $\Delta\tau$ = 280 µs and the OPO at $\Delta\tau$ = 6 ns, respectively. The results are shown in figure 6. The individual spectra correspond to different delay times between the laser pulses and the rise time of a pulsed extraction into the IMS analyser. Analysis was performed in a pulsed ion extraction mode to temporally interrogate the nascent ion plume ejected to the IMS probe volume at a specific delay time given in the legend of Figure 6. The spectra at a delay time of 0 µs, thus, are ungated spectra whereas towards longer delays more and more pronounced evolution of the ion releasing progeny droplet fumes leads to a transient change in ion signal. The right column shows the temporal evolution of the integrated analyte ion signal. The first striking difference between the different laser pulse widths is the overall ion signal being roughly 5 fold larger following the OPO induced evaporation. This increase is especially pronounced when considering the fluence of the Er:YAG at $\Delta\tau$ = 280 µs of ~ 20 J/cm^2 in comparison with the OPO fluence of only 7 J/cm^2. A comparison with Figure 5 b) and c) shows that this fluence of 7 J/cm^2 does hardly form any ions when irradiated temporally distributed over 280 µs. Ablation pulses below the time limit of energy dissipation *via* thermal diffusion and phase transition, thus, obviously result in significantly larger ionization efficiency.

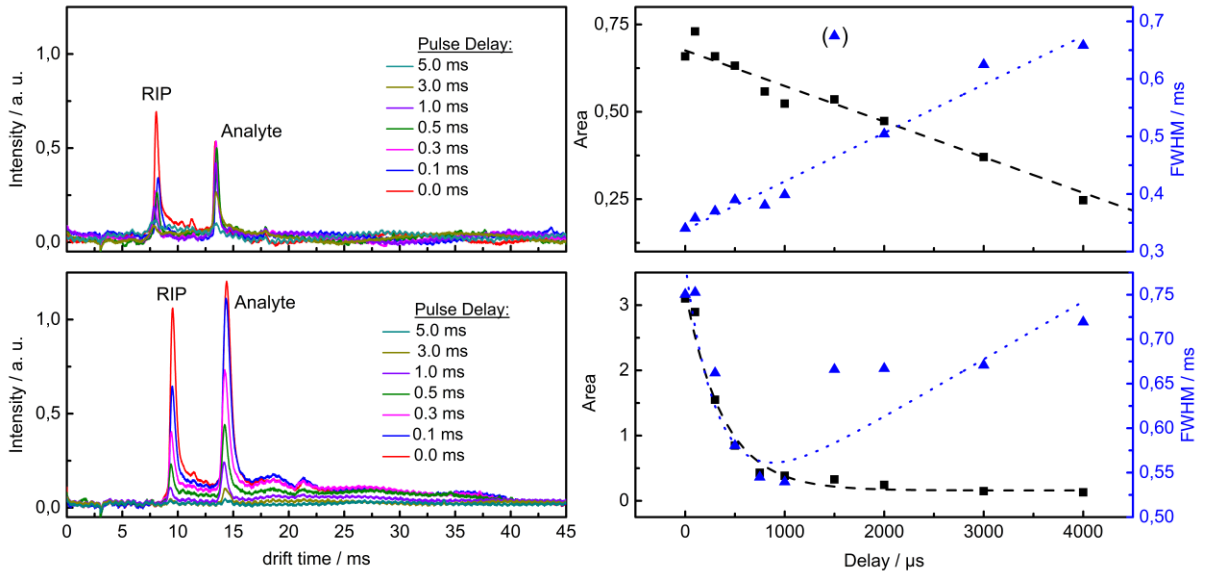

Figure 6. left column: IMS spectra of perphenazine using laser ablation with (upper trace): Er:YAG laser and (lower trace): OPO for different extraction time delays. The peak at shorter drift times is the so called reactive ion peak - in this case protonated solvent cluster signal. right: overall analyte ion signal (area) and temporal width of the analyte peak(FWHM). The dashed and dotted lines in the top right subfigure are linear fits to the experimental results (data point in brackets omitted as outlier). The dashed line in the lower right subfigure shows an exponential fit to the experimental data (τ = 380 µs ± 45 µs), the dotted line shows a superposition of an exponential decay (τ = 330 µs ± 120 µs) and the linear behaviour observed for the µs pulsed laser. The total ion intensities in all subfigures are normalized by the same factor.

The second striking difference is the temporal behaviour of the ion yield over delay time. Unconfined phase explosion induced by the microsecond pulse exhibits a linear decrease in detected ions towards longer delay times. This nicely confirms the undisturbed evaporation observed in the shadowgraphy experiments to be the only mechanism. The observable ion detection loss occurs on a long timescale with a slope of ~ 1/10 ms. A close comparison with the plume visualization in figure 3 indicates that this loss channel is most probably simply

dissipation of the progeny droplets out of the interrogation volume of the IMS analyser. The nanosecond pulse ablation on the other hand leads to a bimodal distribution of the transient ion detection efficiency. The first contribution shows an exponential decay in ion abundance with a time constant of $t \sim 380$ µs. The second contribution to ion formation can be observed at longer delay times between the laser pulse and ion extraction and exhibits a linear decrease. The latter shows a strong resemblance to the diffusion driven dilution observed for the Er:YAG laser case. The first channel temporally coincides with the "mushroom" formation and is assigned to originally supersonically expanding plume front. A loose temporal correlation can characterize the two contributions in the bimodal distributions in both ion yield and FWHM to be originating from the two distinctively separated zones indicated in figure 2.

As can be also seen in figure 6 the signal peaks in the ion drift time distributions obtained in the OPO ablation experiments experience a more pronounced broadening. Experimentally this broadening could stem from a Coulomb repulsion, phase space dissipation of the decelerated ions along either momentum or place of origin or incomplete desolvation. Coulomb repulsions are limited to high ion densities. According to the set of images presented in the figure 3 the plume density decrease with increasing plume propagation time leading to reduction of the Coulomb interactions. Hence charge repulsion would have limited influence on peak broadening after longer delay times. The mentioned incomplete desolvation would also be expected to be especially pronounced in early detection gate experiments because desolvation occurs throughout the delay as well. The latter dispersion in phase space could already be seen to go along the thermally confined laser ablation in figure 2. Hence, this mechanical recoil induced particle dissipation along the phase space is postulated to be the major contribution for temporal broadening of the IMS instrument response function in thermally confined laser ablation experiments. Just as described for the shadowgraphic depiction above, the large amount of turbulent flow that follows a directed supersonic expansion at atmospheric pressure "smears out" the plume along their position and momentum vector in phase space. Since in analytical IMS applications this broadening determines the spectral resolution of the spectrometer, an ionization scheme resulting in temporally narrow ion peaks on the detector is typically favourable. The analyte ion peak width distribution of the microsecond pulse ablation scheme exhibits a minimum at short delay times that systematically grows towards longer plume dissipation. This trend can be attributed to the observed overall decrease in the number of detected ions and the corresponding decrease in signal-to-noise ratio. In the nanosecond experiments the distribution of the peak widths again suggests the existence of two superimposed ion formation moieties. While at later times the increase in peak width can be described by the same mechanism as in the microsecond laser experiments, at early gate times, the energy confinement leads to additional mechanical vapour formation that yields in higher ionization efficiency at the cost of peak broadening. Noteworthy, the peak broadening scales oppositely with the overall ion intensity in the two individual channels. While in the late ion formation assigned to thermal ionization the largest ion yield corresponds to the narrowest peak shape, in the early ion channel – postulated to be driven by mechanical recoil – the FWHM is directly proportional to the observed total ion count. This strengthens the postulate that two different ion formation mechanisms are responsible for the individual ion release moieties. In the thermal ion formation, the ionization barrier is overcome by internal energy. In this way, no additional phase space dissipation is caused. Opposingly, in case of the mechanical stress formation the barrier is overcome by kinetic energy of the progeny droplets and, thus, the ion occurrence should scale proportionally with the released ion momentum. While at first this

momentum vector is directed, *i.e.* all particles of the ensemble have the same position and momentum (corresponding to a dense packing in phase space), throughout the plethora of experienced collisions the particles experience more and more pronounced relative velocities and density in phase space is lost.

In summary, the best performance in terms of overall ion yields is achieved by the use of nanosecond laser ablation/ionization. However, the best spectral resolution is obtained by using microsecond pulsed lasers. At first this may appear somewhat counterintuitive since short laser pulses result in temporally broadened signals but can be readily understood when looking at the shadowgraphic visualization of the formed plume propagation. While for low signal experiments like trace analysis the ionization yield is the most important figure of merit and nanosecond lasers are the best choice, in some cases, when a spectroscopic differentiation between two coexisting analytes is wanted, lasers that exhibit a longer pulse width become favourable.

4. Conclusions

The temporal spread of vapour clouds out of atmospheric pressure laser ablation was found to strongly depend on the temporal confinement of the used laser pulses. Short pulses, somewhat surprisingly, lead to a pronounced broadening of the formed droplet plume in space and momentum while long pulses were found to form a homogenously distributed laser spray plume. The same temporal behaviour was found in the arrival time distributions of ions originating from the laser ablation in supporting IMS experiments. In combination, the results strongly suggest the coexistence of two ionization pathways, in which thermal (internal) energy and the other mechanical (kinetic) energy is the major driving force over the ionization barrier. The latter was found to be more effective in generating ions, however, yields in ions with large kinetic access energy. This leads to a dissipation of the nascent ions along phase space, which eventually results in spectra broadening in drift time experiments as IMS or time of flight experiments. Finally, it can be said that it is recommendable to use longer laser pulses in experiments, where the limits of detection are not as important as the spectral resolution.

Acknowledgments

Authors are indebted to Carsten Warschat for fruitful discussion and Martin Zühlke for help in performing some of the experiments. This work was financially supported by the Excellence Initiative of the German Research Foundation (DFG).

Bibliography

1. V. V. Laiko, N. I Taranenko, V. D. Berkout, M. A. Yakshin, C. R. Prasad, H. Sang Lee, V. M. Doroshenko, J. Am. Soc. Mass Spectrom., 2002, 13, 354 – 361
2. S. C. Moyer, L. A. Marzilli, A. S. Woods , V. V. Laiko, V. M. Doroshenko, R. J. Cotter, Int. J. Mass Spectrom., 2003, 226, 133–150
3. A. Charvát, B. Stasicki, B. Abel, J. Phys. Chem. A, 2006, 110, 3297-3306
4. A. Charvát, E. Lugowoj, M. Faubel, B. Abel, Eur. Phys. J. D, 2002, 20, 573 – 582
5. E. Rapp, A. Charvát, A. Beinsen, U. Plessmann, U. Reichl, A. Seidel-Morgenstern, H. Urlaub, B. Abel, Anal. Chem. 2009, 81, 443–452
6. A. D. Zweig, J. Appl. Phys., 1991, 70, 1684 - 1691
7. A. Miotello, R. Kelly, Appl. Phys. A, 1999, 69, S67 – S73
8. I. Apitz, A. Vogel, Appl. Phys. A, 2005, 81, 329 - 338
9. A. Vogel, V. Venugopalan, Chem. Rev., 2003, 103, 577 - 644
10. X. Fan, K. K. Murray, J. Phys. Chem. A, 2010, 114, 1492 - 1497
11. L. Zhigilei, B. J. Garisson, J. App. Phys. 2000, 88, 1281 – 1298
12. A. A. Oraevsky, S. L. Jacques, F. K. Tittel, J. Appl. Phys., 1995, 78, 1281 - 1290
13. G. Paltauf, P. E. Dyer, Chem. Rev., 2003, 103, 487 – 518
14. D. Feldhaus, C. Menzel, S. Berkenkamp, F. Hillenkamp, K. Dreisewerd, J. Mass Spectrom., 2000, 35, 1320 – 1328
15. C. Menzel, K. Dreisewerd, S. Berkenkamp, F. Hillenkamp, J Am. Soc. Mass Spectrom., 2002, 13, 975-984
16. A. Leisner, A. Rohlfing, U. Röhling, K. Dreisewerd, F. Hillenkamp, J. Phys. Chem. B, 2005, 109, 11661-11666
17. T. Reinecke, A. T. Kirk, A. Ahrens, C. – R. Raddatz, C. Thoben, S. Zimmerman, Talanta, 2015, 150, 1-6
18. M. Zühlke, D. Riebe, T. Beitz, H. – G. Löhmannsröben, K. Zenichowski, M. Diener, M. W. Linscheid, Eur. J. Mass Spectrom. 2015, 21, 391 - 402
19. J. T. Walsh, Jr., T. J. Flotte, T. F. Deutsch, Lasers, Surg. Med., 1989, 9, 314 - 326
20. C. Menzel, K. Dreisewerd, S. Berkenkamp, F. Hillenkamp, Int. J. Mass Spectrom., 2001, 207, 73-96
21. G. Robichaud, J. A. Barry, D. C. Muddiman, J. Am. Soc. Mass Spectrom., 2014, 25, 319-328
22. T. A. Schmitz, J. Koch, D. Günther, R. Zenobi, J. Appl. Phys., 2011, 109, 123106
23. K. Dreisewerd, S. Berkenkamp, A. Leisner, A. Rohlfing, C. Menzel, Int. J. Mass Spectrom., 2003, 226, 189-209

24. C. Warschat, A. Stindt, U. Panne, J. Riedel, DOI: 10.1021/asc.analchem.5b01495

25. K. Dreisewerd, Chem. Rev., 2003, 103, 395 - 425

26. A. Charvát, B. Abel, Phys. Chem. Chem. Phys., 2007, 9, 3335-3360

27. A. Rohlfing, C. Menzel, L. M. Kukreja, F. Hillenkamp, K. Dreisewerd, J. Phys. Chem. B 2003, 107, 12275 – 12286

28. A. Rohlfing, A. Leisner, F. Hillenkamp, K. Dreisewerd, J. Phys. Chem. C, 2010, 114, 5367 - 5381

29. M. W. Sigrist, J. Appl. Phys., 1986, 60, R83

30. C. Illenseer, H. – G. Löhmannsröben, Phys. Chem. Chem. Phys., 2001, 3, 2388 – 2393

31. C. Brendler, D. Riebe, K. Zenichowski, T. Beitz, H.-G. Löhmannsröben, Int. J. Ion. Mobil. Spec., 2014, 17, 105 - 115

32. T. Khayamian, M. T. Jafari, Anal. Chem. 2007, 79, 3199-3205

33. R. E. Duff, E. Houston, J. Chem. Phys., 1955, 23, 1268 – 1273

34. B.V.Voitsekhovskii, V.V.Mitrofanov, M.E.Topchiyan, Comb., Explos. Shock waves (Engl. Transl.), 1969, 5, 267 – 273

35. M. M. Antonakis, A. Tsirigotaki, K. Kanaki, C. J. Milios, S. A. Pergantis, J. Am. Soc. Mass Spectrom., 2013, 24, 1250 - 1259

36. A. Stindt, C. Warschat, A. Bierstedt, U. Panne, J. Riedel, Eur. J. Mass Spectrom, 2014, 20, 21–29

3.2. ^{1}H NMR on-line reaction monitoring

‘‘Click” analytics for ‘‘click” chemistry – A simple method for calibration–free evaluation of online NMR spectra

Aleksandra Michalik-Onichimowska [a,b,d,1], Simon Kern [a,1], Jens Riedel [a], Ulrich Panne [a,c,d], Rudibert King [e], Michael Maiwald [a],

[a] *Bundesanstalt für Materialforschung und -prüfung (BAM), Richard-Willstaetter-Str. 11, D-12489 Berlin, Germany*

[b] *Physical Chemistry, University of Potsdam, Karl-Liebknecht-Str. 24-25, 14476 Potsdam, Germany*

[c] *Institut für Chemie, Humboldt-Universität zu Berlin, Brook-Taylor-Str. 2, 12489 Berlin, Germany*

[d] *School of Analytical Sciences Adlershof, Humboldt-Universität zu Berlin, Zum Großen Windkanal 6, 12489 Berlin, Germany*

[e] *Department Measurement and Control, Institute of Process Engineering, Berlin University of Technology, Hardenbergstr. 36a, 10623 Berlin, Germany*

[1] *Shared first authorship*

Abstract

Driven mostly by the search for chemical syntheses under biocompatible conditions, so called ‘‘click” chemistry rapidly became a growing field of research. The resulting simple one-pot reactions are so far only scarcely accompanied by an adequate optimization via comparably straightforward and robust analysis techniques possessing short set-up times. Here, we report on a fast and reliable calibration-free online NMR monitoring approach for technical mixtures. It combines a versatile fluidic system, continuous-flow measurement of 1H spectra with a time interval of 20 s per spectrum, and a robust, fully automated algorithm to interpret the obtained data. As a proof-of-concept, the thiol-ene coupling between N-boc cysteine methyl ester and allyl alcohol was conducted in a variety of non-deuterated solvents while its time-resolved behaviour was characterized with step tracer experiments. Overlapping signals in online spectra during thiol-ene coupling could be deconvoluted with a spectral model using indirect hard modeling and were subsequently converted to either molar ratios (using a calibration free approach) or absolute concentrations (using 1-point calibration). For various solvents the kinetic constant k for pseudo-first order reaction was estimated to be 3.9 h^{-1} at 25°C. The obtained results were compared with direct integration of non-overlapping signals and showed good agreement with the implemented mass balance.

Keywords: NMR spectroscopy, reaction monitoring, automated data evaluation, thiol-ene click chemistry

1. Introduction

Currently research in chemical manufacturing moves towards flexible plug-and-play approaches focusing on modular plants, capable of producing small scales on-demand with short downtimes between individual campaigns. This approach allows for efficient use of hardware, a faster optimization of the process conditions and, thus, an accelerated introduction of new products to the market [1]. These systems benefit from integrated processing and control, which translates to increased safety and improved product quality, when appropriate techniques for real-time analytics are applied. This maximization of efficiency of chemical processes efforts goes hand in hand with a synergetic reduction of the negative impact of chemical analyses on the environment and to enable implementation of sustainable development principles to analytical laboratories [2]. Principles for green analytical chemistry comprise among others in situ measurements, automated and miniaturized methods as well as multi-analyte methods. All these approaches share the concept of minimizing the sample volume needed for a reliable interrogation. Techniques employing optical properties of molecules, e.g. Raman spectroscopy, IR spectroscopy, UV–VIS spectroscopy, are most commonly applied since they work fast and nondestructive. Albeit they can be integrated inline into the process stream, their real-life applicability is often hampered by problems connected to baseline shift, high background signals and the need for matrix matched standards for calibration. An alternative to the conventional optical techniques is quantitative NMR spectroscopy applied in flow through mode, which recently matured to a reliable technique for online monitoring and process control [3–5]. NMR spectroscopy can provide structural and quantitative information directly inside complex reacting multicomponent systems. It is able to obtain information in technical processes, where aromatic-to-aliphatic conversions or isomerizations occur and conventional methods fail due to only minor changes in functional groups. On behalf of its strict linearity between the number of NMR active nuclei and the detected peak area, which is independent of the matrix, online one-dimensional NMR methods show great potential to obtain quantitative information without timeconsuming calibration effort. Ideally, direct integration is the method of choice to extract peak information from spectra when well resolved peaks acquired with stable baseline. Quantitative information can be obtained from ratio of peak area resulting in relative molar ratios or by the use of a concentration conversion factor for the calculation of absolute molar concentrations [6]. Even in the case of partially overlapping signals least squares fitting algorithm and global spectrum deconvolution could successfully be applied for retrieving the individual peak integrals as occurring in an baseline-resolved unperturbed spectrum [7]. Additionally, when it comes to limited chemical shift dispersion leading to strong peak overlaps, ultrafast two-dimensional NMR approaches for reaction monitoring have been successfully demonstrated in literature [8,9]. Besides problems introduced by signal overlapping in industrial applications of NMR instruments, the automated evaluation of online NMR spectra is often challenged by non-linear effects such as spectral shifts and changes in line shapes. The latter are caused by magnetic field inhomogeneities, or large variations in temperature, pH and pressure. Successful online NMR approaches additionally require to overcome problems related to low signal intensity. The resulting long signal acquisition times become especially critical for monitoring of fast reactions occurring on a timescale of minutes [10]. Linear multivariate methods like partial least square regression (PLS-R) are widely used in industrial applications – often combined with binning in order to compensate variations in the spectra [11–13]. PLS-R performs a data reduction for functionally correlated data by finding factors in the NMR spectra which are also relevant for the quantitative information of the spectra. This is realized by determining a set of latent

variables with the constraint that these components explain as much as possible of the covariance between the NMR spectra and the quantitative information. PLSR models can be used for many variables but represent major obstacles in model extrapolation and require a high calibration effort. For the consideration of non-linear effects and fully overlapping signals, spectral modeling based on so-called Indirect Hard Modelling (IHM) shows great potential [14,15]. This forward convoluting spectral analysis method uses parametrized peak functions to produce flexible spectral models of each component, which appear during reaction monitoring (pure component models). Thereby, the spectrum of a chemical mixture can be composed of the weighted sum of various component models allowing for correction of nonlinear effects. The obtained superposition of peak functions is then iteratively adapted to the recorded spectra via least squares algorithms. Subsequently, the weights of these component models in a mixture spectrum can be utilized to construct linear calibration model based on Beer's law. In contrast to most soft modeling methods (e.g. PLS-R) in IHM the physical structure of the spectrum is considered by fixing the peak area ratio in each pure component model during spectral evaluation. Successful application of IHM to low-field NMR spectra by the use of a linear calibration function has been recently presented in the literature [16,17]. However, since IHM relies on the fitting with parametrized peak functions, potential for the use of these functions and its area for calibration-free approaches is not fully exploited. To proof its applicability, a reaction scheme providing transformation in a minute/hour timescale was investigated in this study. Thiol-ene coupling offers the above mentioned property and additionally can be highly modified at a small efficiency cost. It is a group of well-established ''click" reactions characterized by high conversion rates with reduced degree of by-products formation [18]. Its growing industrial significance for synthetic and material developments impose monitoring when performed on large scale to ensure product quality and optimize the conditions [19–21]. Typical for ''click" chemistry, its reaction performance is not restricted to organic solvents and potentially toxic metal-based catalysts. Its feasibility at room temperature in environmentally benign solvents or aqueous solution is only restricted by the solubility behaviour of the applied catalyst. Of special relevance is a fact that reaction may be initiated by photo-catalysis operated at a near visible wavelength (VIS). A number of approaches at different wavelength were proposed to enhance conversion yields and reaction rates [22]. Still at near-VIS complete reactant transformation may be achieved well below an hour providing optimal conditions for our online NMR spectroscopy test bed. The Thiol-ene coupling between N-boc cysteine methyl ester and allyl alcohol activated at λ = 365 nm was chosen as model system. Data achieved by online NMR spectroscopy were processed using direct integration and IHM to show superiority of the latter for fast assessment of compounds concentration without prior calibration.

2. Materials and methods

2.1. Materials

The chemicals allyl alcohol (≥ 99 %, CAS 107-18-6), N-boc cysteine methyl ester (97 %, CAS 55757-46-5), and 2,2-dimethoxy-2-phenylacetophenone (99 %, CAS 24650-42-8) were supplied by Sigma-Aldrich (Steinheim, Germany) and were used without prior purification.

2.2. Reaction conditions

Thiol-ene coupling was performed between N-boc cysteine methyl ester and allyl alcohol in ratio of 1 to 2.5 M equivalences, respectively. 0.1 mol of 2,2-dimethoxy-2-henylacetophenone (DMPA) was added as photoinitiator (see Fig. 1).

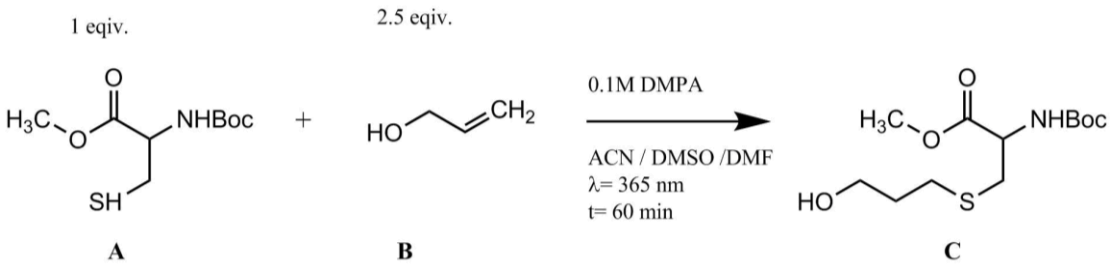

Fig. 1: Reaction mechanism of the thio-ene coupling – A: N-Boc cysteine methyl ester, B: allyl alcohol, C: thioether product

To evaluate the reactions dependence on the surrounding polarity, acetonitrile (ACN), dimethylformamid (DMF), and dimethyl sulfoxide (DMSO) were used as non-deuterated solvents. 0.02 mol of N-Boc cysteine methyl ester and 0.05 mol of allyl alcohol were mixed in a 20 mL measuring flask and filled with a solvent. The photoinitiator was added to the same respective solvent (2 mmol of DMPA). Prepared reaction mixtures were mixed for 5 minutes and transferred to the batch reactor of 20 mL volume. To maintain constant conditions during reaction monitoring a stirred glass reactor was thermostated at 25 °C. Irradiation was performed for 60 min utilizing a high intensity mercury-xenon lamp (Lightningcure LC8, Hamamatsu Photonics, Hamamatsu City, Japan) with a maximum band intensity at 365 nm. A light guide (quartz glass) was immersed inside the batch reactor to provide uniform irradiation conditions.

2.3. Online monitoring set-up

The experimental set-up for reaction monitoring utilizing 500 MHz NMR spectrometer (Varian Associates, Palo Alto, CA, USA) is presented in Fig. 2. The NMR spectrometer was coupled to a glass reactor (C1) via thermostated PTFE tubing. The circulation of the reaction mixture in between the reactor (C1, 50 mL) and the NMR spectrometer was induced using dosing pump (P1, HPD Multitherm 200, Bischoff Chromatography, Leonberg Germany). The circulation was split in two loops: (i) a fast loop providing flow rate of 6 mL min^{-1} for rapid sample transfer from the reactor to the NMR instrument, and (ii) a slow loop of 0.4 mL min^{-1} flow rate resulting in quantitative and pulsation free flow inside the NMR instrument. The latter was obtained by a coriolis massflow controller (FIC, mini Cori-Flow, Bronkhorst High-Tech B.V., Ruurlo, NL) providing accuracy of ±0.2% of rate. The reactor as well as the tubing were temperature controlled by a thermostat. In order to prevent solid impurities from entering the tubing system a 15 mm filter (F1) was installed (FISS-FL2-15, FITOK GmbH, Germany) behind the outlet of P1. All spectra were acquired using a 500 MHz spectrometer with a dual band flow probe having a 1/16-inch polymer tubing working as a flow cell. Single scan 1H spectra were recorded with an acquisition time of 5 s, relaxation delay of 15 s and a spectral width of 13.25 ppm.

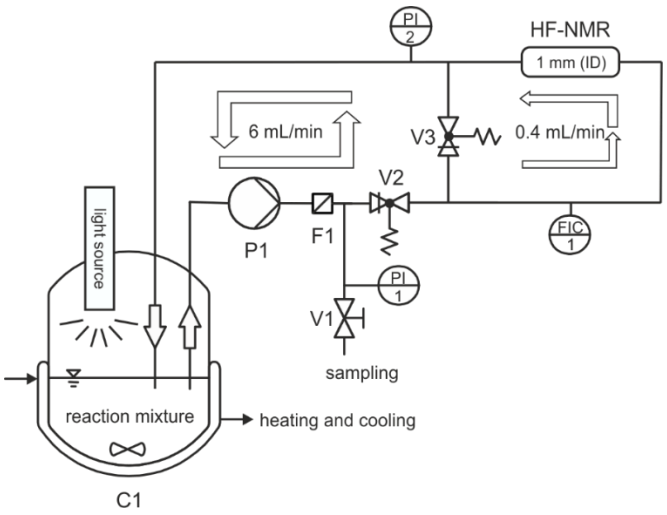

Fig. 2: Flow diagram of the experimental set-up including the by-pass system for online NMR measurements using a 500 MHz NMR spectrometer in continuous flow mode. The bypass stream in between the spectrometer and C1 (50 mL) was split in a fast loop (6 mL/min) and slow loop (0.4 mL/min).

2.4. Determination of residence time distribution

The flow velocity in the active region of the NMR spectrometer has a great influence on signal intensity when operating in continuous flow mode. The critical flow rates to assure fully magnetized analyte nuclei can be determined by iterative optimization of the normalized signal integral [23]. The resulting comparatively low flow rate providing sample to the NMR in the slow loop (0.5– 2 mL min^{-1}) for the flow probe in use and the volume of the tubing system (1.9 mL, 9.5% of the total applied volume) cause a certain response time of concentration variations in the stirred reactor. In the interest of characterizing the mixing behaviour and residence time distribution (RTD) in detail, a step tracer experiment was conducted by using acetone as tracer. The reactor system, with settings described as in Section 2.3, was filled with 20 mL of ACN and 5 mL of acetone was added instantaneously while its propagation in the system was monitored by NMR. The cumulative distribution F(t) can directly be obtained from the concentration profile of the tracer over time, while the residence time distribution E(t) was calculated by the numerical gradient of F(t). During step tracer experiment, the tracer solution in the stirred tank gets diluted from fresh solvent returning from the bypass system to the stirred tank. By this, the resulting curve of E(t) shows the expected oscillation for closed recirculation systems due to re-dilution [24]. For the classification of data into residence time affected and non-affected the following values can be obtained from F(t) as indicated in Fig. 3. The transfer time (t_{trans} = 1.5 min) – the time after which the first amount of tracer cover the distance from the reactor to the active region of the NMR magnet, the delay time (t_{delay} = 3.8 min) – the time after which the tracer concentration has reached its stationary value and the dwell time (t_{dwell} = 2.3 min) – time span between t_{trans} and t_{delay} – have been introduced in the literature [10]. In case of radical formation driven purely by vicinity of light, as shown in the previous section, the reaction occurs mainly in the reactor volume and the reaction mixture flowing through the bypass remains non-irradiated introducing deviations from theoretical behaviour in the observed reaction rate. Still, in the future applications, this effect can be minimized by increasing the reactor volume what was not appropriate for presented herein proof-of-principle studies.

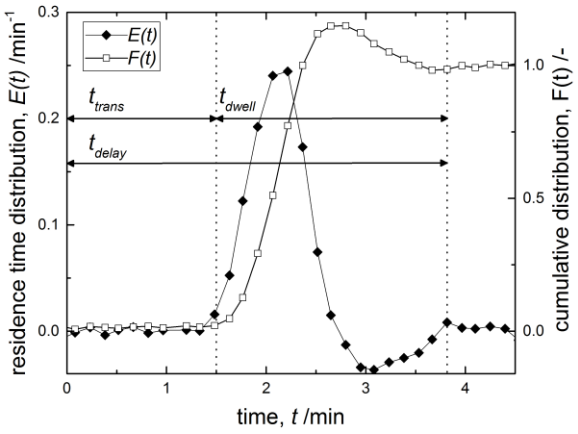

Fig. 3: Cumulative distribution F(t) and residence time distribution function E(t) measured with the NMR instrument in a step tracer experiment, the negative E(t) appears due to re-dilution in the bypass system. The respective times t_{trans}, t_{delay}, t_{dwell} are indicated in the plot.

2.5. Automated data processing of 1H spectra

After acquisition of the FID, the raw data points (32 k) were zero-filled to 64 k and Fourier transformed in the MATLAB environment. Spectra were corrected by automated algorithms for baseline and phase adjustments. In order to estimate spectral background, an iterative method fitting a low order polynomial by minimising a non-quadratic cost function was implemented [25]. Optimal zero-order and first-order phase corrections were determined based on entropy minimization [26]. Spectra were aligned to the dominant solvent signals at 1.96, 8.02, and 2.54 ppm for ACN, DMF, and DMSO respectively. Additionally, an exponential line broadening function of 0.1 Hz was applied. A representative proton spectrum before and after processing is shown in the supplementary information.

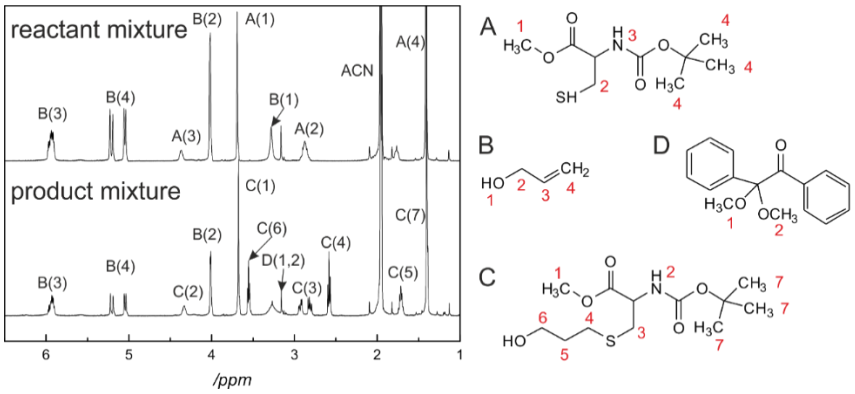

Fig. 4. Spectral assignment of 500 MHz NMR spectra for the reactant mixture and the product mixture after 1 h reaction time. The diastereotopic protons in position 3 of C were summarized to C(3) as well as the vinylic protons in B(4) – A: N-boc cysteine methyl ester, B: allyl alcohol, C: thioether product, D: 2-phenylacetophenone (DMPA).

2.6. Determination of signal areas using indirect hard modeling (IHM) and direct integration

In order to analyse the online spectra in respect to their signal areas for each component spectral assignment has to be conducted. Fig. 4 presents the spectral assignment for the reactant mixture as well as for the product mixture after 1 h of reaction time. IHM was applied to quantitatively resolve overlapping signals A (1) and C (1) of the reactants in

reaction mixture spectra by using the software PEAXACT (SPACT GmbH, Aachen, Germany). The overall framework of IHM consists of the succeeding steps. Firstly, a nonlinear spectral model is generated, which is subsequent fitted to the mixture spectra. Followed conventionally, by a linear calibration model for the prediction of concentrations or ratios from the component fitting results [15]. Regarding the spectral model, pure component models have to be generated by fitting peak functions (Pseudo-Voigt functions) to measured spectra. Based on the spectral assignment, pure component models for N-Boc cysteine methyl ester, allyl alcohol and the thioether product were generated. Therefore, spectra of the final reaction mixture as well as of the initial reaction mixture as shown in Fig. 4 were used. Plots for each pure component model are shown in the supplementary information indicating each single peak function of the models. Additionally, the ranges of interest in the spectra for each component were defined. Solvent signals, OH- and NH- groups of the reactants and the signals of the photoreactant were excluded. Each pure component model consisted of 4–14 peak functions with each peak defined by four parameters of the pseudo-Voigt function, the peak maximum α, the width γ, the position δ and the Gaussian-Lorentzian-ratio β (Eq. (1)**):**

$$V = \alpha\left[\beta \exp\left(-4 \ln 2 \frac{(x-\delta)^2}{\gamma^2}\right) + (1-\beta)\frac{\gamma^2}{(x-\delta)^2+\gamma^2}\right] \quad \textit{Eq. 1}$$

In Table 1, the data range in ppm for each hard model and the respective chemical group are listed. The ranges vary for the respective solvent due to varying overlaps of the solvent signal with the thioether product signal. After generating the component models, a spectral model for mixtures (mixture model) was established. The mixture model consists of a weighted sum of the three reactants (N-Boc cysteine methyl ester, allyl alcohol and the thioether product) component models superimposed with a linear baseline function. IHM builds each mixture spectrum by fitting weighting factors of each component models to a least squares residual between the mixture model and the measured mixture spectrum (component fitting). During component fitting process, nonlinear effects such as peak line broadening or spectral shifts are taken into account by allowing the variation of peak parameters (Eq. (1)) within a constrained range, while the relative peak area in each component model is kept constant. The parameter constraints for the peak position (individual for each peak) and the component shift (shift of all peaks of a component model) showed the most influence on the fitting results. Hereby, the relative boundaries for the peak position were set to 0.05 ppm, the boundaries of component shifts were set to 0.01 ppm while peak maximum and half width was constrained to an relative outer limit of ±100%. As fitting mode ‘‘very high interaction” was used, which allows the adjustment of all model parameters simultaneously. The result of a component fit for a mixture spectrum is shown in Fig. 5, highlighting the signals A(1), C(1) and C(6). For the direct integration method, the processed NMR spectra were numerically integrated in the intervals provided in Table 2 with MATLAB. The acquired signal areas were converted to concentrations and ratios as indicated in Section 2.7.

Tab. 1: Defined spectral ranges of component models for experiments with ACN as solvent

hard model	group no.	chem. group	data range /ppm	no. of peaks
N-Boc cysteine methyl ester	A(1)	$–OCH_3$	3.5–3.85	8
llyl alcohol	B(4)	$=CH_2$	4.85–5.5	4
Product (ACN)	C(1), C(4), C(6)	$–OCH_3$, $–CH_2$, $–CH_2$	3.5–3.85; 2.5–2.7	14
Product (DMSO, DMF)	C(1), C(4), C(5)	$–OCH_3$, $–CH_2$, $–CH_2$	3.5–3.85; 1.65–2.0	14

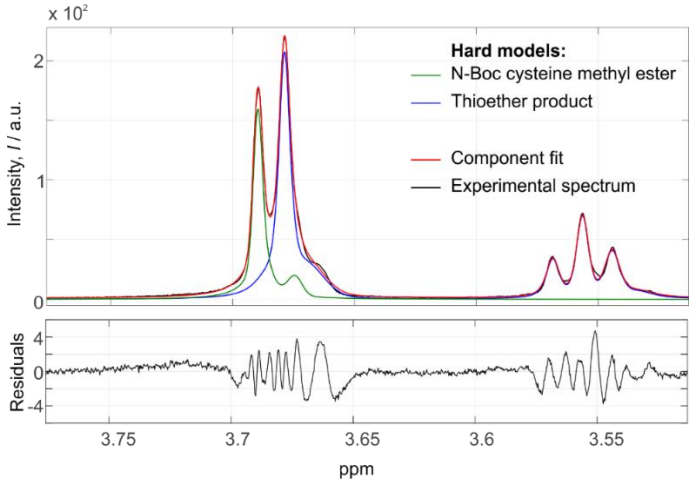

Fig. 5: Representative result for the component fitting of an online NMR spectrum (^1H, 500 MHz) after 15 min reaction time during thiol-ene coupling between N-boc cysteine methyl ester and allyl alcohol.

Tab. 2: integration ranges for processed ^1H spectra of thiol-ene coupling

reactant	group no.	chem. group	integration range /ppm
Allyl alcohol	B(4)	$=CH_2$	4.95–5.33
Thioether product	C(4)	$–CH_2$	2.5–2.65
Thioether product	C(5)	$–CH_2$	1.65–1.94

2.7. Determination of ratios and concentrations

One of the advantages of NMR spectroscopy as an analytical tool is, that the signal intensity in the spectrum is directly proportional to the number of nuclei responsible for this particular resonance. As a result of this in most cases no need for a linear calibration model is needed, if the signal area and the respective molecular structure which causes the signal are known. Thus, a different approach for IHM was chosen with the benefit of reducing the calibration effort. Instead of a linear calibration model, the concentrations were directly calculated out of the peak areas of the fitted component models. One of the easiest methods for NMR is the relative quantification method. Hereby, without calibration, the molar ratio x_i can be calculated on the basis of peak area rations by employing the following expression:

$$x_i = \frac{A_i}{\nu_i} \Big/ \sum_{i=0}^{n} \frac{A_i}{\nu_i}$$

Eq. 2

where ν_i is the number of nuclei, A_i is the absolute Integral. For the absolute quantification method, the use of a concentration conversion factor ξ is needed in order to convert signal areas to molar concentration c_i. ξ was determined via 1-point calibration obtained from the starting concentration of each experiment using Eq. (3):

$$\xi = c_i \cdot \frac{\nu_i}{A_i} \leftrightarrow c_i = \xi \cdot \frac{A_i}{\nu_i} \qquad \textit{Eq. 3}$$

For IHM, the area of each component model was derived from the peak parameters of the Pseudo-Voigt functions with the following equation (cf. Eq. (1)):

$$A = \alpha\,\gamma\left[\beta \cdot \sqrt{\pi/\ln 2} + (1-\beta)\cdot\pi\right] \qquad \textit{Eq. 4}$$

3. Results and discussion

This publication presents an online NMR setup coupled with automated algorithms for spectral processing as well as for the quantification method. To monitor the reaction propagation, IHM was chosen as the favourable evaluation method since it allows resolving the pure peak area of each analyte from the overlapped spectrum measured in the reacting mixture. Through the application of IHM the signal area for each reactant can be deconvoluted from the spectrum and thus converted to the respective molar ratio (calibration-free) or concentration (1-point calibration). However, considering that 1-point calibration method based on a concentration conversion factor (Eq. (3)) is non-specific regarding the analyte, the calibration was carried out with the non-overlapping peaks from the starting mixture of the experiments. Linear multivariate methods like PLS-R have not been considered in this application, since these methods require a calibration set throughout the entire concentration range.

The non-overlapping signals, which were suitable for direct integration, were used herein for comparison purposes of both methods.

3.1. Reaction monitoring

Fig. 6 shows concentration time profiles based on the reaction performed in DMSO. The S-H bond is consumed due to the coupling between N-boc cysteine methyl ester and allyl alcohol, whereas their decrease is directly related to the amount of newly produced bond. The presented plot was obtained from single scans proving that applied spectral modeling in combination with highly linear response of the spectrometer provides high quality results allowing for determination of reaction performance. Data points representing an offset from the exponential trend are related to the additional sampling of the reaction mixture performed using valve V1, which induced flow fluctuations in the by-pass system. Moreover, reaction performance was monitored utilizing ACN and DMF as solvent. Fig. 7 provides a comparison of the individual solvents, depicting the respective molar ratio of product over time. These results indicate faster transformation of reactants into thioether product in the initial phase when ACN is used. For DMSO and DMF the rate of product formation in between 5 and 10 min represents a linear increase of 0.013 per min (0.037 mol mL^{-1} min^{-1}), while the reaction performed in ACN shows a slope of 0.02 per min (0.051 mol mL^{-1} min^{-1}). The varying initial reaction rates cause varying turnovers for DMSO, DMF, and ACN after 20 min (72, 71, and 79%). Nonetheless, for all solvents the limiting reactant (N-boc cysteine methyl ester) was

completely consumed after approximately one hour and thus quantitative conversion was achieved. Variations in the final molar ratio of product for the different solvents reach up to 0.05 due to minor deviations in the initial concentration of reactants. The described changes in the initial phase of product formation might be subjected to the properties of reaction mixture related to the environment in which transformation occurs. Changes in solvent properties like polarity, viscosity lead to changes in reactant interactions hence reaction rates. Taking into account the solvent polarity index the lowest value is for ACN and the increase for DMF and DMSO being 5.8, 6.4, 7.2, respectively [27]. The same dependence is observed for their density being 0.786, 0.944, and 1.100 g mL^{-1} for ACN, DMF, DMSO respectively. Accordingly, it can be suspected that mixing intensity will vary depending on the solvent and will have the most significant influence in the initial phase of reaction when radicals are produced. The influence of solvent polarity cannot be excluded. However, for the solvents applied throughout this study there is no direct indication of a solvent. The typical mechanism of the intended radical initiated thiolene click chemistry involves two steps: propagation and chain transfer. C–S bond formation is initiated by thiyl radicals created by charge transfer from primarily formed photoinitator radicals. Produced thiyl radicals react with alkenes forming intermediate carbon centered-thioether radical (propagation). The intermediate radical is able to abstract a hydrogen atom, forming the thioether product along with a new thiyl radical (chain transfer), which can then initiate another propagation step [28]. A detailed scheme of the reaction mechanism is illustrated in the supplementary information. By terminating the irradiation after 15 min reaction propagation by chain transfer step and recombination of light induced radicals was investigated. The exponential results obtained for 15 min irradiation is characterized by the same slope as in case of 60 min irradiation experiments for the same operating conditions as summarized in Fig. 7. Consistency between the results acquired for the first 18 min indicate high reproducibility of the studied chemical system. Investigations of the reaction propagation after the light cut off indicate no significant changes after merely three minutes. The timescale required to detect reaction termination is affected by two mechanisms (i) time required for radical recombination (ii) the system response being delayed due to the remaining residence time. As described in Section 2.4 the delay time to the system is assessed to be 3.8 min nicely coinciding with the detected reaction end-point delay. Hence, radicals formed by the photoinitiation recombine directly (or at least within the temporal resolution of 3 min) when the driving force (photons) required for their production is withdrawn. This indicates a negligible contribution of the chain transfer reaction. Line broadening effects, which usually appear when paramagnetic radicals are investigated [29], were not observed, since radicals recombine before they enter the active region of the NMR. The observed product concentration decreases slightly between 21 min and 30 min appears due to the final rinsing of dead volume in the by-pass system and merely reflects fluid dynamic equilibration.

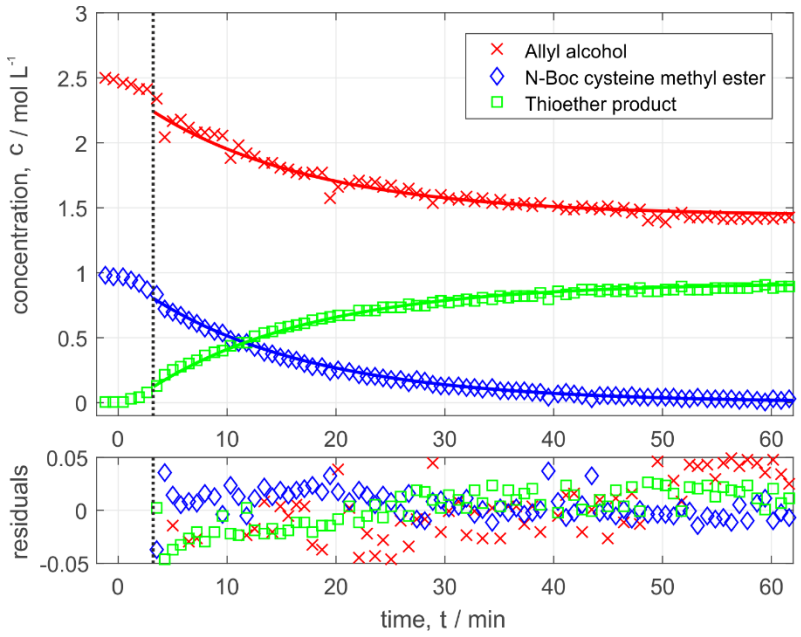

Fig. 6: Comparison of time courses for the photoreaction using DMSO as solvent calculated with IHM (symbols) and fitting results to first order reaction kinetics (lines), residuals of NMR results compared to mass balance of kinetic model. Deviations in Allyl alcohol concentrations were mainly due to withdrawing samples from the reactor.

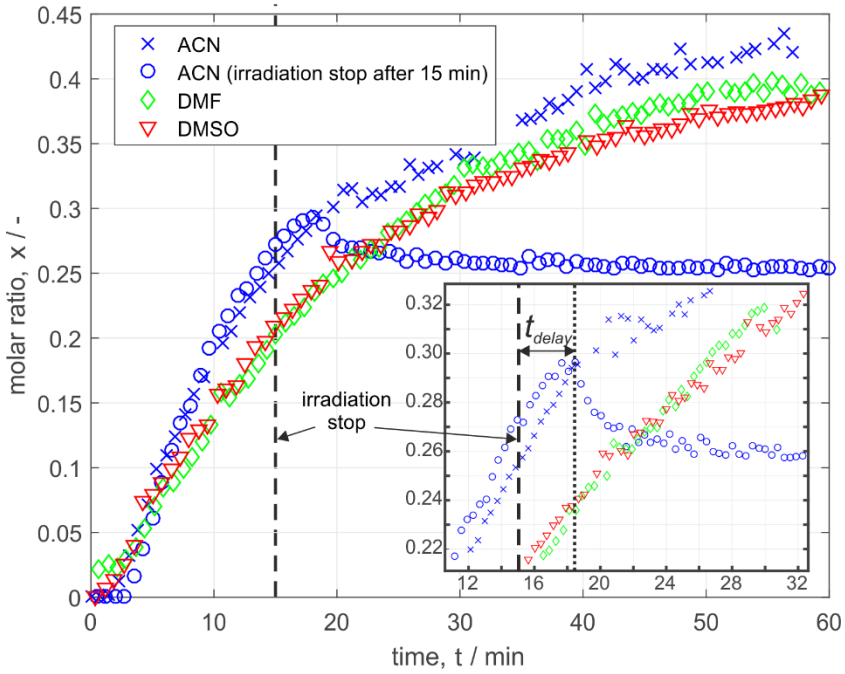

Fig. 7: Time courses of the molar ratio for the thioether product during photoreaction

3.2. Material balance and kinetics

According to the above described reaction mechanism reaction kinetics can be differentiated in respect to ratio of propagation and chain transfer rate. Thiols with less abstractable hydrogen atoms, such as alkyl thiols (i.e. N-boc cysteine methyl ester), will tend to have reduced chain transfer rates. This results in rate-limiting chain transfer reactions and thus pseudo-first order reaction kinetics based on thiol concentration [18,28]. By plotting the logarithm of the experimentally obtained N-boc cysteine methyl ester concentrations over time, a resulting linear behaviour justifies this approximation to first order kinetics. In order to

validate the quantitative NMR results of IHM a material balance according to Eq. (5) was generated, assuming an irreversible first-order reaction.

$$\frac{\mathrm{d}c_\mathrm{A}}{\mathrm{d}t} = \frac{\mathrm{d}c_\mathrm{B}}{\mathrm{d}t} = -\frac{\mathrm{d}c_\mathrm{C}}{\mathrm{d}t} = -r = kc_\mathrm{A} \qquad \textit{Eq. 5}$$

On the basis of this simple model, the time courses of reactants can be described and fitted to the experimental data. For identification of the model parameters c_A(t = 0), c_B(t = 0), c_C(t = 0), as well as k a simplex search method was used to minimize a objective function, which is based on least squares. By reason of response time in the tubing system the first three minutes of irradiation were neglected during the fitting process. The results of the mass balance of the adapted kinetic model are plotted in Fig. 6. No major trends regarding the residuals were observed, indicating a satisfying quality of the fit. The kinetic constant k (h^{-1}) was estimated to 3.96, 3.92, and 3.94 for experiments using ACN, DMF and DMSO as solvent, respectively. Moreover, the impact of residence time distribution when determining reaction kinetics can be further reduced by modifying the experimental set-up and by introducing E(t) into the mass balance of the kinetic model.

3.3. Uncertainty evaluation

For this study, no reference analytics was available in the interest of validation of NMR results in ‘‘traditional” manner. In order to obtain a first estimation of the uncertainty of the presented method, standard deviations of the reactant concentration were calculated for the period of time when concentrations remained constant. An experiment, in which irradiation was terminated after 15 min was well suited since concentrations did not change from absolute standard deviations of 0.011, 0.004 and 0.005 mol L^{-1} were obtained for allyl alcohol, N-boc cysteine methyl ester, and the thioether product, respectively. However, a rigorous in-depth analysis of uncertainty of peak parameters, which were calculated during component fitting, would be beneficial for precise error propagation calculations for peak areas and thus for concentrations. In Fig. 8 the NMR results for IHM and direct integration are compared in a parity plot. While the two methods show a strong coincidence with unity slope (Fig. 8–I) for the allyl concentrations, the obtained thioether product concentrations show a constant offset between direct integration and IHM (Fig. 8–II). For direct integration the signal C(4) was evaluated, for IHM the signals C(1), C(4) and C(6) were taken into account in the respective pure component model. As expected, those signal areas of the same compound for both methods show a strongly linear dependency of the resulting concentration. However, regarding the product concentration (Fig. 8, I) a minor constant offset can be observed. Since the sign of the observed deviation in the parity plot is positive, it is assumed to be an influence of an insufficient covering of the signal area for that signal C(4) using the direct integration method.

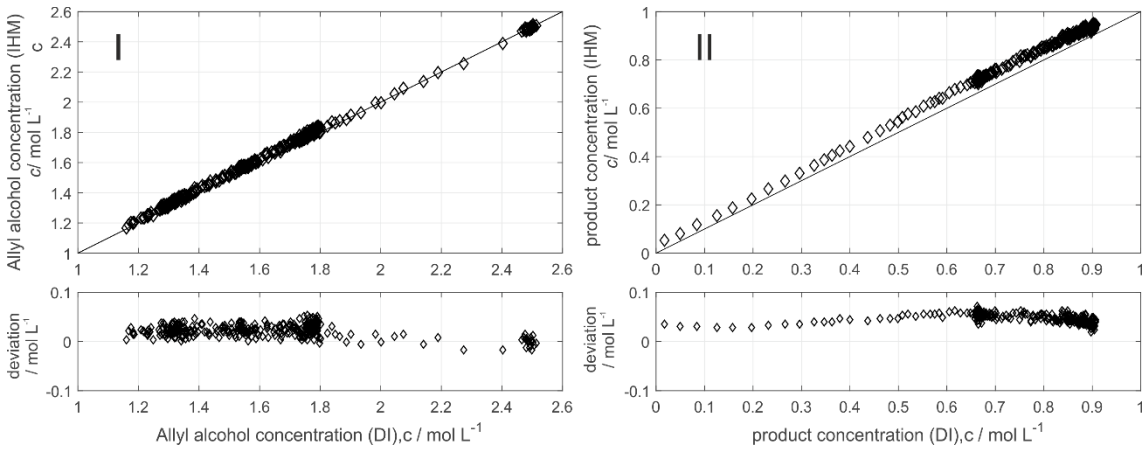

Fig. 8: Direct comparison of reactant concentrations calculated via direct integration (DI) and indirect hard modeling (IHM) for allyl alcohol (*I*) *and the corresponding thioether product* (*II*) *in a parity plot along with deviations c(IHM) – c(DI).*

4. Conclusion

The implemented flow cell NMR set-up for online monitoring in combination with IHM allows quantitative online tracing of reactants during thiol-ene coupling using ‘‘click chemistry”. The presented method demonstrates a simple procedure used for evaluation of complex NMR spectra which cannot be evaluated via direct integration. The evaluation method is based on a spectral modeling approach which requires solely pure component spectra and the spectral assignment. This method benefits in comparison to classical PLS-R from quantitative insight in signal areas of pure components in overlapping signals and thus yields a significantly reduced calibration effort and, therefore, exhibits short set-up times. This was shown for adjusting the IHM models for a couple of different solvents in which the reaction was conducted. The sensitivity of the presented approach allows to identify minor changes in the reaction kinetics when different solvents are applied. Moreover, depicted negligible deviations in concentration during several experiments indicate high repeatability between the measurements. A direct comparison of the two methods, IHM and direct integration, reveal their analogous performance. IHM considers additional peaks, which cannot be resolved utilizing direct integration, providing more flexibility to characterize chemical systems and a more robust analysis. The ultimate advantage of IHM can be anticipated to lie in a quantitative analysis of non-baseline-resolved spectra as they are typical for even more complex reaction mixtures or data obtained on lower field NMR instruments. Thus, the work presented here could eventually pave the road towards a reliable evaluation with low field NMR instruments using permanent magnets in an industrial environment. The extracted data would be beneficial for on-site kinetic studies, screening of novel reactions and optimization of reaction conditions run in small batches.

Acknowledgement

Authors are indebted to Klas Meyer and Nicolai Zientek for help in performing preceding experiments and Andrea Paul for providing the light source. The work of A. Michalik-Onichimowska was financially supported by the Excellence Initiative of the German Research Foundation (DFG). M. Maiwald and S. Kern gratefully acknowledge support from the European Union’s Horizon 2020 research and innovation programme under grant agreement N° 636942.

Appendix A. Supplementary material

Supplementary data associated with this article can be found, in the online version, at http://dx.doi.org/10.1016/j.jmr.2017.02.018.

References

[1] A. Adamo, R.L. Beingessner, M. Behnam, J. Chen, T.F. Jamison, K.F. Jensen, J.-C.M.Monbaliu, A.S. Myerson, E.M. Revalor, D.R. Snead, T. Stelzer, N. Weeranoppanant, S.Y. Wong, P. Zhang, On-demand continuous-flow production of pharmaceuticals in a compact, reconfigurable system, Science 352 (2016) 61–67.

[2] A. Gałuszka, Z. Migaszewski, J. Namies´nik, The 12 principles of green analytical chemistry and the SIGNIFICANCE mnemonic of green analytical practices, TrAC Trends Anal. Chem. 50 (2013) 78–84.

[3] J. Mitchell, L.F. Gladden, T.C. Chandrasekera, E.J. Fordham, Low-field permanent magnets for industrial process and quality control, Prog. Nucl. Magnet. Reson. Spectrosc. 76 (2014) 1–60.

[4] K. Meyer, S. Kern, N. Zientek, G. Guthausen, M. Maiwald, Process control with compact NMR, TrAC Trends Anal. Chem. 83 (2016) 39–52, http://dx.doi.org/ 10.1016/j.trac.2016.03.016.

[5] F. Dalitz, M. Cudaj, M. Maiwald, G. Guthausen, Process and reaction monitoring by low-field NMR spectroscopy, Prog. Nucl. Magnet. Reson. Spectrosc. 60 (2012) 52–70.

[6] S.K. Bharti, R. Roy, Quantitative 1H NMR spectroscopy, TrAC Trends Anal. Chem. 35 (2012) 5–26.

[7] M.A. Bernstein, S. Sy´ kora, C. Peng, A. Barba, C. Cobas, Optimization and automation of quantitative NMR data extraction, Anal. Chem. 85 (2013) 5778– 5786.

[8] M. Gal, M. Mishkovsky, L. Frydman, Real-time monitoring of chemical transformations by ultrafast 2D NMR spectroscopy, J. Am. Chem. Soc. 128 (2006) 951–956.

[9] B. Gouilleux, B. Charrier, E. Danieli, J.-N. Dumez, S. Akoka, F.-X. Felpin, M. Rodriguez-Zubiri, P. Giraudeau, Real-time reaction monitoring by ultrafast 2D NMR on a benchtop spectrometer, Analyst 140 (2015) 7854–7858.

[10] M. Maiwald, H.H. Fischer, Y.-K. Kim, K. Albert, H. Hasse, Quantitative highresolution on-line NMR spectroscopy in reaction and process monitoring, J. Magnet. Reson. 166 (2004) 135–146.

[11] J.C. Edwards, P.J. Giammatteo, Process NMR spectroscopy: technology and online applications, in: K.A. Bakeev (Ed.), Process Analytical Technology, John Wiley & Sons, Ltd, 2010, pp. 303–335.

[12] T.M. Alam, M.K. Alam, Chemometric Analysis of NMR Spectroscopy Data: A Review, Annual Reports on NMR Spectroscopy, Academic Press, 2004, pp. 41– 80.

[13] T.M. Alam, M.K. Alam, S.K. McIntyre, D.E. Volk, M. Neerathilingam, B.A. Luxon, Investigation of chemometric instrumental transfer methods for highresolution NMR, Anal. Chem. 81 (2009) 4433–4443.

[14] E. Kriesten, D. Mayer, F. Alsmeyer, C.B. Minnich, L. Greiner, W. Marquardt, Identification of unknown pure component spectra by indirect hard modeling, Chemometr. Intell. Lab. Syst. 93 (2008) 108–119.

[15] E. Kriesten, F. Alsmeyer, A. BardoW, W. Marquardt, Fully automated indirect hard modeling of mixture spectra, Chemometr. Intell. Lab. Syst. 91 (2008) 181–193.

[16] N. Zientek, C. Laurain, K. Meyer, A. Paul, D. Engel, G. Guthausen, M. Kraume, M. Maiwald, Automated data evaluation and modelling of simultaneous 19F–1H medium-resolution NMR spectra for online reaction monitoring, Magnet. Reson. Chem. 54 (2016) 513–520.

[17] N. Zientek, C. Laurain, K. Meyer, M. Kraume, G. Guthausen, M. Maiwald, Simultaneous 19F–1H medium resolution NMR spectroscopy for online reaction monitoring, J. Magnet. Reson. 249 (2014) 53–62.

[18] C.E. Hoyle, C.N. Bowman, Thiol-ene click chemistry, Angew. Chem.-Int. Ed. 49 (2010) 1540–1573.

[19] C. Ligeour, L. Dupin, A. Marra, G. Vergoten, A. Meyer, A. Dondoni, E. Souteyrand, J.J. Vasseur, Y. Chevolot, F. Morvan, Synthesis of galactoclusters by metal-free thiol ‘‘Click Chemistry” and their binding affinities for pseudomonas aeruginosa Lectin LecA, Eur. J. Org. Chem. (2014) 7621–7630, http://dx.doi. org/10.1002/ejoc.201402902.

[20] A. Dondoni, A. Marra, Recent applications of thiol-ene coupling as a click process for glycoconjugation, Chem. Soc. Rev. 41 (2012) 573–586.

[21] M.A. Cole, C.N. Bowman, Evaluation of thiol-ene click chemistry in functionalized polysiloxanes, J. Polym. Sci. Pol. Chem. 51 (2013) 1749–1757.

[22] E.L. Tyson, Z.L. Niemeyer, T.P. Yoon, Redox mediators in visible light photocatalysis: photocatalytic radical thiol-ene additions, J. Org. Chem. 79 (2014) 1427–1436.

[23] F. Dalitz, M. Maiwald, G. Guthausen, Considerations on the design of flow cells in by-pass systems for process analytical applications and its influence on the flow profile using NMR and CFD, Chem. Eng. Sci. 75 (2012) 318–326.

[24] A.D. Martin, Interpretation of residence time distribution data, Chem. Eng. Sci. 55 (2000) 5907–5917.

[25] V. Mazet, C. Carteret, D. Brie, J. Idier, B. Humbert, Background removal from spectra by designing and minimising a non-quadratic cost function, Chemometr. Intell. Lab. Syst. 76 (2005) 121–133.

[26] L. Chen, Z.Q. Weng, L.Y. Goh, M. Garland, An efficient algorithm for automatic phase correction of NMR spectra based on entropy minimization, J. Magnet. Reson. 158 (2002) 164–168.

[27] L.R. Snyder, Classification off the solvent properties of common liquids, J. Chromatogr. Sci. 16 (1978) 223–234.

[28] B.H. Northrop, R.N. Coffey, Thiol-ene click chemistry: computational and kinetic analysis of the influence of alkene functionality, J. Am. Chem. Soc. 134 (2012) 13804–13817.

[29] C. Feldmeier, H. Bartling, K. Magerl, R.M. Gschwind, LED-illuminated NMR studies of flavin-catalyzed photooxidations reveal solvent control of the electron-transfer mechanism, Angew. Chem. Int. Ed. 54 (2015) 1347–1351.

3.3. Coupling of acoustically levitated droplet to IMS

Laser ionization ion mobility spectrometric interrogation of acoustically levitated droplets

Aleksandra Michalik-Onichimowska[1,2,3], Toralf Beitz[3], Ulrich Panne[1,2,4], Hans-Gerd Löhmannsröben[3], Jens Riedel[1*]

[1] *School of Analytical Sciences Adlershof, Humboldt-Universität zu Berlin, Zum Großen Windkanal 6, 12489 Berlin, Germany*

[2] *Bundesanstalt für Materialforschung und -prüfung (BAM), Richard-Willstätter-Straße 11, Berlin*

[3] *Physical Chemistry, University of Potsdam, Karl-Liebknecht-Str. 24-25, 14476 Potsdam, Germany*

[4] *Institut für Chemie, Humboldt-Universität zu Berlin, Brook-Taylor-Str. 2, 12489 Berlin, Germany*

**Corresponding Author: Jens.Riedel@bam.de*

Keywords: Ambient Pressure Laser Ionization, Ion Mobility Spectrometry, Acoustic levitation, Ion Optics

Abstract

Acoustically levitated droplets have been suggested as compartmentalized, yet wall-less microreactors for high throughput reaction optimization purposes. The absence of walls is envisioned to simplify up-scaling of the optimized reaction conditions found in the microliter volumes. A consequent pursuance of high-throughput chemistry calls for a fast, robust and sensitive analysis suited for online interrogation. For reaction optimization, targeted analysis with relatively low sensitivity suffices, while a fast, robust, and automated sampling is paramount. To follow this approach, in this contribution a direct coupling of levitated droplets to a homebuilt ion mobility spectrometer (IMS) is presented. The sampling, transfer to the gas phase, as well as the ionization are all performed by a single exposure of the sampling volume to the resonant output of a mid-IR laser. Once formed, the nascent spatially and temporally evolving analyte ion cloud needs to be guided out of the acoustically confined trap into the inlet of the ion mobility spectrometer. Since the IMS is operated at ambient pressure, no fluid dynamic along a pressure gradient can be employed. Instead, the transfer is achieved by the electrostatic potential gradient inside a dual ring electrode ion optics, guiding the analyte ion cloud into the first stage of the IMS linear drift tube accelerator. The design of the appropriate atmospheric pressure ion optics is based on the original vacuum ion optics design of Wiley and McLaren. The obtained experimental results nicely coincide with ion trajectory calculations based on a collisional model.

1. Introduction

Acoustical levitation became of interest due to its intrinsic properties in sample handling. Not posing any physical constraints on the levitated sample, it is highly adoptable to microfluidic chemical reactors allowing for compartmentalized, yet wall-less sample handling. The absence of walls minimizes contamination and cross-talk caused by possible ad-/desorption processes occurring between the sample volume and surface of the container walls. Stable levitation conditions in an acoustic field enable handling of a wide range of sample volumes, irrespective of its physical state, and in any carrier-gas including ambient conditions. The minute sample volumes have made levitation of droplets mature to a powerful tool in bioanalytical applications [1]. Levitation allows compartmentalization of liquids, while, compared to conventional microfluidics, no contact to any other liquid or solid interfaces is necessary, the droplet is confined by an acoustic field alone. The inside of the droplet is in a zone of acoustic silence where diffusion predominates any occurring mixing effects. This absence of mixing allows phase separation between two solvents of different polarities allowing for extracting analytes of importance in one of the phases inside the single droplet. If mixing is favored, a modulation of the carrier frequency can effectively perturb the droplet. In summary, all fundamental steps of laboratory routine analysis as sample introduction, mixing, separation preconcentration and sample removal can be performed on levitated droplets. Hence the intrinsic properties of the acoustically levitated droplet make it a suitable microreactor.[2-4]

Therefore, lately some attention has been put onto on-line monitoring of chemical reactions performed within levitated droplets.[5] Several interrogation schemes have been proposed for contactless interrogation of the droplets' chemical composition. The majority of the available publications focus on spectroscopic detection techniques showing successful monitoring of reactions performed within the levitated droplet volume by RAMAN, IR, X-Ray where interrogation is remotely performed inside intact droplets.[6-8] However, until now only a limited number of publications report on the interrogation of the volume composition of levitated droplet *via* gas phase detection techniques, which require effective sample desolvation such as mass spectrometry (MS). The successful approaches include either contactless sampling of a single levitated droplet by IR-laser light and detection of the generated analyte ion plume or at-line detection of reaction performed within levitated droplet were the levitated droplet is collected on a metal mesh and ionized using DART source.[1, 9] Though, in both cases, the sample/reaction mixture is handled at atmospheric pressure and the ion plume is directed towards the MS entrance along a decreasing pressure gradient between the acoustic trap vicinity and the MS orifice. Another approach to direct the generated ion plume presented by Westphall[10] utilizes a ring electrode between the droplet and the MS orifice acting as an ion gating electrode operated in pulsed mode. Here, the ion plume can be directly modulated regarding its spatial and temporal propagation. Still, a robust approach to contactless on-line monitoring of reaction performed within levitated droplet is in the development phase.

In the last 15 years ion mobility spectrometry (IMS), operated at atmospheric pressure, has been extensively studied as an alternative route for gas phase detection.[11] IMS is widely used for on-site detection of warfare agents, explosives and industrial applications in pharmaceutical and food industry; IMS in combination with MS has been attested a wide

applicability for interrogation of complex matrices in proteomics and metabolomics.[12-15] There is a number of possible IMS separation principles, however the most straightforward utilizes a linear drift tube.[16, 17] Here, the ions are guided along an electric field applied in the opposite direction of a buffer gas stream. The number of collisions the analyte ions experience with the buffer gas, defines the separation power and it is directly correlated to the size, shape and 3D-structure of the molecule. The collisional cross section as a molecule-specific parameter allows to not only differentiate between possible isomers but even isobars of very similar structure. A number of research groups develop IMS systems ever improving its performance and applicability.[18] Current advances are directed towards the implementation of new ionization sources and coupling to HPLC, MS reaching 2-dimensional separation improving separation power.[19, 20]

The possibility to model motion of ions in the neutral gas at atmospheric pressure, under the influence of electrostatic field, became a powerful tool in designing new instruments including couplings and introduction of new ionization sources. Finite element methods allow to numerically predict ion trajectories inside electrostatic lenses integrating the pressure-temperature-velocity forces of dynamic gas flow with the forces imposed by the electrostatic field. The resulting, reliable prediction of ions in force fields at ambient collision conditions by modelling has greatly accelerated instrumental development. These complex ion motions at atmospheric pressure are also applied when converting empirical IMS results as the drift time into molecular specific properties such as the collisional cross section.

Herein we present a novel sample introduction/ionization system utilizing acoustically levitated droplet coupled to drift tube IMS. The ion plume ejected out of the surface of a levitated droplet by a nanosecond infrared (ns IR) laser pulse is transferred into the IMS internal electric field regime *via* an ion optics composed of two electrostatic lenses. The applied electrostatic fields invoke the ion propagation and spatially focus the ions towards the customized inlet of the drift tube IMS. The experimental results are subsequently compared to predictions obtained using the SIMION ion trajectory modeling suite.

2. Methods

The acoustic trap for droplet levitation is composed of a sonotrode equipped with a radiating plate and an opposing spherical reflector. When the sonotrode and reflector are placed at a resonant distance 5/2 λ and the 41 kHz sine function output of a power driver is applied to the Langevine type piezo transducer stack (MTH, Henstedt, Ulzburg, Germany), a standing wave is formed between the sonotrode and reflector. The generated acoustic field provides confinement in vertical direction compensating gravity force and, hence, allowing for droplet levitation. For all experiments in this work droplets of 5 µL volume are levitated in the central pressure antinode.

The used drift tube IMS is a modified version of the instrument presented in Beitz et al.[21].A schematic representation of the entire setup can be seen in Figure 1. It consists of a short drift tube of length L=80 mm, operated at temperature 180°C. The relatively short length allows for operation at comparably low voltages on the electrodes of the IMS. The drift tube is composed of alternating pairs of a stainless-steel drift ring and a PEEK spacer. Each pair of metal ring and isolator ring is of 5 mm length arranged in a tubular manner. Along the conductive rings the externally applied potential drops along a voltage divider consisting of a

series of resistors and a ground termination. The endcap carries a central Faraday plate detector. Along the drift tube, separation according to collisional cross section is achieved. To facilitate the coupling to the external liquid sample, no counterflowing gas was used. The entrance of the IMS has been customized according to design constrains yielding at maximum ion transmission. The inlet plate electrode was equipped with a protruding cylindrical segment (ID=10 mm, L=10 mm) facilitating operation at proximity to the droplet and IMS inlet. A typical voltage of 5 kV is applied on the inlet resulting in an electric field of E = 625 V/cm inside the drift tube.

The levitated droplet is set up in front of the IMS inlet. To invoke ion transport two electrostatic lenses operated at high potential working as an ion plume repeller and extractor have been implemented. These electrostatic lenses provide a compromise between a comprehensive ion guiding and a minimized geometrical footprint. The latter was found to drastically perturb the emitted acoustic field of the levitator resulting in instable levitation conditions. The overall design of the resulting ion optics resembles the classic vacuum design by Wiley and McLaren.[22] The electrostatic lenses are constructed from metal wire bent on a cylindrical mandrel to form 10 mm diameter loops and aligned parallel to the IMS inlet, forming a circularly symmetric electric field along the entire system. The repeller and extractor electrodes are placed at distance of 5 mm and 10 mm from the cylindrical IMS inlet, respectively. The desorption/ionization out of the droplet was performed with the $\lambda = 2.94$ µm output of an optical parametric oscillator (OPO) (Opotek inc. Carlsbad, CA, USA) with a pulse width of 7 ns, focused by a plano-convex CaF_2 lens (f = 100 mm). As indicated in Figure 1, the laser was aligned to hit the droplet on its outer perimeter to form a desorption plume along the surface normal of the droplet towards the detector.

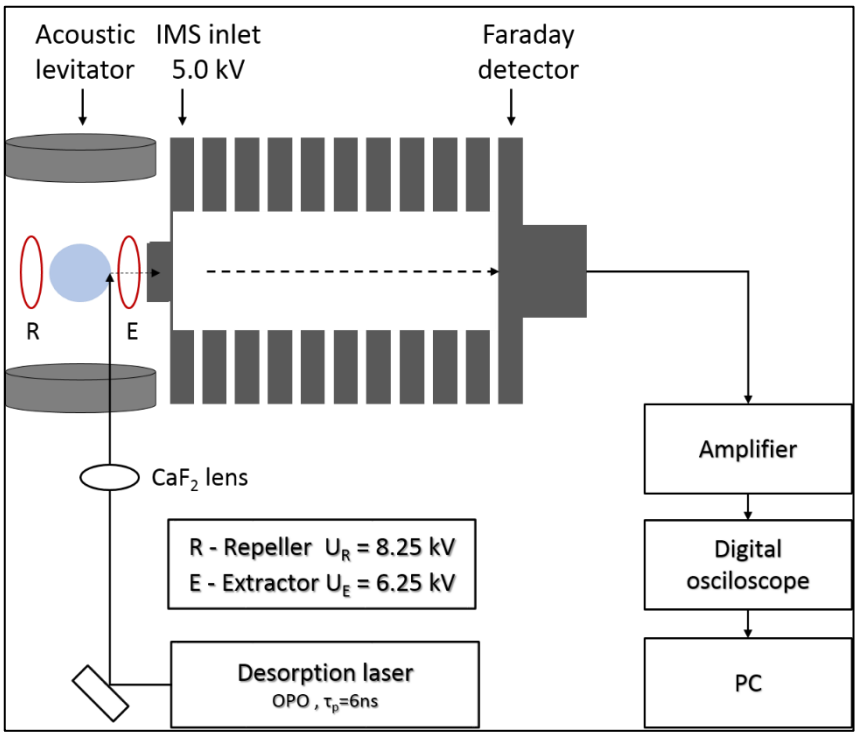

Fig. 1 Schematic of the experimental setup.

In this configuration the propagation vector of the plume is coinciding with the axis of symmetry of the electrostatic fields inside the IMS. The laser pulse energy is adjusted to match the horizontal confinement strength of the acoustic trap. At a pulse energy of 1 mJ per pulse an effective evaporation could be observed, while no ejection of the suspended droplet out of the pressure node occurred.

Optimization of the ion transport was performed on the ion signal of tetra-n-butylammonium bromide (TBAB) as a reference substance. The potentials applied to the extractor and repeller electrodes, $U_{ext.}$ and $U_{rep.}$ were optimized on maximum intensity at minimum peaks widths. The analysis was performed in two subsequent runs. By modifying $U_{rep.}$, in the range 7.25 – 8.5 kV, at constant extractor potential, followed by altering $U_{ext.}$, in the range 5.5 – 7.5 kV at the previously optimized $U_{rep.}$. The upper limit of the high potential applied on repeller was the maximum before discharges between the grounded sonotrode and the ring electrodes occurred. Subsequent reference spectra were acquired for TBAB, atenolol, promazine, and L-arginine dissolved in ACN:H_2O (1:1) solution. No additional sample purification or preparation procedure were applied to reference analytes. Upon manual introduction of the different analyte solutions into the central antinode of the levitator with an Eppendorf pipette, the individual droplets exhibited a slightly different ellipticity changing the exact position of the droplets' equatorial waist. Consequently, for each sample the exact laser spot position had to be slightly modified. All acquired spectra were baseline corrected in Origin (OriginLab Corporation, MA, U.S.A.)

To predesign the applied electrostatic lenses according to the desired ion flow, SIMION (Scientific Instruments Services, Inc.) simulations were conducted. The transport of ions in the atmospheric pressure as well as the collisions between the ions and gas particles occurring in the drift tube and its vicinity were mimicked using the statistical diffusion simulation (SDS) algorithm by Dahl et al. [23]. The simulations were performed at atmospheric pressure of air as collision gas propagating antiparallel to the ejected ion plume. The temperature was set to T = 180°C. The simulation was performed for 500 individual TBAB ions as the standard analyte. The ion cloud origin was set at 6 mm distance from the repeller being the real ion origin of the ion cloud. The results of the simulation are presented in the form of simulated ion mobility spectra to compare the drift times, peak broadening and intensity of simulated and measured spectra.

2.1 Chemicals

All chemicals have been supplied by Sigma-Aldrich (St. Louis, MO, USA).

3. Results

The optimization of the electrostatic lenses and their focusing and ion transmission behaviour is depicted in Figure 2. The Wiley-McLaren type two electrostatic lenses, repeller and extractor, operated at high potential generate electrostatic field between the sampling/ionization region and the IMS inlet region guiding the ions inside the IMS cell. Working potentials applied on the electrostatic lenses are modified according to the potential slopes presented in Figure 2 middle row. The optimization of operating conditions was initiated with the repeller voltage defining the first electrostatic slope the nascent ions experience on their way towards the IMS. The generated ion plume must overcome an electric barrier present in the vicinity of IMS inlet. This is why below voltages of 7.25 kV and 5 kV

applied to the repeller and extractor electrode, respectively, no ions could be observed. For the repeller a natural upper limit for practical use was determined at 8.5 kV by the potential gradient at which discharges between the electrode and the grounded sonotrode occurred. In this first optimization, $U_{ext.}$ was kept constant at 6 kV while $U_{rep.}$ was modified in the range 7.25 – 8.50 kV. In total, three peaks become visible (Fig.2 left bottom). Around 7 ms the reagent ions are detected, a typical phenomenon for IMS. The strongest signal around 12 ms can be assigned to the reference analyte TBAB while the contributions at longer drift times can be attributed to dimer formation. Subsequent stepwise increase of the repeller potential in a 0.25 kV steps resulted in an increase of ion signal coming to a maximum ion signal at a voltage of 8.5 kV. The full width at half maximum (FWHM) of the peaks does not change significantly for the given potential range (Table 1). Due to erratic discharges, 8.5 kV becomes ineffective for any real application purposes, thus 8.25 kV was identified as the best operation voltage for the repeller.

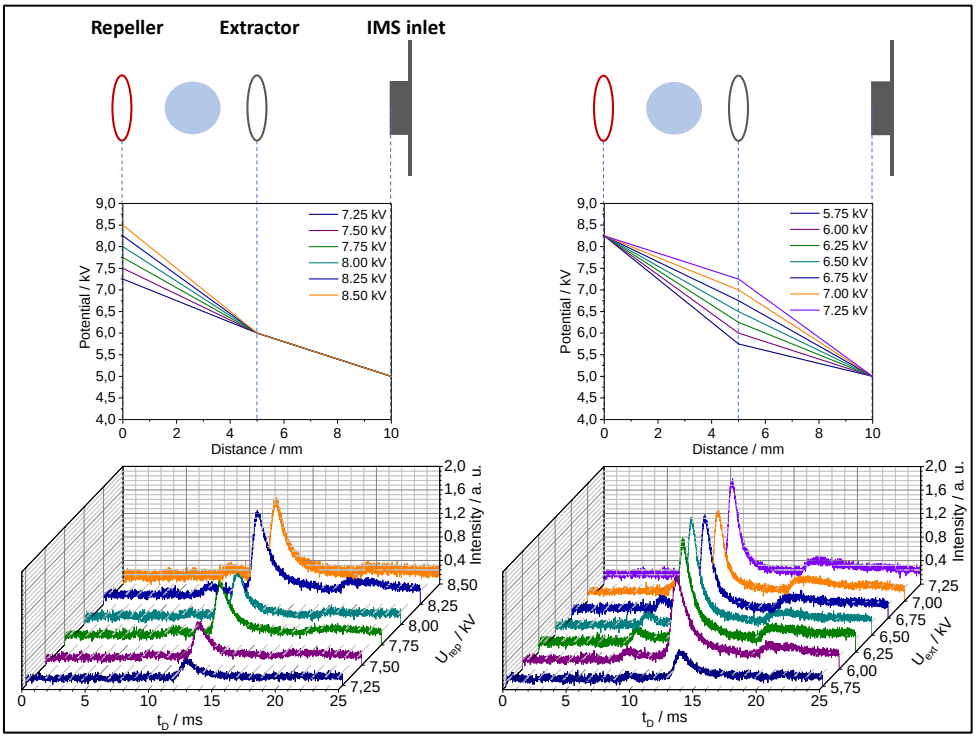

Fig. 2 IMS performance. Top row: schematic; center row: potential gradient along the propagation towards the IMS entrance; bottom row: resulting IMS drift time spectra. Left column: optimization of repeller electrode voltage; right column, optimization of extractor potential.

Previous investigations of laser ablation of liquid droplets by a ns laser pulses observed a pronounced spread of the spray plume in space, time, velocity and progeny droplet size. [24] In IMS all these factors contribute to peak broadening. An ideal ion optics does, therefore, not only show in an efficient guiding but also temporally focusing of the ions. Thus, besides the signal overall intensity also its temporal width should be considered. All of the above can potentially be compensated by the right setting of the dual electrode ion optics. Thus, in a next step, the impact of the ion optics focusing conditions on the ion detection distribution caused by this temporal dissipation was studied. The repeller potential was fixed to 8.25 kV while the extractor potential was altered in the range 5.5 – 7.5 kV. A schematic of the potential gradient is presented in Figure 2 together with the corresponding ion arrival spectra obtained for the

individual extractor potentials. Towards higher extractor potential the intensity of TBAB monomer peak increases while the peak width decreases. For a more quantitative analysis, the analytically relevant figures of merit of the ion signal statistics are summarized in Table 1 and 2.

Tab. 1 Experimental dependence on the voltage applied to the repeller electrode

U_{rep} [kV]	t_D [ms]	FWHM [ms]	I [au]	S/N
7.25	12.6	0.72	0.33	8.9
7.50	12.3	0.97	0.56	15.2
7.75	12.3	1.11	0.87	21.6
8.00	12.1	0.99	0.80	20.2
8.25	12.1	1.01	1.33	25.8
8.50	12.1	1.07	1.28	20.4

Tab. 2 Experimental dependence on the voltage applied to the extractor electrode

U_{ext} [kV]	t_D[ms]	FWHM [ms]	I [au]	S/N
5.75	13.7	0.91	0.45	12.7
6.00	12.1	1.22	1.33	25.8
6.25	11.4	0.98	1.64	31.3
6.50	10.8	0.91	1.88	47.1
6.75	10.6	0.83	1.49	34.9
7.00	10.4	0.78	1.30	33.0
7.25	10.2	0.82	1.57	41.6

From the given number can also be seen that the extractor potential accelerates the ions into the IMS drift tube, leading to a peak drift time decrease from 13.7 ms to 10.2 ms. The signal increase with increasing extractor potential is most pronounced throughout the first 4 applied potentials reaching a plateau for values higher than 6.5 kV (Table 2). The FWHM decreases beyond this potential until reaching a minimum of ~ 0.8 ms at 7.0 kV extractor voltage. The optimal collimating conditions are reached at this specific conditions. As presented in ref.[24], the plume ejection is delayed by the energy transfer within the droplet volume leading to a temporal lag in spray release from the surface of the levitated droplet of up to > 1 ms. This broadening goes along with a spatial distribution and a momentum distribution in both, absolute value and direction. Compared with these findings, an absolute signal peak width of below 0.8 ms attests the simple dual electrode ion optics an effective focusing of the released ions. The performance of the ion optics depends on the absolute potential on the electrostatic lenses as well as their ratio. While the absolute value of the potentials strongly affects the ion

transmission into the IMS and, the ratio between repeller and extractor potential mainly determines the ion clouds confinement. For the optimized extractor potential, the dimer peak (observed as broad undefined feature when adjusting repeller potential) becomes apparent at 6 kV and becomes more pronounced towards higher voltages applied to the extractor. The appearance of dimer peak indicates improved transport properties in the crucial region of the sample introduction region. Ion propagation in the laser beam direction is exceled by the generated double electric field allowing to direct the ions with a good result towards gas phase detection system.

To quantify the observed effects, Fig. 3 shows the FWHM, the absolute intensity, and the signal to noise (S/N) ratio at the different potentials applied. As can be seen in the left upper figure, the intensity increases roughly linearly with the applied $U_{Rep.}$ while the FWHM quickly increases to a constant value of ~ 1 ms. As the lower left plot indicates, the intensity is not the only factor, affecting a high sensitivity, but towards higher potential, also a higher noise level is observed resulting in no further S/N increase beyond $U_{Rep.}$ = 7.75 kV.

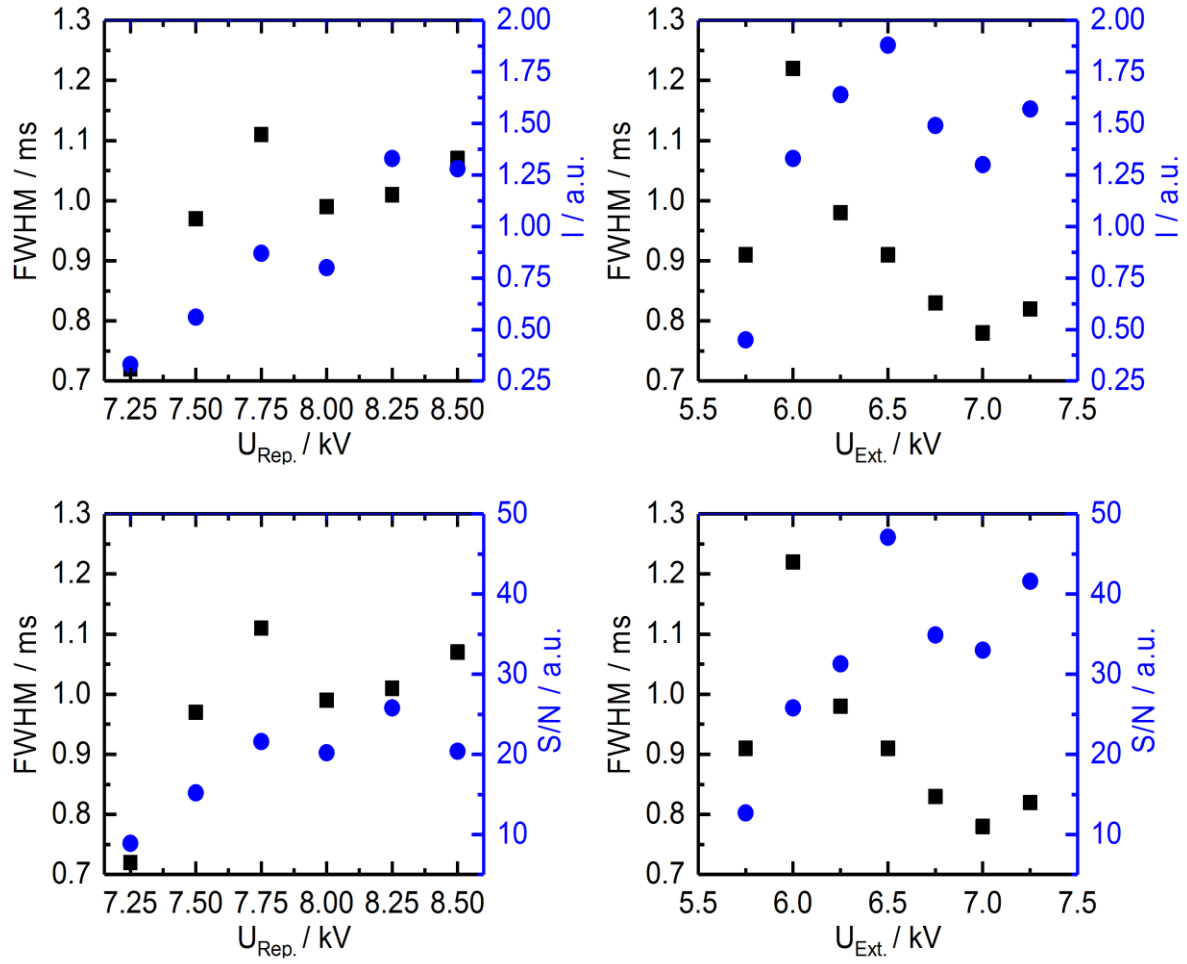

Fig. 3 Analytical performance of the used ion optics potential settings. The FWHM (black squares) determines the resolution of the instrument while the intensity (I) and Signal-to-noise (S/N) (blue circles) dictate the sensitivity. Left panel: absolute potential on repeller $U_{rep.}$ with a constant voltage of 6 kV applied to the extractor electrode. Right panel: Ratio $U_{ext.}/U_{rep.}$ at a constant $U_{rep.}$ of 8.25 kV. Upper trace: FWHM and absolute intensity, lower trace: FWHM and S/N.

Regarding the Extractor potential, the right upper trace clearly shows how the two electrode focusing design increases not only the total ion peak intensity I further up but also decreases the signal width drastically. The similarity between the upper and the lower right plot indicates that the applied potential does not significantly adds noise to the detector.

The best performance is achieved at the voltage ratio of 0.79 indicating that forces (i.e., atmospheric pressure, repulsion forces) acting in the sampling region/interface vicinity are compensated. Further alternation of the settings is pointless, the S/N ratio is not influenced above this value, the ion transport reaches plateau. Moreover, the provided second electrostatic lens in combination with repeller corrects for any of the 3, above mentioned, effects contributing to the peak width broadening. It compensate the complex 2-phase plume propagation mechanism composed of a) a fast propagating early and a b) slow propagating late fraction described in ref.[24] improving the distribution and time of ion detection.

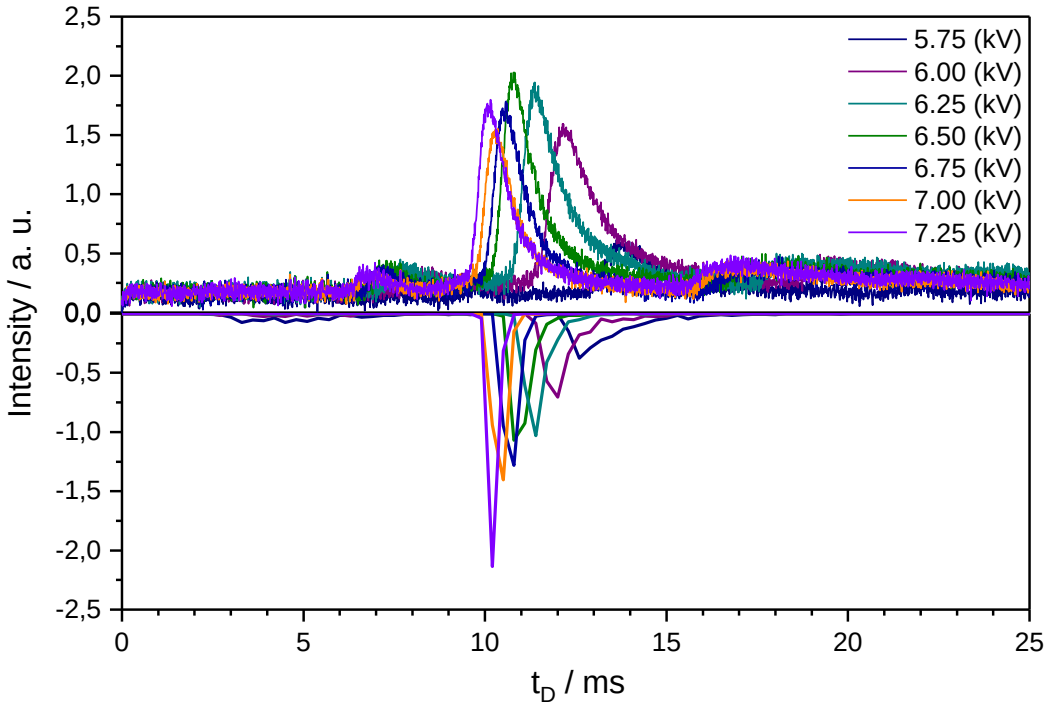

Fig. 4 Comparison of experimental spectra, acquired for a reference analyte – TBAB, (upper) and simulated spectra (lower).

To prove that the applied ion optics act as designed SIMION simulation was performed to mimic electric field generated between the lenses and the cylindrical IMS inlet (Supplementary Material). Simulation results are presented in Figure 4 and compared to experimentally obtained spectra. The primary broad low intensity peaks observed for simulated spectra indicate that the collimating power of the system is insufficient to overcome forces acting on the ejected ion plume confirming experimental conclusions. With the increasing high potential applied on the lenses the ion transmission improves exponentially, following enhanced intensity and FWHM. The ion transmission reach maximum at 7.25 kV representing the best ion confinement. The small distinctions in the drift times, between the simulated and real values, are most likely caused by imperfections of the exact input parameters for the simulation. The general trend achieved in the simulation follows the experimentally acquired spectra while the narrower peaks indicate additional phenomenon

that must be considered when discussing real system. The complex plume ejection nature is apparently not fully mirrored in the simulation hence, better resolution of the simulated peaks. Despite the care to keep the analysis conditions constant and repeatable some fluctuations in the atmospheric conditions can emerge which will be fully avoided in the simulation. Still, the good comparability between the simulated and the experimentally obtained spectra indicate a comprehensive understanding of the underlying focusing potentials.

To explore the real functionality of presented system L-arginine, promazine, atenolol were analysed using described conditions and compared to the reference analyte, TBAB. The laser spot for ionization/desorption out of the levitated droplet surface was adjusted prior to the experiments to allow efficient desorption of all investigated analytes without further re-adjustments between individual recordings. As presented in Figure 5 for L-arginine monomer as well as a dimer can be observed. The monomer peak appearing at 8.4 ms is a well-shaped, high intensity peak indicating indisputably appearance of L-arginine in the analysed sample. The dimer formation at 11.7 ms indicates high ionization ratio of the analyte and its good detectability by the presented gas phase detection scheme. Both peaks exhibit relatively low of FWHM indicating good ion confinement by the applied electrostatic lenses and separation within the IMS drift tube. The reactant ion peak (RIP) decreases in a favourable manner confirming efficiency of presented ionization scheme and analyte ion transfer inside the IMS drift tube. Atenolol ions are detected at 10.3 ms represented by a monomer peak with a significantly higher FWHM of 0.78 ms. The moderate ionization efficiency/ion transfer of atenolol as a probable cause for this broadening is also represented by the high intensity of the RIP peak. Promazine is detected at 10.1 ms. The monomer peak is 0.93 ms broad and exhibits a broad tailing and a high ionization efficiency. The observed tailing of the promazine peak imply possible dimer formation with a signal convoluted with the monomer peak. For the presented detection conditions, reference analyte the TBAB is detected at 10.8 ms and with a FWHM of 0.98 ms. The absolute values coincide with the one obtained during optimization of the system indicating the stability of the system. The minor change in the desorption conditions, do not significantly influence the detection limits of TBAB. Comparing respective spectra fluctuations in the drift time of the RIP peak are determined. These fluctuations are connected to minute changes in the exact position where the laser focus irradiated the levitated liquid droplet. Physical properties of the analyte solution such as surface tension influence the shape of the droplet confined in the acoustic field. For each analyte solution a slightly different laser focus position had to be chosen.

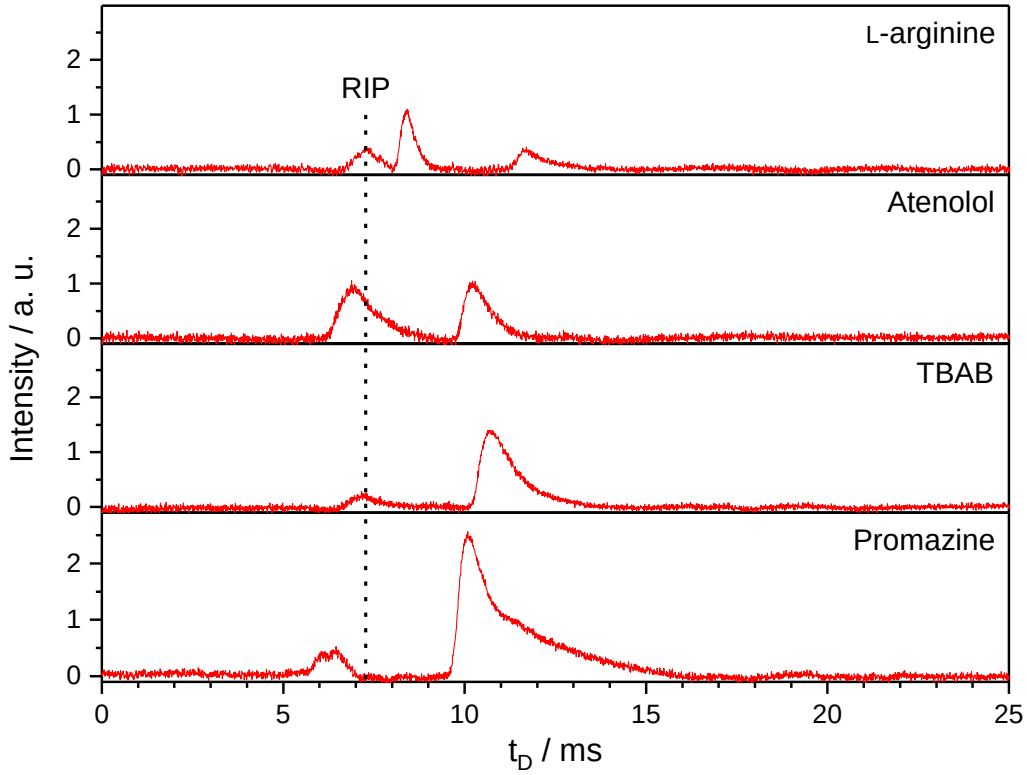

Fig. 5 IMS spectra acquired for reference analytes.

As can be seen in Table 3, the presented drift time values substantially overlap (Table 3) and only the L-arginine can be undeniably distinguished. Thus, for an analysis of complex mixtures further optimization of the system would be necessary. Although the resonant infrared laser strongly excites the internal degrees of freedom inside the interrogated solvent volume and the IMS is operated at elevated temperature, apparently the drift time alone does not suffice for an effective desolvation of the detected ions.. Analytical IMS instruments typically use a temporally decoupled desolvation step preceding the ions separation occurring in the drift tube, which was found to be especially important in case of analysis of liquid samples. Though the laser desorption/ionization results in the fine fume formation the solvent content remains moderately high. In case of ion separation based on number of the analyte ion collisions with a counter gas, the separation is, thus potentially disturbed by the number of solvent ions attached to the analyte ion substantially increasing collisional-cross section and smearing the separation efficiency. Future application of desolvation cell will allow to diminish number of solvent molecules and improve the separation. In cases of more complicated mixtures separation efficiency can also potentially be further improved by extending length of the drift tube.

Tab. 3 Experimental t_D values acquired for reference analytes

Analyte	**Mass**	**t_D [ms]**	**FWHM [ms]**
L-arginine	174.20	8.41 11.70	0.374 0.391
Atenolol	266.34	10.29	0.777
Promazine	284.42	10.09	0.929
TBAB	322.37	10.77	0.984

4. Conclusions

The acoustically levitated droplet can be utilized as novel sample introduction/ionisation system and coupled to the drift tube IMS *via* application of two electrostatic lenses generating double electrostatic field confining ions, ejected out of the surface of levitated droplet, towards IMS entrance. The operation of the applied ion optics in the atmospheric pressure conditions is optimized resulting in the highest possible ion transmission enabling qualitative analysis of number of analytes. The solvent droplet is sampled and ionized *via* ns laser pulses and the nascent ion plume is directly analysed by the drift tube IMS. Despite its small footprint the used IMS is fit for monitoring a reaction process especially when the collimating power of the applied ion optics is efficient reaching high quality results. The reliable operation of the ion optics is confirmed *via* computational simulation performed in SIMION software package. The simulation results confirm proper operation of the designed system and applied high potentials on its specific parts. Thought the drift time resolution, of the presented system, to analyse the chemical mixture is not sufficient, the peak's drift times substantially overlap, the performance of the proposed prototype can be further improved targeting towards more complex samples being especially suitable for sensitive reaction mixtures requiring containerless conditions, μL, uniform droplet volume and a fast analysis time.

Acknowledgments

This work was financially supported by the Excellence Initiative of the German Research Foundation (DFG).

Compliance with Ethical Standards

The authors declare that they have no conflict of interest.

References

1. Crawford EA, Esen C, Volmer DA. Real Time Monitoring of Containerless Microreactions in Acoustically Levitated Droplets *via* Ambient Ionization Mass Spectrometry. Anal Chem. 2016;88(17):8396-403.

2. Santesson S, Nilsson S. Airborne chemistry: acoustic levitation in chemical analysis. Anal Bioanal Chem. 2004;378(7):1704-9.

3. Welter E, Neidhart B. Acoustically levitated droplets — a new tool for micro and trace analysis. Fresenius J Anal Chem. 1997;357(3):345-50.

4. Mu C, Wang J, Barraza KM, Zhang X, Beauchamp JL. Mass Spectrometric Study of Acoustically Levitated Droplets Illuminates Molecular-Level Mechanism of Photodynamic Therapy for Cancer involving Lipid Oxidation. Angew Chem. 2019;131(24):8166-70.

5. Scheeline A, Behrens RL. Potential of levitated drops to serve as microreactors for biophysical measurements. Biophys Chem. 2012;165-166:1-12.

6. Schenk J, Tröbs L, Emmerling F, Kneipp J, Panne U, Albrecht M. Simultaneous UV/Vis spectroscopy and surface enhanced Raman scattering of nanoparticle formation and aggregation in levitated droplets. Anal Methods. 2012;4(5):1252-8.

7. López-Pastor M, Domínguez-Vidal A, Ayora-Cañada MJ, Laurell T, Valcárcel M, Lendl B. Containerless reaction monitoring in ionic liquids by means of Raman microspectroscopy. Lab on a Chip. 2007;7(1):126-32.

8. Leiterer J, Emmerling F, Panne U, Christen W, Rademann K. Tracing Coffee Tabletop Traces. Langmuir. 2008;24(15):7970-8.

9. Warschat C, Stindt A, Panne U, Riedel J. Mass Spectrometry of Levitated Droplets by Thermally Unconfined Infrared-Laser Desorption. Anal Chem. 2015;87(16):8323-7.

10. Westphall MS, Jorabchi K, Smith LM. Mass Spectrometry of Acoustically Levitated Droplets. Anal Chem. 2008;80(15):5847-53.

11. Eiceman GA. Ion-mobility spectrometry as a fast monitor of chemical composition. Trends Anal Chem. 2002;21(4):259-75.

12. Armenta S, Alcala M, Blanco M. A review of recent, unconventional applications of ion mobility spectrometry (IMS). Anal Chim Acta. 2011;703(2):114-23.

13. Hernández-Mesa M, Escourrou A, Monteau F, Le Bizec B, Dervilly-Pinel G. Current applications and perspectives of ion mobility spectrometry to answer chemical food safety issues. Trends Anal Chem. 2017;94(Supplement C):39-53.

14. Creaser CS, Griffiths JR, Bramwell CJ, Noreen S, Hill CA, Thomas CLP. Ion mobility spectrometry: a review. Part 1. Structural analysis by mobility measurement. Analyst. 2004;129(11):984-94.

15. Ewing RG, Atkinson DA, Eiceman GA, Ewing GJ. A critical review of ion mobility spectrometry for the detection of explosives and explosive related compounds. Talanta. 2001;54(3):515-29.

16. May JC, McLean JA. Ion Mobility-Mass Spectrometry: Time-Dispersive Instrumentation. Anal Chem. 2015;87(3):1422-36.

17. Cumeras R, Figueras E, Davis CE, Baumbach JI, Gracia I. Review on Ion Mobility Spectrometry. Part 1: current instrumentation. Analyst. 2015;140(5):1376-90.

18. Gunzer F, Zimmermann S, Baether W. Application of a Nonradioactive Pulsed Electron Source for Ion Mobility Spectrometry. Anal Chem. 2010;82(9):3756-63.

19. Zühlke M, Riebe D, Beitz T, Löhmannsröben H-G, Andreotti S, Reinert K, et al. High-performance liquid chromatography with electrospray ionization ion mobility spectrometry: Characterization, data management, and applications. J Sep Sci. 2016;39(24):4756-64.

20. Lapthorn C, Pullen F, Chowdhry BZ. Ion mobility spectrometry-mass spectrometry (IMS-MS) of small molecules: Separating and assigning structures to ions. Mass Spectrom Rev. 2013;32(1):43-71.

21. Beitz T, Laudien R, Löhmannsröben H-G, Kallies B. Ion Mobility Spectrometric Investigation of Aromatic Cations in the Gas Phase. J Phys Chem A. 2006;110(10):3514-20.

22. Wiley WC, McLaren IH. Time-of-Flight Mass Spectrometer with Improved Resolution. Rev Sci Instrum. 1955;26(12):1150-7.

23. Appelhans AD, Dahl DA. SIMION ion optics simulations at atmospheric pressure. Int J Mass Spectrom. 2005;244(1):1-14.

24. Michalik-Onichimowska A, Beitz T, Panne U, Löhmannsröben H-G, Riedel J. Microsecond mid-infrared laser pulses for atmospheric pressure laser ablation/ionization of liquid samples. Sens Actuators B Chem. 2017;238:298-305.

4. Discussion

The presented work highlights the significance of understanding the phenomena behind the laser ablation of acoustically levitated droplets and their comprehensive application in combination with gas-phase detection techniques, especially in combination with the IM spectrometry.

Acoustic levitation of objects is a unique technique allowing sample handling without direct contact. Its application in analytical and bioanalytical chemistry has proven itself to be highly successful. Building on those successes, the growing demand for novel, more reliable and robust, analytical techniques expands its application, in combination with simpler analytical methods, such as IM spectrometry.

The work performed in the frame of the project was focused on the coupling of an acoustically levitated droplet to an IM spectrometer and utilizing the system for on-line monitoring of photochemical reactions. Laser ablation was applied to achieve desolvation and ionization of the droplet surface for contactless handling of the droplet. This rather simple-appearing combination introduces a three-dimensional pattern in which each part of the system needs to be considered separately as well as a unit. The acoustically levitated droplet, utilized for both sample handling and introduction, must provide a high degree of freedom in the event of possible operations on the sample and must be easily accessible for desorption/ionization *via* laser ablation. The compact dimensionality of the acoustic levitator is advantageous when coupled to the IM spectrometer since the latter is also characterized by its modest size. However, the limited space poses certain obstacles to combining additional devices, as might be required for supporting droplet continuity and direct implementation as a microreactor to carry out the reaction within the droplet volume for the required time. When focusing on the ability of an acoustically levitated droplet to operate as a microreactor, the emphasis needs to be placed on possible interactions of the generated acoustic field with the droplet volume and hence with the reaction itself. The acoustic field can enhance reaction within the droplet. Though those properties haven't been directly considered in the work presented in chapter 3.1, they were anticipated when designing the system.

The desorption/ionization out of the droplet volume *via* laser ablation is complex and represents a critical point for the successful performance of the system. The chosen wavelength, 2,94 µm, allows resonance of the OH bond, hence is especially usable for water-based solvent systems. As shown, consideration of the parameters of the laser, as well as the properties of the irradiated sample, are crucial to achieving stable ion formation and a uniform ion cloud. The laser-based desorption/ionization of a liquid will result in different ion plume behaviour when performed on a thick water layer of 10 µm compared to a droplet of 5 µL, with a diameter of 3 mm.[52, 53] In the case of liquid droplets, direct investigation has shown that plume formation and ejection are spread in time, depending not only on the laser power, but, most importantly, on the pulse duration. The laser energy and its dissipation within the laser pulse duration are critical to achieving a well desolvated and spatially confined ion plume. A high laser energy, confined in a short laser pulse, will result in a rapidly evolving, erupted, ion plume. The ion plume ejection will be limited in time, while the plume propagation will result in complex dynamics and high ion solvation. The described complex dynamics influence the temporal and spatial confinement of the ion plume. The application of the laser pulse results in the formation of two-phases within the ion plume. It includes fast propagating and slow propagating, recombined, phases in the plume. The latter significantly increases the timeframe of plume propagation and its recombination and refocusing, hence

directly influencing the spatial and temporal quality of the plume (Figuer 2.). The laser energy injected into the droplet volume results in explosive boiling in which the matter is ejected rapidly. The time required for the transformation is not sufficient to create a well-desolvated ion plume. Instead, it results in sizable drops that are retained within the plume and the creation of some undesirable, non-functional, larger droplets. The sizable drops forming the plume recombine based on these two-phase dynamics and finally yield a moderately defined/desolvated ion plume. The overall time required for plume recombination and refocusing, as well as the original plume solvation that cannot be effectively mitigated, significantly affects the detected ion signal at the Faraday detector.

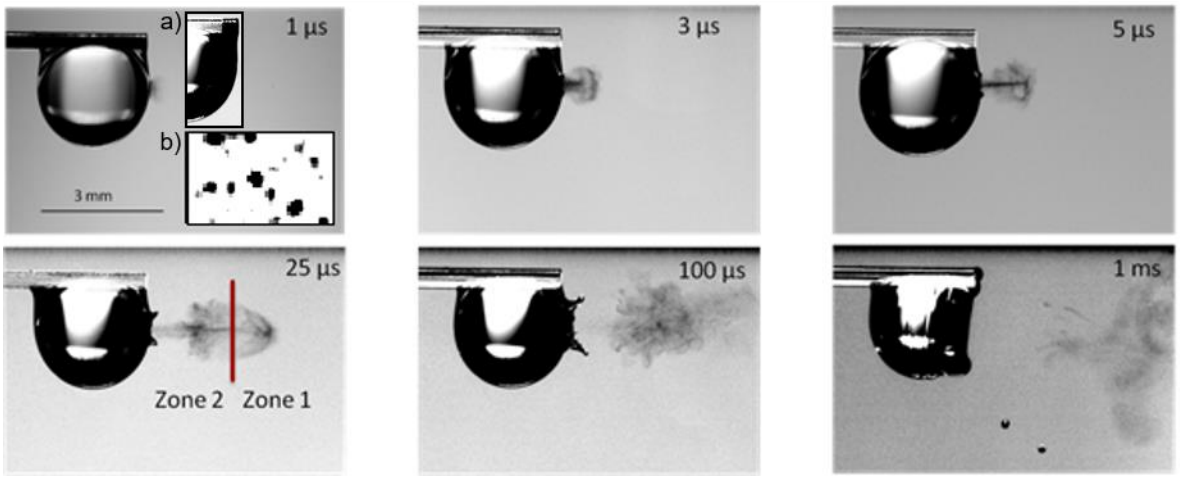

Figure 2. Shadowgraphy images of ablation dynamics following laser excitation with a pulse width of τp = 6 ns. Inset a) zoom of the vapour front at t= 700 ns, inset b) close up view on single pixel resolution.

Accordingly, the overall spectrum quality would be hindered without implementation of additional ion extraction procedures. However, those issues are not evident when using µs laser pulses. Here the energy is dissipated within the droplet volume on a longer timescale, revealing a rather gentle thermal spraying process instead of explosive boiling and connected sudden material ejection (Figure 3). The thermal spraying results in simple plume propagation (dynamics) with no recombination. Hence the overall timescale of plume ejection is significantly lower. The energy recombination within the droplet volume is much more efficient, allowing the generation of a well-desolvated ion plume that is directly transferred to the detection system without further complex dynamics occurring at the interface. This pure thermal spraying is reflected in the spectra that show better overall confinement.

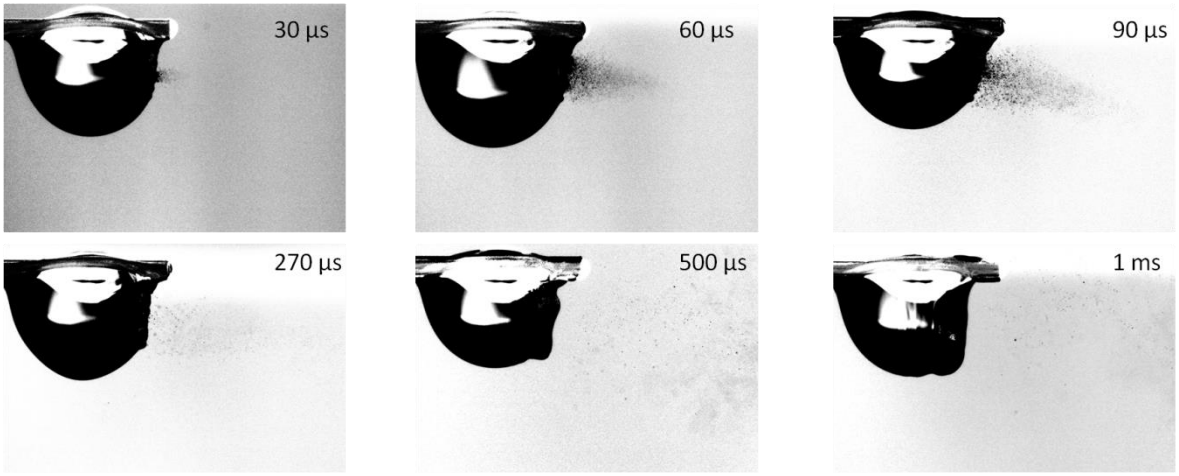

Figure 3. Shadowgraphy images of ablation dynamics following laser excitation with a pulse width of τp = 280 µs.

The comparison of IMS performance indicates an unequivocal predominance of the mild conditions of laser desorption/ionization when applied to acoustically levitated droplets. As is evident in the drift time spectra, the two-phase dynamics can be recognized and result in the worst IM spectral quality (Figure 4. lower trace). Though the intensity of the signal, as well as the area under the peak are higher, the delay used to characterize the plume propagation indicates a transient change in ion signal with increasing delay. The observed transient change illustrates the two-phase dynamics that are characteristic of short laser pulses. By following the evolution of the spectra, it becomes evident that the FWHM and peaks area are continuously decreasing until the transition point. At this point, the area continues to decrease since the number of ions constantly decrease. However, their spatial confinement is resolved, as indicate by FWHM. The higher focusing observed in the second phase of the plume ejection is connected to capturing only the slow propagating ions.

The situation looks differently for longer laser pulses in the µs time range (Figure 4. upper trace). Here the area under the peak continuously decreases, with the highest number of ions being ejected in the first several µs of the plume duration. As presented, the direct recombination of the ion plume does not occur. The confinement of the plume is not affected by the delay used. The ion plume is dissipated in the phase space with increasing delay.

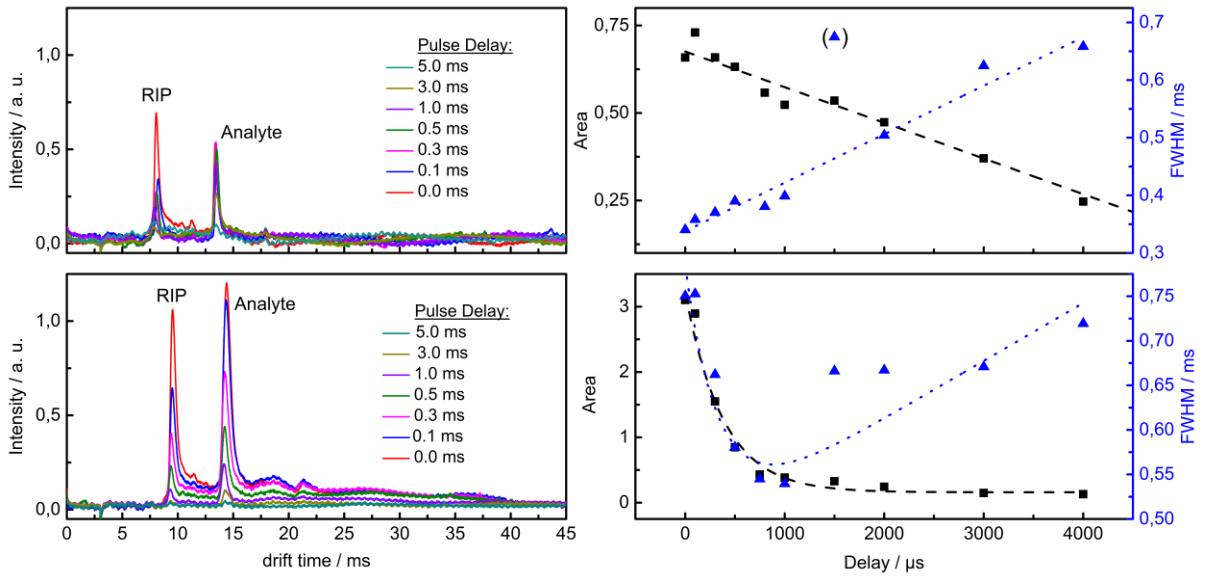

Figure 4. left column: IMS spectra of perphenazine using laser ablation with (upper trace): Er:YAG laser and (lower trace): OPO for different extraction time delays. The right column compares the overall analyte ion signal (area) and temporal width of the analyte peak (FWHM) for the two selected laser pulses.

The presented investigation indicates that achieving steady and well-confined ion plumes in acoustically levitated droplet requires mild conditions of laser ablation.

Nonetheless, further distinction of applied laser pulse duration might be necessary due to the possible occurrence of decomposition reactions if applied for biomolecule analysis. In theory, both processes, i) laser desorption and ii) laser ejection, with some limitations and requirements, have been described as effective for processing biomolecules in matrixes. As summarized by Levis,[54] molecular desorption will occur on a shorter timescale compared to decomposition reactions if the heating rate is high enough (10^8 to 10^{11} Ks^{-1}). The transfer of the energy needs to be rapid to desorb the molecules intact, not allowing decomposition reactions to occur. This point is valid for pulsed laser sources. In the case of µs laser with a long pulse duration of ~280 µs the heat is dissipated within the pulse width leading to constant heating of the droplet volume. This may lead to possible decomposition/conformational changes in biomolecules. Hence, the process of desorption of biomolecules out of the liquid droplet *via* µs laser pulses should be further investigated.

To realize the coupling of acoustically levitated droplet to the drift tube IM spectrometer, the ns laser has been chosen as the reference ionization method. The performance of the ns laser, when coupled to an IM spectrometer has been already thoroughly investigated.[52, 53, 55] To facilitate the development stage, the coupling of a novel sample introduction system, as well as a well-defined/functioning laser desorption/ionization source were of importance.

The successful coupling of levitated droplets to IM spectrometer requires the application of additional ion optics to transfer the ions ejected out of the droplet surface to the IM spectrometer entrance. The ions are ejected from the droplet at ambient pressure, outside the IM spectrometer instrument. The separation occurs in the low electric field prevailing in the IM spectrometer. Therefore, the gap in the ion carrier between their ejection and arrival at the IM spectrometer entrance (operating at 5,5 kV), requires incorporation of two electrostatic lenses. The electrostatic lenses generate an electrostatic field around the levitated droplet and the IM spectrometer entrance. The physical simplicity, however, does not follow the technical requirements of the system. Application of two electrostatic lenses at high voltage, between 6 and 10 kV, at the intersection with an acoustic field, constrains miniaturization of the system to avoid discharges between the lenses and parts of the acoustic trap. Hence, the primary approach was consistent with the two bent metal wires to which the high voltage was applied. This solution has allowed the manipulation of the lenses in the vicinity of the droplet and avoids its interaction with the propagating laser beam.

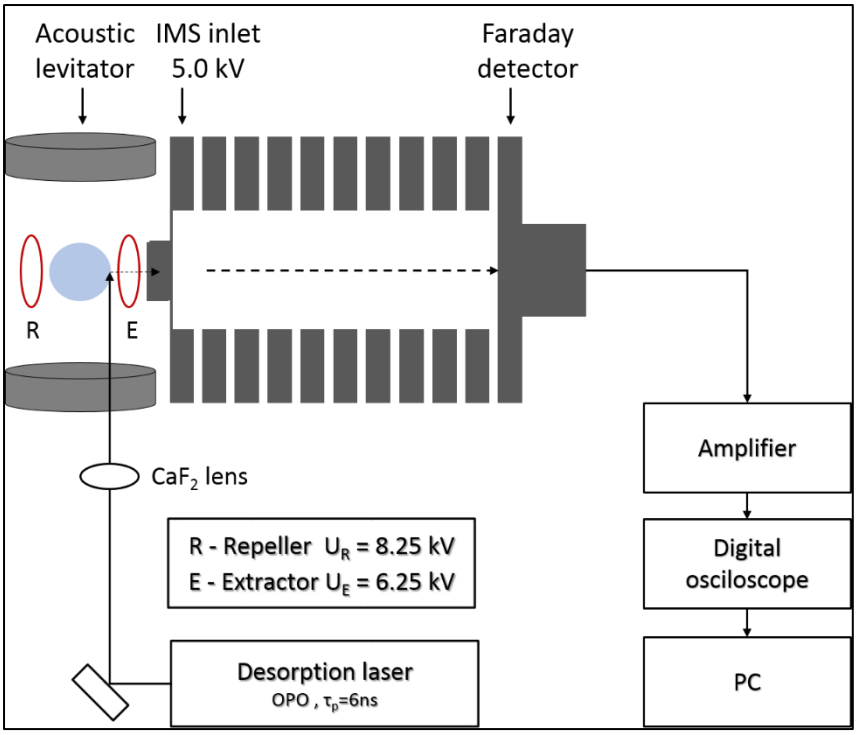

Figure 5. Schematic of the experimental setup representing applied ion optics composed of two electrostatic lenses.

The Figure 6. represents the modelled electrostatic field, generated by utilizing two electrostatic lenses, one before and one after the levitated droplet, at a distance of 5 mm. The simulation results indicate the generation of a steep electrostatic field gradient between the parts of the system. The electrostatic field generated around the levitated droplet allows focusing of the ion plume and its transfer under ambient conditions. Since the droplet irradiation occurs at a right angle to the IM spectrometry entrance, the applied field overcomes the original propagation of the ion plume aligned to the propagation direction of the laser beam.

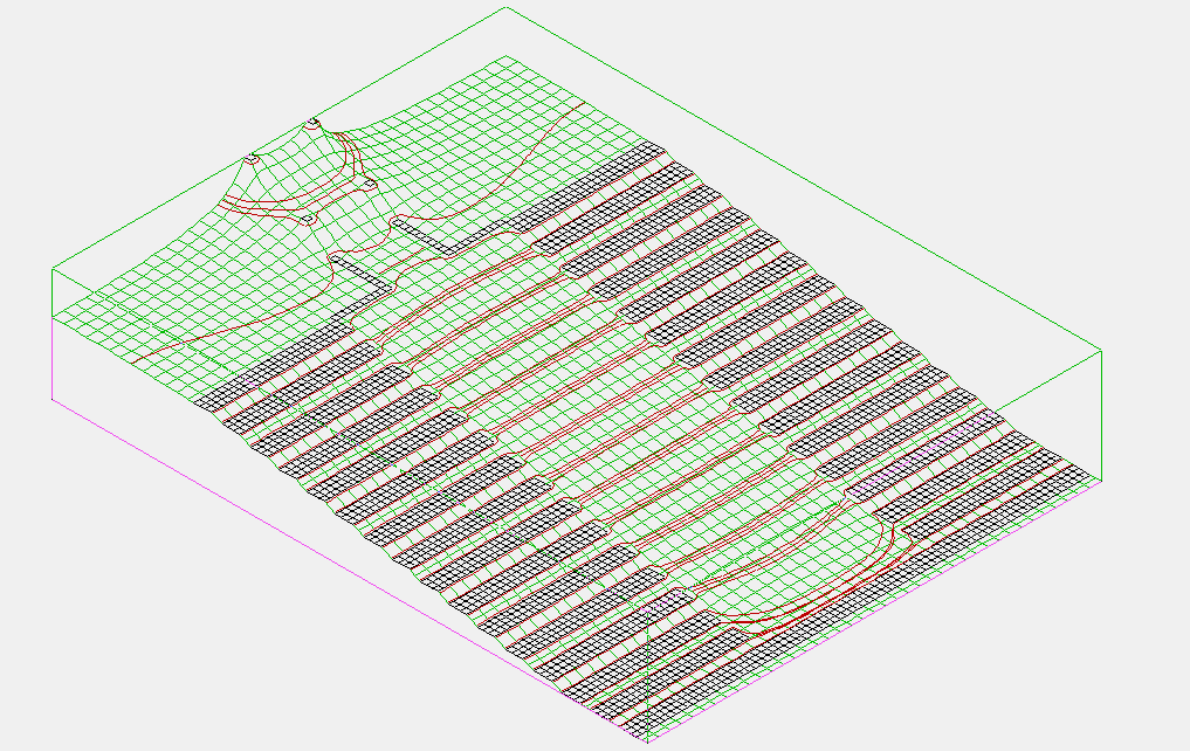

Figure 6. Simion simulation representing behaviour of the field at the acoustic trap – IMS entrance interface. Simulation represents the 3D potential profile of optimised system: A) Repeller electrode operated at 8.25 kV, B) Extractor electrode operated at 6.5 kV

The manipulation of the potentials applied to the electrostatic lenses has allowed optimum system performance conditions to be established based on the peak intensity, broadening, and dimer formation (Figure 7.). Further investigation has been focused on demonstrating real analytical possibilities. However, due to the simplified arrangement of the IM spectrometer, the obtained resolution was not sufficient to achieve mixture analysis. Moreover, the oscillations in the droplet volume, as well as minor migration of the droplet in the z-direction, combine with the initial ion plume and are reflected in the rise of the peak in the spectrum and the t_D of the analyte signal. The simplified construction of the IM spectrometer, particularly the lack of a desolvation cell, results in further broadening of the signal that is inherent to systems lacking features compensating for poorly desolvated ions. Emphasis must be placed on the proper characterization of the ionization method and its influence on the spectrum quality. Though the work has been focused on desorption/ionization *via* a ns laser beam providing a well-characterized ion plume, its further manipulation is required to increase the overall quality of the separation.

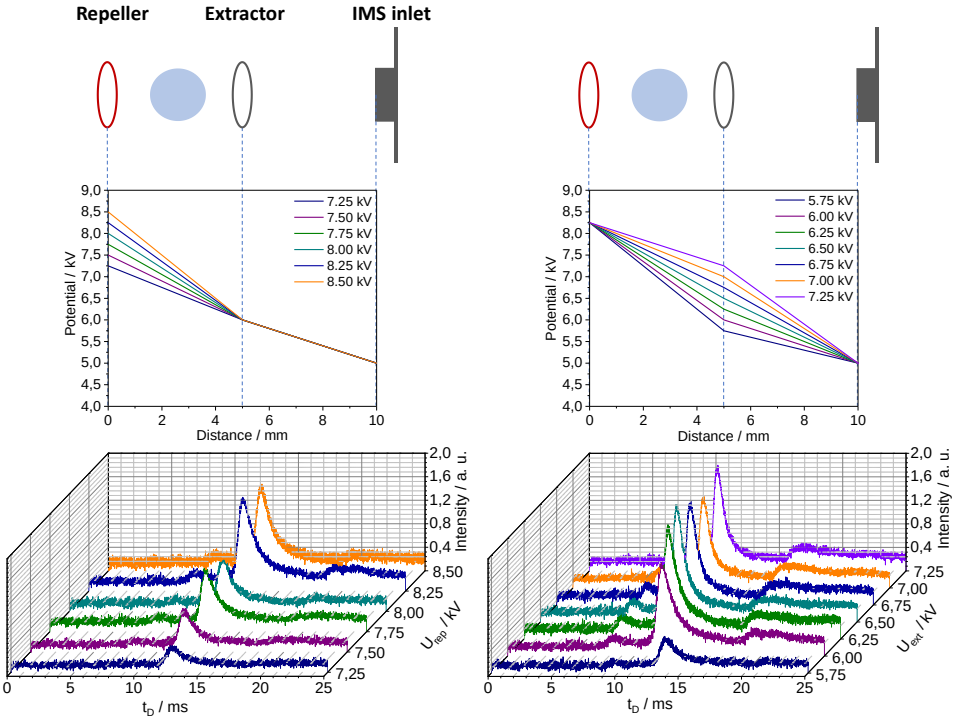

Figure 7. IMS performance. Top row: schematic; center row: potential gradient along the propagation towards the IMS entrance; bottom row: resulting IMS drift time spectra. Left column: optimization of repeller electrode voltage; right column, optimization of extractor potential.

In order to show a real-world application of the system, a model photochemical reaction has been chosen and its performance assessed using ^{1}H NMR to establish reaction kinetic baseline. The focus of this part of the work was to carry out the same reaction in a microreactor and monitor it using on-line techniques to evaluate the reaction rate. This step was necessary to characterize the chemical system, its reactivity, and its performance. Due to the possible influence of the acoustic field on the volume of the levitated droplet, which can interact with the reaction at an early stage of the coupling, evaluating the reaction reproducibility was of importance. The thiol-ene coupling was chosen as the model reaction. The kinetics were initially analysed using high field ^{1}H NMR as well as an IHM approach, allowing calibration-free measurements to be carried out.

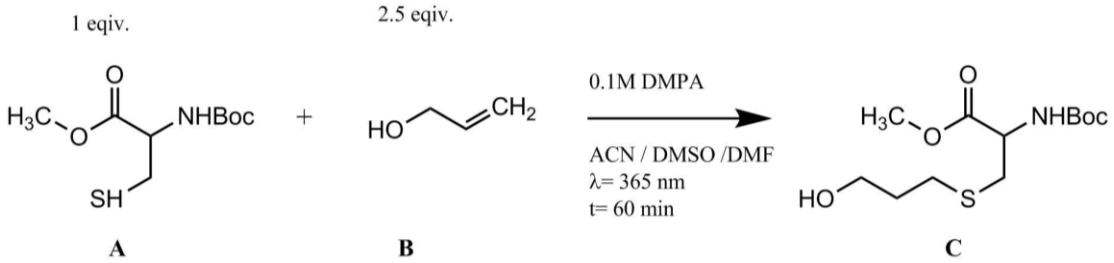

Figure 8. Model photochemical reaction for proof-of-principle studies. The reaction performance was established using on-line detection via ^{1}H NMR.

The reaction between N-Boc cysteine methyl ester and allyl alcohol, photochemically activated at $\lambda = 365$ nm, proceeds to completion within one hour, demonstrating that it is optimal for the conditions required by the NMR setup. Under these conditions, the S-H bond is completely converted by coupling with allyl alcohol. The reaction was carried in 3 solvents

to investigate reaction propagation dependence. Reaction in ACN solvent results in the fastest reaction rate. The presented concentration-time profiles indicate that high-quality results can be achieved for a single scan method utilizing IHM in combination with a highly linear response of the spectrometer. Moreover, with this approach, the amount of time for subsequent analysis is reduced.

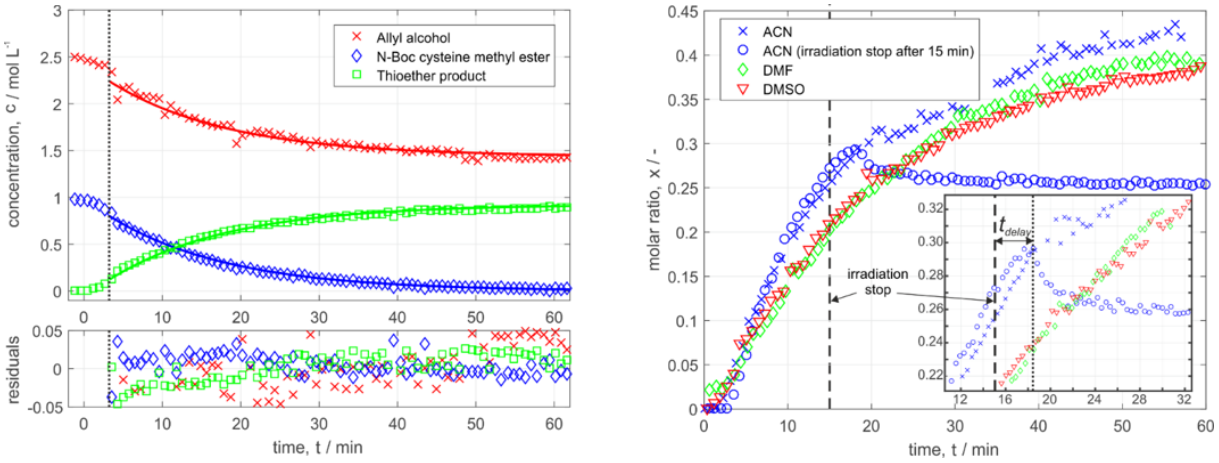

Figure 9. Reaction propagation based on ^{1}H NMR studies and hard sphere modelling.

Reaction in ACN, monitored *via* ^{1}H NMR, shows 79% conversion within the first 20 minutes. This means that the proposed reaction can be, carried out in acoustically levitated droplets and directly analysed *via* the IM spectrometry detection scheme without any limits. The high reproducibility of the studied chemical system is especially important in the case of establishing new couplings with a higher dimension of complexity. The chemical system utilized for on-line ^{1}H NMR can be directly applied to at-line, and in the ultimate potential application, to real-time investigation of reaction *via* gas-phase detection schemes.

5. Summary

The presented work demonstrates possible lab-on-a-drop developments utilizing acoustically levitated droplets coupled to IM spectrometer for gas-phase detection. The set of results illustrate the feasibility of the designed set up as well as suggest possible improvements to increase the sensitivity of the system. A major part of the work is focused on defining the technical constraints that must be evaluated and resolved to achieve successful operation of the system. Application of the proper laser pulse duration, as well as the focusing of the ions in the ambient atmosphere, is vital to achieving an optimal ion signal in the Faraday plate detector of the IM spectrometer. Hence, the presented design of the ion optics, in combination with application of ns laser pulses, demonstrates potential for providing moderate results. The applied ns laser source has been used as reference ionization technique typically utilized, till now, in combination with IM spectrometry. The defined complex plume ejection and ion transport has been compensated by the surrounding electrostatic field, generated *via* two electrostatic lenses, guiding the ions into the IM spectrometer.

By modifying the conditions of laser irradiation and lensing, the temporal and spatial spread of the ion plume can be compensated to some extent. The achieved quality of the plume allows detection of a well confined ions packet at the Faraday detector, yielding sufficient signal for unambiguous identification of single analytes. Nonetheless, the presented detection system is not capable of categorical characterization of mixture composition. The signal was judged to be the maximum achievable given state of the experimental design. The design imposes certain constrains limiting further improvement of signal quality that would be necessary to unambiguously identify constituents of samples having moderate to complex composition. To further increase the signal intensity, the IM spectrometer needs to be enhanced by the addition of a desolvation cell. A desolvation cell is expected to achieve further spatial and temporal resolution of the ion plume. Additional desolvation of the ions should allow differentiation of the ions by size and time of arrival at the Faraday detector, enhancing resolution of the system.

The proposed model reaction satisfies all requirements necessary to demonstrate the feasibility of carrying out the reaction in a levitated droplet. These include i) a high reaction rate (significant degree of completion within 20 minutes), ii) reaction in a medium that can be directly applied as the acoustic droplet volume, iii) the chosen desorption/ionization source is capable of ionizing an appreciable portion of the mixture with/without post ionization, and finally iv) the analytes can be detected *via* gas phase detection schemes like MS and IM spectrometry.

Further, comprehensive studies performed by on-line ^{1}H NMR, allowed characterization of the rection and definition of its kinetics in 3 different solvents.

Though the presented work still shows potential for further improvements, the basic principles has been demonstrated. The acoustically levitated droplet can be coupled to IM spectrometer with a high degree of success and used as a direct sample introduction/ionization system. The entire experimental setup operates at atmospheric pressure, not requiring costly vacuum pumps. The introduced ion optics, though simple in design, effectively compensate for plume dissipation and can be easily upgraded. Current improvements in IM spectrometer design and application illustrate the increasing importance of the IM spectrometry technique and motivate research into new applications. The innovative experimental design presented illustrates newly emerged options in the field of real time reaction interrogation. The system has shown numerous advantages, including, i) a small reaction volume, ii) no wall

confinement, iii) as well as simple and cost-effective detection technique, where numerous ionization techniques can be incorporated. The latter are then defined based on the analyte chemistry.

6. References

1. Workman J, Lavine B, Chrisman R, Koch M. Process Analytical Chemistry. Analytical Chemistry. 2011;83(12):4557-78.

2. Fair RB. Digital microfluidics: is a true lab-on-a-chip possible? Microfluidics and Nanofluidics. 2007;3(3):245-81.

3. Stone HA, Stroock AD, Ajdari A. Engineering Flows in Small Devices: Microfluidics Toward a Lab-on-a-Chip. Annual Review of Fluid Mechanics. 2004;36(1):381-411.

4. Streets AM, Huang Y. Chip in a lab: Microfluidics for next generation life science research. Biomicrofluidics. 2013;7(1):011302.

5. Reyes DR, Iossifidis D, Auroux P-A, Manz A. Micro Total Analysis Systems. 1. Introduction, Theory, and Technology. Analytical Chemistry. 2002;74(12):2623-36.

6. Auroux P-A, Iossifidis D, Reyes DR, Manz A. Micro Total Analysis Systems. 2. Analytical Standard Operations and Applications. Analytical Chemistry. 2002;74(12):2637-52.

7. Dittrich PS, Manz A. Lab-on-a-chip: microfluidics in drug discovery. Nature Reviews Drug Discovery. 2006;5(3):210-8.

8. Samiei E, Tabrizian M, Hoorfar M. A review of digital microfluidics as portable platforms for lab-on a-chip applications. Lab on a Chip. 2016;16(13):2376-96.

9. Abgrall P, Gué AM. Lab-on-chip technologies: making a microfluidic network and coupling it into a complete microsystem—a review. Journal of Micromechanics and Microengineering. 2007;17(5):R15-R49.

10. Santesson S, Nilsson S. Airborne chemistry: acoustic levitation in chemical analysis. Analytical and Bioanalytical Chemistry. 2004;378(7):1704-9.

11. Welter E, Neidhart B. Acoustically levitated droplets — a new tool for micro and trace analysis. Fresenius' Journal of Analytical Chemistry. 1997;357(3):345-50.

12. Mu C, Wang J, Barraza KM, Zhang X, Beauchamp JL. Mass Spectrometric Study of Acoustically Levitated Droplets Illuminates Molecular-Level Mechanism of Photodynamic Therapy for Cancer involving Lipid Oxidation. Angewandte Chemie. 2019;131(24):8166-70.

13. Scheeline A, Behrens RL. Potential of levitated drops to serve as microreactors for biophysical measurements. Biophysical Chemistry. 2012;165-166:1-12.

14. Santesson S, Barinaga-Rementeria Ramírez I, Viberg P, Jergil B, Nilsson S. Affinity Two-Phase Partitioning in Acoustically Levitated Drops. Analytical Chemistry. 2004;76(2):303-8.

15. Zang D, Yu Y, Chen Z, Li X, Wu H, Geng X. Acoustic levitation of liquid drops: Dynamics, manipulation and phase transitions. Advances in Colloid and Interface Science. 2017;243:77-85.

16. Shen CL, Xie WJ, Wei B. Parametric resonance in acoustically levitated water drops. Physics Letters A. 2010;374(23):2301-4.

17. Eberhardt R, Neidhart B. Acoustic levitation device for sample pretreatment in microanalysis and trace analysis. Fresenius' Journal of Analytical Chemistry. 1999;365(6):475-9.

18. Petersson M, Nilsson J, Wallman L, Laurell T, Johansson J, Nilsson S. Sample enrichment in a single levitated droplet for capillary electrophoresis. Journal of Chromatography B: Biomedical Sciences and Applications. 1998;714(1):39-46.

19. Schenk J, Tröbs L, Emmerling F, Kneipp J, Panne U, Albrecht M. Simultaneous UV/Vis spectroscopy and surface enhanced Raman scattering of nanoparticle formation and aggregation in levitated droplets. Analytical Methods. 2012;4(5):1252-8.

20. López-Pastor M, Domínguez-Vidal A, Ayora-Cañada MJ, Laurell T, Valcárcel M, Lendl B. Containerless reaction monitoring in ionic liquids by means of Raman microspectroscopy. Lab on a Chip. 2007;7(1):126-32.

21. Leiterer J, Delißen F, Emmerling F, Thünemann AF, Panne U. Structure analysis using acoustically levitated droplets. Analytical and Bioanalytical Chemistry. 2008;391(4):1221-8.

22. Leiterer J, Emmerling F, Panne U, Christen W, Rademann K. Tracing Coffee Tabletop Traces. Langmuir. 2008;24(15):7970-8.

23. Westphall MS, Jorabchi K, Smith LM. Mass Spectrometry of Acoustically Levitated Droplets. Analytical Chemistry. 2008;80(15):5847-53.

24. Warschat C, Stindt A, Panne U, Riedel J. Mass Spectrometry of Levitated Droplets by Thermally Unconfined Infrared-Laser Desorption. Analytical Chemistry. 2015;87(16):8323-7.

25. Crawford EA, Esen C, Volmer DA. Real Time Monitoring of Containerless Microreactions in Acoustically Levitated Droplets *via* Ambient Ionization Mass Spectrometry. Analytical Chemistry. 2016;88(17):8396-403.

26. May JC, McLean JA. Ion Mobility-Mass Spectrometry: Time-Dispersive Instrumentation. Analytical Chemistry. 2015;87(3):1422-36.

27. Kanu AB, Dwivedi P, Tam M, Matz L, Hill Jr. HH. Ion mobility–mass spectrometry. Journal of Mass Spectrometry. 2008;43(1):1-22.

28. Lapthorn C, Pullen F, Chowdhry BZ. Ion mobility spectrometry-mass spectrometry (IMS-MS) of small molecules: Separating and assigning structures to ions. Mass Spectrometry Reviews. 2013;32(1):43-71.

29. Krechmer JE, Groessl M, Zhang X, Junninen H, Massoli P, Lambe AT, et al. Ion mobility spectrometry–mass spectrometry (IMS–MS) for on- and offline analysis of atmospheric gas and aerosol species. Atmospheric Measurement Techniques. 2016;9(7):3245-62.

30. Karasek FW. Plasma Chromatography. Analytical Chemistry. 1974;46(8):710A-20A.

31. Hartner NT, Raddatz C-R, Thoben C, Piendl SK, Zimmermann S, Belder D. On-Line Coupling of Chip-Electrochromatography and Ion Mobility Spectrometry. Analytical Chemistry. 2020.

32. Lippmann M, Kirk AT, Hitzemann M, Zimmermann S. Compact and Sensitive Dual Drift Tube Ion Mobility Spectrometer with a New Dual Field Switching Ion Shutter for Simultaneous Detection of Both Ion Polarities. Analytical Chemistry. 2020;92(17):11834-41.

33. Ekelöf M, Dodds J, Khodjaniyazova S, Garrard KP, Baker ES, Muddiman DC. Coupling IR-MALDESI with Drift Tube Ion Mobility-Mass Spectrometry for High-

Throughput Screening and Imaging Applications. Journal of the American Society for Mass Spectrometry. 2020;31(3):642-50.

34. Cumeras R, Figueras E, Davis CE, Baumbach JI, Gracia I. Review on Ion Mobility Spectrometry. Part 1: current instrumentation. Analyst. 2015;140(5):1376-90.

35. Eiceman GA, Karpas Z, Jr H. Ion mobility spectrometry, third edition2013. 1-400 p.

36. Hill HH, Siems WF, Louis RHS, McMinn DG. ION MOBILITY SPECTROMETRY. Analytical Chemistry. 1990;62(23):1201A-9A.

37. Gabelica V, Marklund E. Fundamentals of ion mobility spectrometry. Current Opinion in Chemical Biology. 2018;42(Supplement C):51-9.

38. Gabelica V, Shvartsburg AA, Afonso C, Barran P, Benesch JLP, Bleiholder C, et al. Recommendations for reporting ion mobility Mass Spectrometry measurements. Mass Spectrometry Reviews. 2019;38(3):291-320.

39. Kaur-Atwal G, O'Connor G, Aksenov AA, Bocos-Bintintan V, Paul Thomas CL, Creaser CS. Chemical standards for ion mobility spectrometry: a review. International Journal for Ion Mobility Spectrometry. 2009;12(1):1-14.

40. Peacock PM, Zhang W-J, Trimpin S. Advances in Ionization for Mass Spectrometry. Analytical Chemistry. 2017;89(1):372-88.

41. Kirk AT, Zimmermann S. Bradbury-Nielsen vs. Field switching shutters for high resolution drift tube ion mobility spectrometers. International Journal for Ion Mobility Spectrometry. 2014;17(3):131-7.

42. Tyndall AM, Powell CF. The Mobility of Ions in Pure Gases. Proceedings of the Royal Society of London Series A, Containing Papers of a Mathematical and Physical Character. 1930;129(809):162-80.

43. Jafari MT, Saraji M, Mossaddegh M. Mitigation of solvent interference using a short packed column prior to ion mobility spectrometry. Talanta. 2017;167(Supplement C):486-92.

44. Versluis M. High-speed imaging in fluids. Experiments in Fluids. 2013;54.

45. Castrejón-García R, Castrejón-Pita JR, Martin GD, Hutchings IM. The shadowgraph imaging technique and its modern application to fluid jets and drops. Revista mexicana de física. 2011;57:266-75.

46. Settles GS, Hargather MJ. A review of recent developments in schlieren and shadowgraph techniques. Measurement Science and Technology. 2017;28(4):042001.

47. Settles GS. Smartphone schlieren and shadowgraph imaging. Optics and Lasers in Engineering. 2018;104:9-21.

48. Mitchell J, Gladden LF, Chandrasekera TC, Fordham EJ. Low-field permanent magnets for industrial process and quality control. Progress in Nuclear Magnetic Resonance Spectroscopy. 2014;76:1-60.

49. Dalitz F, Cudaj M, Maiwald M, Guthausen G. Process and Reaction Monitoring by Low-Field NMR Spectroscopy. Progress in nuclear magnetic resonance spectroscopy. 2012;60:52-70.

50. Zientek N, Laurain C, Meyer K, Paul A, Engel D, Guthausen G, et al. Automated data evaluation and modelling of simultaneous 19F–1H medium-resolution NMR spectra for online reaction monitoring. Magnetic Resonance in Chemistry. 2016;54(6):513-20.

51. Kern S, Wander L, Meyer K, Guhl S, Mukkula ARG, Holtkamp M, et al. Flexible automation with compact NMR spectroscopy for continuous production of pharmaceuticals. Analytical and Bioanalytical Chemistry. 2019;411(14):3037-46.

52. Charvat A, Stasicki B, Abel B. Product Screening of Fast Reactions in IR-Laser-Heated Liquid Water Filaments in a Vacuum by Mass Spectrometry. The Journal of Physical Chemistry A. 2006;110(9):3297-306.

53. Charvat A, Abel B. How to make big molecules fly out of liquid water: applications, features and physics of laser assisted liquid phase dispersion mass spectrometry. Physical Chemistry Chemical Physics. 2007;9(26):3335-60.

54. Levis RJ. Laser Desorption and Ejection of Biomolecules From the Condensed Phase into the Gas Phase. Annual Review of Physical Chemistry. 1994;45(1):483-518.

55. Kleinekofort W, Avdiev J, Brutschy B. A new method of laser desorption mass spectrometry for the study of biological macromolecules. International Journal of Mass Spectrometry and Ion Processes. 1996;152(2):135-42.

Acknowledgments

I dedicate this work to my husband. You have supported me all over the way and I know that it means as much to me as to you. With our twins the world has changed but the priorities have stayed the same. We have managed through all the better and worst times together during that time and this is the final touch.

A special thank you goes to Dr. Jens Riedel. Being a part of your Team was a great experience, the scientific world with you is an easy task. I thank you for constant support nonmatter the situation, for your motivation and new ideas. I also thank you for knowing when to say stop.

To Dr. Toralf Beitz for introducing me to an intriguing world of the ion mobility spectrometry. Thank to you I have fall in love with this technique.

To Prof. Löhmannsröben and Prof. Panne for being impeccable part of the creation process of the thesis.

All of you have made an impossible to possible! Thank you very much.